Computational Biomechanics for Medicine XII

A MICCAI 2017 Workshop
Quebec City, Canada, 2017 September 14

Poul M.F. Nielsen[1,2], Adam Wittek[3], Karol Miller[3,5], Barry Doyle, Grand R. Joldes[3,4], Martyn Nash[1,2]

[1]Auckland Bioengineering Institute, The University of Auckland, New Zealand
[2]Department of Engineering Science, The University of Auckland, New Zealand
[3]Intelligent Systems for Medicine Laboratory, School of Mechanical and Chemical Engineering, The University of Western Australia, 35 Stirling Highway, Crawley/Perth, WA 6009, Australia
[4]School of Engineering and Information Technology, Murdoch University, 90 South St, Murdoch, Australia
[5]School of Engineering, Cardiff University, The Parade, CF24 3AA Cardiff, United Kingdom

Contents

Making head and neck reconstruction surgery an engineering process

Sid Fels

Dept. of Electrical and Computer Engineering, The University of British Columbia
Vancouver, BC, Canada, V6T 1Z4

Abstract

Computer modeling and simulation of the human body is rapidly becoming a critical and central tool in a broad range of disciplines, including engineering, education, entertainment, physiology and medicine. Often, these models underpin the goal of transitioning from an artisanal practice to designing and making to an industrial engineering process. One reason for this approach is that designed and simulated models can be thoroughly tested used manufactured by machine to high tolerances, potentially removing much of the guess work when addressing complex human body dynamics and variations. The challenge for researchers is how to create patient specific models with enough fidelity for in-silico simulation to accurately predict treatment outcomes. To address these challenges, we are developing technology to create dynamic, parametric, multiscale models of human musculoskeletal anatomy that can later be extended to include organ structures and other subsystems. We are working to provide a range, from low-to-high accuracy, of models, including high-resolution bone surfaces and detailed representations of muscle fibre structure and pennation. A significant component of our approach provides 3D finite element (FEM) muscle models coupled with multibody simulation techniques including contact handling and constraints. Our primary modelling effort is for the oral, pharyngeal and laryngeal (OPAL) complex to predict functional outcomes, such as chewing, swallowing and speaking. I report on our progress with our interdisciplinary team of scientific and clinical investigators, and collaborators and iRSM partners, the advances we have made including: an advanced Functional Reference ANatomy Knowledge (FRANK) template of the head and neck that can be registered structurally and functionally to patient specific data, new techniques for patient specific registration, liquid bolus simulations in the head and neck models, and a new technique for simulating speech from the biomechanics of the airway. Based on our experiences, I will outline a number of grand challenges that require a community of clinical, scientific and engineering researchers to address before we can transition to patient treatment as an engineered solution.

Atlas of Acceleration-Induced Brain Deformation from Measurements in Vivo

Arnold D. Gomez[1], Andrew Knutsen[2], Deva Chan[2], Yuan-Chiao Lu[2], Dzung L. Pham[2], Philip Bayly[3], and Jerry L. Prince[1]

[1]Department of Electrical and Computer Engineering, Johns Hopkins University, Baltimore, USA

[2]Center for Neuroscience and Regenerative Medicine, Henry Jackson Foundation, Bethesda, USA

[3]Mechanical Engineering Department, Washington University in St. Louis, St. Louis, USA

Abstract

In traumatic brain injury (TBI), rapid head acceleration resulting from a blow or fall results in detrimental brain tissue deformation. These types of injuries are frequent and can have devastating effects. Understanding the relationship between acceleration and deformation is a challenging and essential step towards designing effective preventive strategies. This study describes patterns of acceleration-induced brain deformation in a group of human volunteers (n=7). Unlike previous research, the analysis herein involved spatiotemporal analysis of 3D kinematics. In each subject, tagged magnetic resonance imaging (MRI) was acquired during a mild acceleration event, and displacements were extracted using a mechanically regularized motion estimation algorithm. This technique involved registering an anatomical template (a finite-element mesh) to all of the subjects allowing translation of scalar strain projections back to the template to be averaged. Our results show that, in individuals, weighting acceleration measurements by the subject's brain volume improves the correlation between acceleration magnitude and deformation (R^2 of 0.66 in the weighted comparison, compared to 0.34). In individuals, and the group, brain deformation peaked after the peak acceleration, and near the interface between the brain and the skull. However, some deformation was also observed near medial brain structures, which supports the idea that the falx plays a role in transferring mechanical power to the middle of the brain.

Introduction

Acceleration-induced brain deformation is associated with concussion and TBI [1, 2]. Complications associated with TBI are an important cause of disabilities af-

fecting people of all ages worldwide [2]. The central component of the injury process is rapid deformation of the brain after an acceleration event, such as a blow or fall. A clear understanding about how brain tissue deforms in such an event, would be key to develop preventive strategies aimed at reducing injury likelihood. However, this type of brain biomechanics is affected by different factors including the magnitude and direction of acceleration, differences in geometry, and tissue mechanobiology. Many of these factors are unique to humans and specific to individuals; thus, experimental observations of deformation (strain) in vivo are both desirable and necessary for complementing existing experimental and numerical research.

With its exceptional soft tissue sensitivity, MRI has long been a cornerstone for brain morphological analysis and atlas generation [3]. It is also considered the gold standard for observation of soft tissue deformation in vivo via tagged acquisitions [4]. In MRI, 'tags' refer to an artificial magnetic pattern that moves with the tissue as it deforms—a technique that was developed for the heart, but also has been applied to the brain for observations of planar (2D) deformation under mild acceleration [5, 6]. MRI-based atlas generation has evolved from solely morphological averaging to multivariate and functional analyses. Researchers have constructed both anatomical atlases from intensity data, as well as structural and connectivity atlases [7]. Similar concepts have been used to average mechanical motion in the heart [8], and the change in brain morphology arising from brain tissue deterioration [9]. However, although planar displacements and strains from different individuals have been studied with principal component analyses (PCA) [5], and with low-order physical models [6], an atlas of spatiotemporal strain observations in 3D is not yet available.

In the past, we have introduced advances in acquisition and image processing that have enabled full-brain MRI coverage approximately within a two-hour imaging session, and provided the basis to define the strain tensor in spatiotemporal fields [10, 11]. Therefore, this study addresses the analysis and atlas generation of experimental observations of deformation in 4D (volume and time) across multiple individuals. This analysis will be useful for identifying idiosyncratic sensitivity to deformation. For example, correlation of strain patterns with respect to anatomical characteristics may reveal factors that determine susceptibility to TBI. Likewise, group patterns of deformation can be used as validation data for representative mechanical models. (Validation is a crucial step for gaining confidence in simulations aiming at investigating head accelerations that are too dangerous to be observed experimentally in vivo). Also, the measurements can serve as complementary information for interpreting experimental observations from animal or cadaveric TBI models.

Methods

This research combines MRI image acquisition, processing, and integration of strain results in a common template. Imaging information included anatomical, tagged and DT-MRI scans. The processing pipeline featured tissue labeling for identifying white matter, and motion estimation via harmonic phase analysis with finite elements (HARP-FE) [11]. During motion estimation, a finite element (FE) mesh (Fig. 1) was registered to each of the subjects to obtain kinematic information, and served as the template for atlas generation.

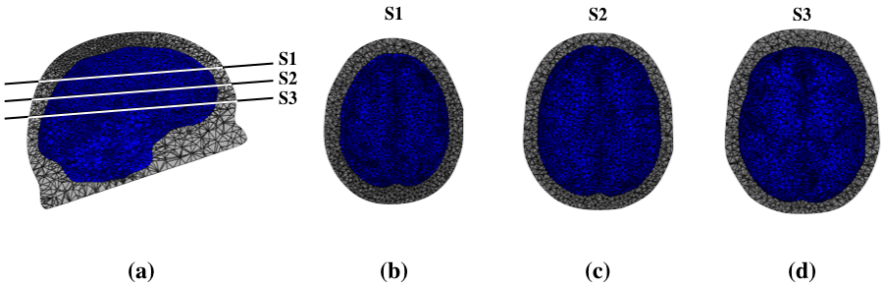

Fig. 1. FE mesh template. A modified version of the Colin27 adult brain atlas mesh [12] was registered to each of the subjects and used for motion estimation. The sagittal cross-section (a) shows the relative position of axial slices, labeled S1-S3 (b)-(c). All the cross-sectional slices show two domains corresponding to intra- and extracranial tissue.

Image Acquisition and Preprocessing

Human volunteers (n = 7, 4 males, and 3 females, 33.7 ± 6.5 years of age) were scanned with anatomical, diffusion, and tagged MRI pulse sequences. Informed consent was obtained from all participants of the study. Experimental protocols were approved by an institutional review board, according to ethical considerations and approved by overseeing authorities.

Imaging was performed in a Siemens Biograph mMR 3T instrument (Siemens, Erlangen, Germany). Anatomical scans consisted of 176 1mm-slices of 240 pixel × 240 pixel, 1 mm × 1 mm resolution with T1 contrast. The DT-MRI scan, performed to extract fiber directions in the white matter, consisted of 39 directions, 128 × 128 × 75 matrix size, 250 mm × 250 mm × 150 mm FOV, and a b-value 1000s/mm^2. Both, the T1 and the DT-MRI acquisition were obtained in either a 16- or 32-channel head coil. The tagged MRI acquisition occurred during a voluntary rotation towards the left shoulder. A MRI-compatible apparatus was used to guide the motion, as shown in Fig. 2 (a-b). After head rotation, movement came to a sudden stop producing a rotational acceleration of 209 ± 23 rad/s^2, depending on each volunteer's comfort, anatomy, and reflexes (Fig. 3c). An angular position sensor (Micronor, Camarillo, USA) was used to calculate angular acceleration.

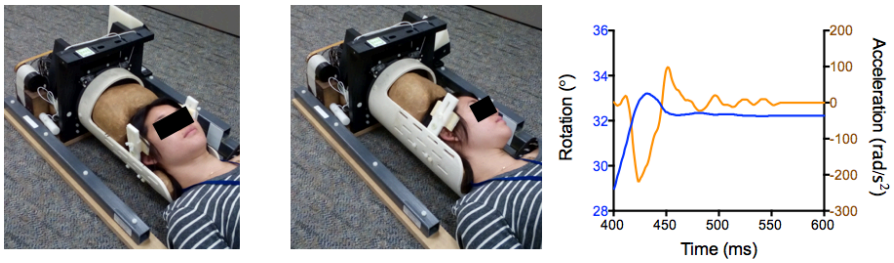

(a) **(b)** **(c)**

Fig. 2. Rotational motion apparatus. Both the volunteer and the apparatus fit inside the MRI bore. The device guides motion from a resting configuration (a) towards the left shoulder (b). An encoder attached to the rotating axis is used to obtain rotation and acceleration data (c).

The tagged acquisition comprised 13 time frames (18 ms TR). Each slice had 160 pixel × 160 pixel (1.5 mm × 1.5 mm), using a spatial modulation of magnetization (SPAMM) pulse sequence. The segmented acquisition of 24 *k*-space lines, 6 lines per segment, required 4 motion repetitions per slice. Acquisitions were performed using a 4-channel body coil plus a 2-channel spine coil. A total of 11—13 axial slices were used per direction, to encode motion from left to right, and from front to back (anteroposterior). Six additional slices oriented radially were used to encode motion form the inferior to the superior side of the head. The approximate configuration of the tagged slices and directions appears in Fig. 3 (a). Total acquisition time was less than 1.5 hours including anatomical, diffusion, and tagged imaging. More information regarding acquisition of tagged images, including motion triggering to reduce blurring and other artifacts, can be found in the literature [10].

Image volumes were preprocessed for motion estimation and strain measurement with respect to local fiber directions. Anatomical T1 scans were automatically labeled with a subject-specific sparse dictionary-learning algorithm (with default parameters) [13] to differentiate white matter, gray matter, and the cerebrospinal fluid (CSF). DT-MRI was processed (DSI studio, http://dsi-studio.labsolver.org) for identification of fiber directionality in the white matter. Tagged slices were interpolated into an intersecting volume via linear interpolation, which produced the best tracking accuracy against benchmarking data (next Section). The resulting volume had a resolution of 1.5 mm isotropic, and was filtered to extract harmonic phase volumes with a high-pass Fourier domain filter with cutoff at the tagging frequency (full cutoff after a 3-pixel quasi-linear slope). A typical outcome of the interpolation and filtering steps appear in Fig. 3 (b—c).

The first time frame of the tagged MRI sequence was defined as the global reference configuration. To compensate for imaging coil placement, the T1 image was rigidly registered to the tagged reference: This required tag removal in the tagged reference (via a notch filter placed at the tagging frequency), and Gaussian blurring to match resolutions (with σ = 10 mm set empirically). The registration results were used to align all anatomical data (labels, the FE mesh, and DT-MRI).

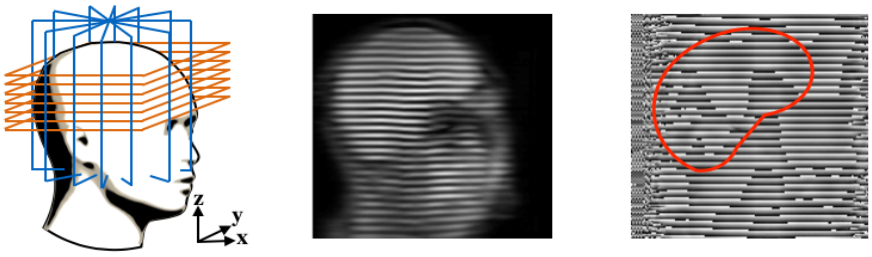

Fig. 3. Tagged MRI for motion estimation. Slices (a) were oriented axially and sagittaly. The axial slices were sensitized in the left-to-right (y), and the anteroposterior (x) directions, and the sagittal slices were used to measure motion in the inferosuperior (z) direction. For tracking, the slices were interpolated into volumes and filtered. A cut of the volume tagged along the z direction shows a tagged image (b), and a harmonic phase image (c) after filtering.

Displacement and Strain Estimation From Tagged MRI

Displacements associated with head motion were calculated by tracking the harmonic phase volumes using HARP-FE. This tracking technique was designed to provide displacements with three main features: compatibility (displacement fields are diffeomorphic), incompressibility, and rigid displacement of extra cranial tissue. To this end, the harmonic image volumes provide pseudo-forces that deform the FE domain from one time frame (the reference) to another (the target) [11].

The computational domain for HARP-FE was a modified version of the Colin 27 adult brain atlas mesh (Fig. 1) [12]. The mesh, 423,000 tetrahedral elements nodally integrated to prevent locking, was matched to each subject via iterative closest point affine registration of the surfaces around the cranial vault extracted from CSF labels [14]. (This transformation was applied to all the mesh nodes.) After registration, the maximum distance from the atlas surface to its subject-specific equivalent ranged within 1.9 and 2.4 mm. The original mesh domain assigned to the brain, and the results of a representative mesh registration are shown in Fig. 4.

Tracking was sequential from one frame to the next, and composition was used to pull results back to the global reference. By discarding intermediate stresses, the material model provides minimum regularization, and the imaging information has the largest influence on the deformation. As the images retain nonlinearities associated with the actual tissue motion, realistic material properties for the brain are not required for HARP-FE; instead, parameters were optimized for tracking convergence. The intra-cranial tissue (Fig. 2) was modeled as a Neo-Hookean solid with $C_1 = 1.0$ kPa, $\kappa = 100$ kPa. Tracking parameters included $\lambda_{\max} = 200$ mN/rad, and $\lambda_{\text{tol}} = 0.3$. Preprocessing and HARP-FE parameters were empirical-

ly calibrated using an open benchmarking dataset [15] (median tracking error of 1.1 ± 0.4 mm). Axonal bundle directionality in the white mater was obtained from the principal diffusion direction from DT-MRI, and transferred to the FE mesh via nearest-neighbor interpolation, which is common in computational modeling of fibers [16]. This information enabled calculation of strain in a local coordinate system i.e., stretch along the fiber direction (first diffusion eigenvector), and the net shear (the sum of shears associated with the second and third eigenvectors).

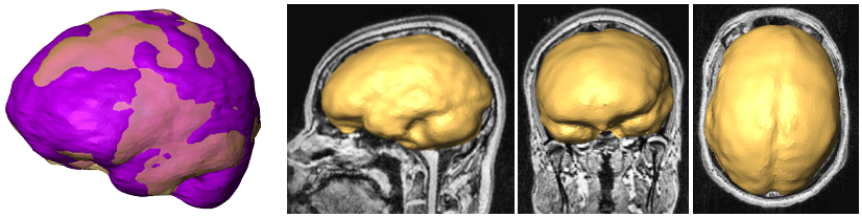

Fig. 4. Mesh matching. After registration, the template surface largely conforms to the target (a). Fit quality can be observed when comparing the intracranial mesh surface with the T1 image in sagittal (b), coronal (c), and axial views (d).

Individual observations of deformation were based on the maximum shear strain $\gamma_{\max}$ defined as one-half of the difference between the first and the third principal components of the Green-Lagrange strain tensor $\boldsymbol{E} = [\boldsymbol{F}^T\boldsymbol{F} - \boldsymbol{1}]/2$ (where $\boldsymbol{F}$ is the deformation gradient [17]). This metric was chosen due to its association with TBI [18]. To evaluate the relationship between individual deformation and acceleration, the spatial mean of $\gamma_{\max}$ was calculated at each time point and the largest values were compared against the acceleration peak of each experiment, or the product between acceleration and the subject's brain volume.

Group Analysis

This study made use of scalar-based analysis to avoid the challenges associated with tensorial interpolation [19]. In general, this can be achieved through analysis of strain tensor invariants, or scalars that arise from tensorial projection. The latter was the focus of the study.

For reference, the classic invariants from continuum mechanics [17], are defined with respect to the right Cauchy-Green strain tensor $\boldsymbol{C} = \boldsymbol{F}^T\boldsymbol{F}$ as

$$I_1 = \mathrm{tr}(\boldsymbol{C}), I_2 = I_1^2 - \mathrm{tr}(\boldsymbol{C}^2), \text{and } I_3 = \det(\boldsymbol{C})\ . \tag{1}$$

The physical interpretation of I_1 and I_2 is roughly associated with the mean hydrostatic and deviatoric deformation, and I_3 represents the relative volume change.

Here, brain motion is assumed to be incompressible, which is enforced by HARP_FE via the bulk modulus. (From a numerical perspective this is a "soft" constraint, but the expectation is that $I_3 \approx 1$.)

In this context, tensorial projection has explicit directionality assumptions. For instance, $\gamma_{\max}$ assumes that the largest shear deformations across subjects occur in similar directions (this is likely because the apparatus a repeatable motion). Likewise, two more quantities, can be defined using a local fiber direction $\boldsymbol{a}_0$. First,

$$I_4 = \boldsymbol{a}_0(\boldsymbol{C}\boldsymbol{a}_0)\,, \tag{2}$$

the local fiber stretch. Also, the coupling relationship

$$I_{\mathrm{a}} = \gamma_{\mathrm{a}} = \boldsymbol{a}_0(\boldsymbol{C}\boldsymbol{b}_0) + \boldsymbol{a}_0(\boldsymbol{C}\boldsymbol{c}_0)\,, \tag{3}$$

was used to describe the total fiber-shearing strain. Both I_4 and I_a were defined exclusively in the white matter and averaged as absolutes.

The atlas was built using the scalar quantities above, which are stored digitally either at the nodes or integration points of the mesh (which was shared across subjects). It is possible to approximate continuous random fields (each with a mean and a standard deviation) using interpolation via element shape functions. Thus, for a group of field samples ($n = 1,2,\dots,N$), expressions (1) to (3) yield a mean

$$\bar{I}_i(\boldsymbol{X},t) = \frac{1}{N}\sum_{n=1}^{N} I_i^n(\boldsymbol{X},t)\,, \tag{4}$$

(i is used to identify the expressions above), and standard deviation

$$s_i(\boldsymbol{X},t) = \sqrt{\frac{1}{N}\sum_{n=1}^{N}\left(I_i^n(\boldsymbol{X},t) - \bar{I}_i(\boldsymbol{X},t)\right)^2}, \tag{5}$$

defined as a function of the reference configuration $\boldsymbol{X}$, and time t.

Results and Discussion

Individual Patterns

Peak acceleration occurred the time of impact, which generally occurred two frames into the acquisition, Fig. 3(c). A representative example of acceleration-

induced brain deformation induced by a mild acceleration appears in Fig. 5. The largest values for $\gamma_{\max}$ occurred in the time frame after the highest acceleration. Note that the tracking algorithm ensures zero extracranial deformation.

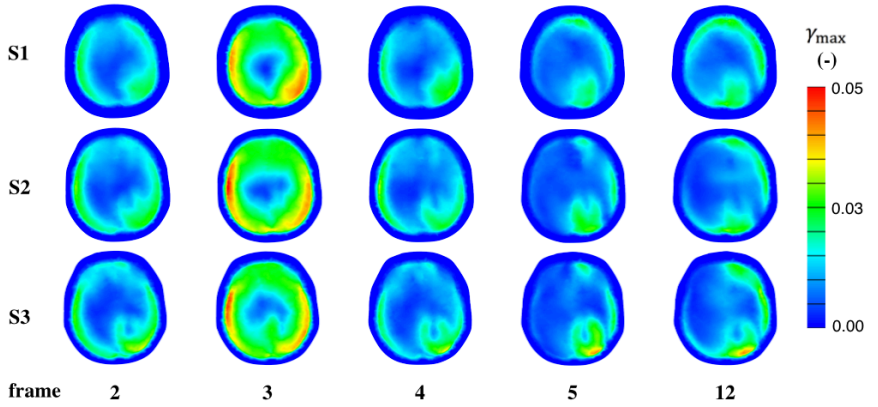

Fig. 5. Individual observations of maximum shear strain ($\gamma_{\max}$) in a single individual. Axial slices are labeled S1 through S3 from the most superior. Slice placement appears in Fig. 1. The patient's right appears on the right.

Midbrain slices from different volunteers at the time of highest acceleration are shown in Fig. 6. The distribution of $\gamma_{\max}$ included peaks around the skull particularly in temporal regions. There were relatively large differences in terms of magnitude of peak deformation, which spanned approximately 0.04. The center of the brain exhibited lower $\gamma_{\max}$ values, although this was not particularly true near the midline (except in v6), where areas of low deformation expanded laterally towards the ventricles. This lateral expansion may be evidence of the influence of the falx tentorium, which is thought to be involved in mechanical power transmission towards the center of the brain [20]. Differences in size and shape can be clearly seen, but no obvious relationships appear between these and the strain patterns. The individual measurement with the largest average percent volume change was $1\times10^{-2} \pm 2.2\times10^{-3}$ (which indicates nearly incompressible deformation).

Comparing the spatial average of $\gamma_{\max}$ (right after the time of impact) with the magnitude of the peak acceleration resulted in a loose relationship between deformation and acceleration with a coefficient of determination (R^2) of 0.34, Fig. 7a. However, weighting the acceleration values by the subject's brain volume, resulted in a more visible linear relationship with R^2= 0.66. This finding suggests that volume is an idiosyncratic factor related to propensity to deformation.

While the deformation field in Fig.5 is representative in that it exhibits some of the expected relationship between acceleration and deformation, it also shows counterintuitive behavior, as the strain measure does not reach zero in the last frame. This could be associated with the relatively short acquisition window (since dynamic behavior could continue), imaging artifacts (including accumulative error from sequential tracking), or the change in the relative direction of gravity [21].

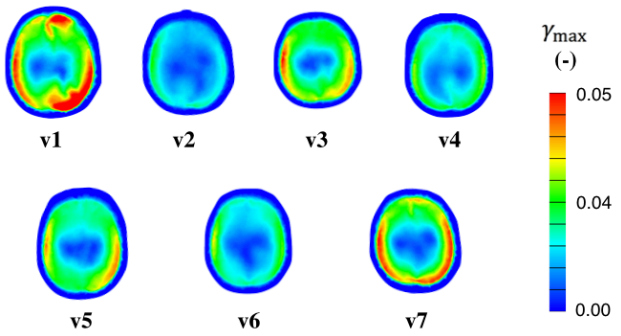

Fig. 6. Individual observations of maximum shear strain (γ_{max}) after the peak acceleration. In all of the volunteers (v1-v7), strain patterns were characterized by peaks around the skull, and lowered values near the center. The patient's right appears on the right.

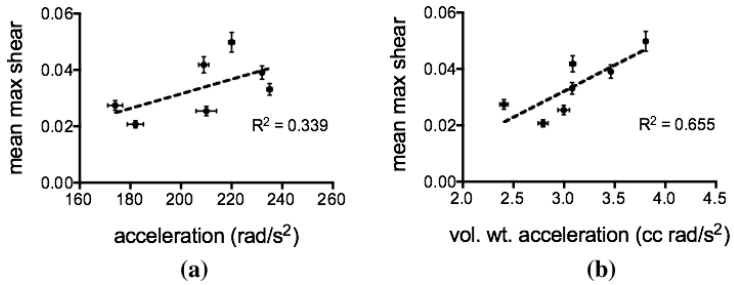

Fig. 7. Effect of acceleration on mean deformation. Although there is a loose relationship between acceleration and deformation (a), weighting peak acceleration by the subject's volume results in a clearer trend (b). Whiskers represent standard error.

Group-Based Deformation Patterns

A spatiotemporal atlas of γ_{max} (with no volume weighting) shown in Fig. 8, exhibits some of the visible features of the individual measurements (Fig. 6), including peak deformations around the cranium and the lateral expansion of regions of lowered deformation towards the ventricles. The standard deviation of strain measurements (spatially averaged) was 0.01 ± 0.02. Also, the spatial mean of $\bar{I}_3$ was $1\times10^{-2} \pm 2.2\times10^{-3}$ percent indicating nearly incompressible behavior.

Spatial averages of absolute fiber stretch and net fiber-shearing strain appear in Fig. 9. Compared to the magnitude of peak maximum shear strains, fiber deformations were lower. This is consistent with the pattern of deformation, because the white matter is deeper inside the brain (in relation to the cranial surface) where deformation was less. Fiber-shearing strain also exhibits larger peak values (at time frame 3) than fiber stretch.

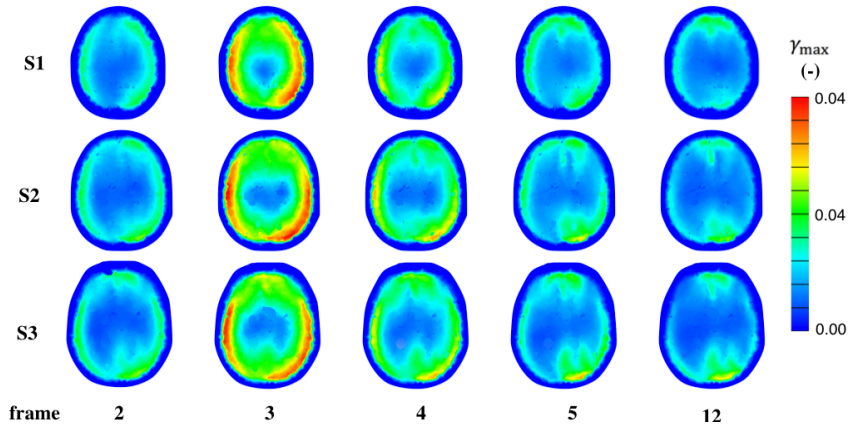

Fig. 8. Atlas of maximum shear strain (γ_{max}). Strain patterns were characterized by peaks around the skull, and lowered values near the center. The patient's right appears on the right.

As with the individual measurements, the results in the atlas exhibit some unexpected features, e.g. a strain concentration is present in the posterior right side in Fig. 8. It is possible that this behavior (similar patterns also appear in Fig. 5) points to the imaging artifacts resulting in non-zero strains at later times, or a phase shift due to fluid displacement. To improve motion estimation, and analysis of atlased results, future research includes finding a balance between regularization and tracking accuracy, and characterizing the effect of boundary conditions. Although HARP-FE was successfully validated against a displacement database [15], a strain benchmark could provide a more rigorous validation. Considering that elongations (of fibers or other tissues) at small strains fall below image resolution, the confidence in the measurement, to an extent, increases with the amount of strain limiting the accuracy of our results. Future research will also focus on implementing time alignment, and the design of confidence intervals based on variability. For instance, volume is associated with mass, which is a major component in inertial loading; thus, the observed relationship between average strain and volume (Fig. 7) suggests that strain variability across subjects, which was relatively large in this preliminary atlas, could be reduced by applying normalization.

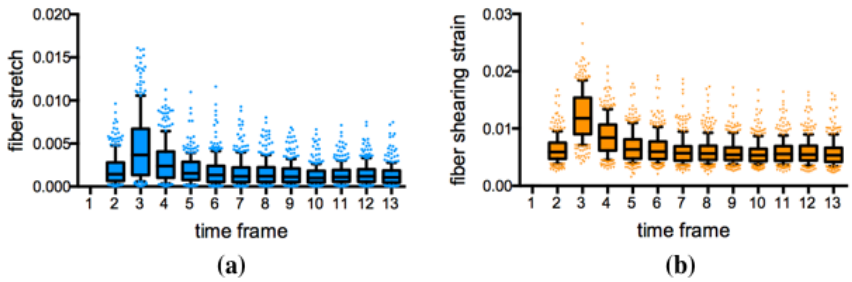

Fig. 9. Spatial averages of fiber stretch (a), and fiber-shearing strain (b) in the atlas. As expected peak deformation was seen after maximum acceleration in time frame 3.

Conclusion

This study introduced methodology and preliminary results associated with experimental observations of brain deformation after a mild acceleration. The novel spatiotemporal 3D measurements were incorporated in both individual and atlas-based analysis, including DT-MRI. Although the results exhibit some unexpected features, the general trends agree with the temporal evolution of acceleration, and follow logical relationships with respect to idiosyncratic factors (brain volume), and structural features (the falx). Future work includes refinement of motion estimation, additional validation, and study of variability.

Acknowledgments This research was funded by NIH Grant R01-NS055951, supplement PA12-149, and support by the Center for Neuroscience and Regenerative Medicine.

References

1. Shaw, N.A.: The neurophysiology of concussion. Prog. Neurobiol. 67, 281–344 (2002).
2. Siedler, D.G., Chuah, M.I., Kirkcaldie, M.T.K., Vickers, J.C., King, A.E.: Diffuse axonal injury in brain trauma: insights from alterations in neurofilaments. Front. Cell. Neurosci. 8, 429 (2014).
3. Dickie, D.A., Shenkin, S.D., Anblagan, D., Lee, J., Blesa Cabez, M., Rodriguez, D., Boardman, J.P., Waldman, A., Job, D.E., Wardlaw, J.M.: Whole brain magnetic resonance image atlases: a systematic review of existing atlases and caveats for use in population imaging. Front. Neuroinform. 11, 1 (2017).
4. Ibrahim, E.-S.H.: Myocardial tagging by cardiovascular magnetic resonance: evolution of techniques-pulse sequences, analysis algorithms, and applications. J. Cardiovasc. Magn. Reson. 13, 36 (2011).
5. Abney, T.M., Feng, Y., Pless, R., Okamoto, R.J., Genin, G.M., Bayly, P. V: Principal component analysis of dynamic relative displacement fields estimated from MR images. PLoS One. 6, e22063 (2011).
6. Laksari, K., Wu, L.C., Kurt, M., Kuo, C., Camarillo, D.C.: Resonance of human brain under head acceleration. J. R. Soc. Interface. 12, 331 (2015).
7. Peng, H., Orlichenko, A., Dawe, R.J., Agam, G., Zhang, S., Arfanakis, K.: Development of a human brain diffusion tensor template. Neuroimage. 46, 967–980 (2009).
8. Bai, W., Shi, W., de Marvao, A., Dawes, T.J.W., O'Regan, D.P., Cook, S.A., Rueckert, D.: A bi-ventricular cardiac atlas built from 1000+ high resolution MR images of healthy subjects and an analysis of shape and motion. Med. Image Anal. 26, 133–145 (2015).
9. Subsol, G., Roberts, N., Doran, M., Thirion, J.P., Whitehouse, G.H.:

Automatic analysis of cerebral atrophy. Magn. Reson. Imaging. 15, 917–27 (1997).
10. Knutsen, A.K., Magrath, E., McEntee, J.E., Xing, F., Prince, J.L., Bayly, P. V, Butman, J.A., Pham, D.L.: Improved measurement of brain deformation during mild head acceleration using a novel tagged MRI sequence. J. Biomech. 47, 3475–81 (2014).
11. Gomez, A.D., Xing, F., Chan, D., Pham, D., Prince, J.: Motion estimation with finite-element biomechanical models and tracking constraints from tagged MRI. In: Wittek, A., Joldes, G., Nielsen, P.M.F., Doyle, B.J., and Miller, K. (eds.) Computational Biomechanics for Medicine. pp. 81–90. Springer Nature, Cham, Switzerland (2017).
12. Collins, D.L., Zijdenbos, a P., Kollokian, V., Sled, J.G., Kabani, N.J., Holmes, C.J., Evans, a C.: Design and construction of a realistic digital brain phantom. IEEE Trans. Med. Imaging. 17, 463–468 (1998).
13. Roy, S., Carass, A., Prince, J.L., Pham, D.L.: Subject specific sparse dictionary learning for atlas based brain MRI segmentation. In: International Conference on Medical Image Computing and Computer-Assisted Intervention: Wokshop on Machine learning in Medical Imaging. pp. 108–115 (2010).
14. Kroon, D.-J.: Segmentation of the mandibular canal in cone-beam CT data, (2011).
15. Tobon-Gomez, C., De Craene, M., McLeod, K., Tautz, L., Shi, W., Hennemuth, A., Prakosa, A., Wang, H., Carr-White, G., Kapetanakis, S., Lutz, A., Rasche, V., Schaeffter, T., Butakoff, C., Friman, O., Mansi, T., Sermesant, M., Zhuang, X., Ourselin, S., Peitgen, H.O., Pennec, X., Razavi, R., Rueckert, D., Frangi, A.F., Rhode, K.S.: Benchmarking framework for myocardial tracking and deformation algorithms: An open access database. Med. Image Anal. 17, 632–648 (2013).
16. Vadakkumpadan, F., Arevalo, H., Ceritoglu, C., Miller, M., Trayanova, N.: Image-based estimation of ventricular fiber orientations for personalized modeling of cardiac electrophysiology. IEEE Trans. Med. Imaging. 31, 1051–60 (2012).
17. Spencer, A.J.M.: Continuum Mechanics. Dover Books, Essex (1985).
18. Zhang, L., Yang, K.H., King, A.I.: A proposed injury threshold for mild traumatic brain injury. J. Biomech. Eng. Eng. 126, 226–236 (2004).
19. Alexander, D.C., Pierpaoli, C., Basser, P.J., Gee, J.C.: Spatial transformations of diffusion tensor magnetic resonance images. IEEE Trans. Med. Imaging. 20, 1131–9 (2001).
20. Kumaresan, S., Radhakrishnan, S.: Importance of partitioning membranes of the brain and the influence of the neck in head injury modelling. Med. Biol. Eng. Comput. 34, 27–32 (1996).
21. Monea, A.G., Verpoest, I., Vander Sloten, J., Van der Perre, G., Goffin, J., Depreitere, B.: Assessment of relative brain-skull motion in quasistatic circumstances by MR imaging. J. Neurotrauma. 29, 2305–17 (2012).

Reconstruction of Real-World Car-to-Pedestrian Accident Using Computational Biomechanics Model: Effects of the Choice of Boundary Conditions of the Brain on Brain Injury Risk

Fang Wang[1, 2*], Bingyu Wang[1, 2], Yong Han[1, 2], Qian Peng[1, 2], Fan Li[3], Adam Wittek[4]

[1] School of Mechanical and Automotive Engineering, Xiamen University of Technology, Xiamen 361024, China

e-mail: wangfang@xmut.edu.cn

[2] Fujian Collaborative Innovation Center for R&D of Coach and Special Vehicle, Xiamen 361024, China

[3] College of Mechanical and Vehicle Engineering, Hunan University, Changsha 410082, China

[4] Intelligent System for Medicine Laboratory, School of Mechanical and Chemical Engineering, The University of Western Australia, Crawley-Perth 6009, Australia

Abstract: In the current study, the effects of the approach for modelling the brain-skull interface on prediction of the brain injury risk are investigated using a previously validated computational head-brain model. Four types of brain-skull interface modelling approaches (1: the method used in original Total HUman Model for Safety THUMS Head-brain model; 2: brain rigidly attached to the skull, 3: frictionless contact between the brain and skull, and 4: cohesive layer (spring-type) between the brain and skull) are employed in numerical reconstruction of a real-world car-to-pedestrian impact accident. The results indicate that the predicted brain injury risk is strongly affected by the approach for modelling the brain–skull interface. The comparison of the predicted risk of diffuse axonal injury DAI and brain contusions with the injuries sustained by the pedestrian involved in the accident seems to suggest that accurate prediction of the brain injury risk using computational biomechanics models requires direct representation of the meninges and subarachnoidal space with the CSF.

1. Introduction

Traumatic brain injury (TBI) affects around 10 million people worldwide every year and is associated with high risk of permanent disability and death [1]. Motor vehicle impacts are the second most important factor leading to the occurrence of

TBI [2]. To mitigate the TBI risk and to improve the countermeasures against this type of injury in motor vehicle impacts and similar loading environment, numerous attempts have been made to gain in-depth knowledge of human brain injury mechanism [3, 4], injury tolerance/threshold [5, 6], and injury criteria [7, 8]. These attempts used both experimental and computational biomechanics methods. By employing Post Mortem Human Subject (PMHS) and human/animal tissue samples, vast amount of biomechanical data (including brain injury response, brain tissue properties, etc.) were experimentally obtained [3, 8-13]. These data are often used in the development and validation of computational biomechanics models that became a widely-used tool in injury biomechanics research due to technical and ethical constraints associated with conducting experimental studies under loads resulting in injury [8, 14-19]. In particular, such models have played an important role in the investigation and prediction of organ and tissue level responses of the brain due to violent impact [8, 16, 17], and numerous human brain computational models have been built using finite element (FE) methods to facilitate such investigation and prediction [20-26]. Such models utilise different approaches for modelling the brain-skull interface — layers of tissues between the skull and the brain. Although the brain-skull interface determines the boundary conditions of the brain and exerts appreciable effects on predicting the brain responses [16, 27], and consequently the risk of brain injury, no consensus regarding selection of the approach for modelling of the brain-skull interface has been reached so far by the injury biomechanics research community.

Several experimental studies have been conducted to investigate the mechanical properties of pia-arachnoid complex (part of brain-skull interface) [28-30]. However, the quantitative data are still limited. This, together with complex and not yet fully-understood anatomical structure of the brain-skull interface, remains a barrier to improvement of the biofidelity of computational biomechanics models of the brain. Such models tend to rely on various simplifications and assumptions for modelling the brain-skull interface. Direct representation of the key anatomical components (such as dura, arachnoid, CSF and pia) of the brain-skull interface was used in some brain FE models, including the models developed at Wayne State University [26, 31], Total HUman Model for Safety THUMS by Toyota Central R&D Labs [32, 33], model by Yang [34], model by Al-Bsharat et al. [35], and SIMon model [8]. Examples of more simplified approaches include modelling the brain–skull interface using a sliding contact allowing no separation between the brain and skull [20], frictionless sliding contact between the brain and skull [12, 15], and no-slip interface allowing no relative movement between the brain and skull [14].

Relatively few focused research attempts have been made with the purpose of finding an answer to what are boundary conditions of the brain and how they should be modelled [16, 21, 36]. In particular, in our recent research [36], we investigated the effects of approach for modelling the brain-skull interface on prediction of the brain deformations due to violent impact by modelling the experiments on PMHS head specimens conducted by Hardy et al. [3]. However, from

the perspective of design of countermeasures against TBI, investigating the effects on the brain injury risk in actual motor vehicle accident would be more relevant and important. In this study, we perform such investigation through reconstruction of a real-world car-to-pedestrian impact accident using the experience gained from [36].

2. Methods

2.1 Description of the car-to-pedestrian impact accident

A real-world car-to-pedestrian impact was selected from the IVAC database (the In-Depth Investigation of Vehicle Accident in Changsha) initiated and established by Hunan University (Changsha, China) in 2006 with the purpose of collecting the on-site data on traffic accidents involving Vulnerable Road Users (VRUs). The IVAC database incorporates the traffic police and hospital data, which includes the information of how the accident occurred, VRUs' injuries due to the accident and injury treatment. A large number of accident data from this database have been used in related studies in the field of traffic accident analysis and injury prevention [34, 37-40].

In the current study, we analysed the accident in which a 50-year-old male pedestrian was hit on the body right-hand-side by a small passenger car (Volkswagen Jetta - China version, a very popular model in China). The car was travelling at a speed of around 40km/h before the emergency braking was applied (estimated from the vehicle braking mark on the road surface) and impacted the pedestrian crossing the street. The car windscreen was damaged in the lower corner on the driver's side due to the impact with the pedestrian head. According to the medical report, the pedestrian suffered the cerebral concussion and right temporal contusion, which correspond to the Abbreviated Injury Scale (AIS, the most commonly used injury code designed to quantify the severity of injury to the human body organs/segments) [41] of AIS=3 (AIS3), for the cerebral concussion and AIS=4 (AIS4), for the right temporal contusion. The information about the pedestrian and vehicle is in Table 2.1 and Table 2.2, respectively.

Table 2.1 The information about the pedestrian and overview of the accident

Age	Height (cm)	Weight (kg)	Direction (o'clock)	Speed (km/h) Vehicle/Pedestrian	Brake	Brain injury description
50	174	70	3	37/1.5*	Yes	Right temporal contusion, AIS 4 Cerebral concussion, AIS 3

* Confirmed through accident construction.

Table 2.2 The information about the vehicle involved in the accident

Vehicle type	Manufacturer	Vehicle model	Model year	Mounting mass (kg)	Dimension (mm)
Small Passenger Car	FAW-Volkswagen	Jetta	2001	1490	4428×1660×1420

2.2 Investigation of the effects of approach for modelling the brain-skull interface on predicted brain deformations and brain injury risk due to car-to-pedestrian accident

Investigation of the effects of approach for modelling the brain–skull interface on the prediction of the brain deformations and brain injury risk was conducted in two stages. In the first stage, we reconstructed the car-to-pedestrian impact following the information from IVAC accident database (see section 2.1) using a multibody (MB) subject-specific human body model that represented the pedestrian involved in the analysed accident (section 2.2.1) (Fig. 2.1). In the second stage, the actual parametric study of the effects of the approach for modelling the brain–skull interface was conducted using a FE head-brain model with the initial head orientation and head gravity centre initial velocity determined from the accident reconstruction (section 2.2.2).

2.2.1 Accident reconstruction

We reconstructed the accident described in section 2.1 using the subject-specific model implemented by means of the MADYMO multibody analysis package by TASS International Software and Services (Helmond, The Netherlands; https://www.tassinternational.com/madymo). MADYMO is arguably the most widely used MB analysis software package in injury biomechanics.

The subject-specific pedestrian MB model was created by scaling the validated pedestrian model by Yang et al. [42, 43] according to the anthropometric information from Table 2.1. The scaling was done using the Generator of Body Data (GEBOD) [44] available in the MADYMO package. The information about the vehicle (Volkswagen Jetta) is in Table 2.2. We used Volkswagen Jetta MB model from the study by Li and Yang [37].

The information about the initial (before the accident) velocity of the vehicle (including the pedestrian and vehicle movement direction), relative position of the pedestrian and vehicle before the accident, and the pedestrian posture were obtained from the IVAC accident database (Table 2.1 and Table 2.2). However, there is always some uncertainty regarding the parameters describing the situation before the accident obtained from IVAC and other databases. Therefore, the process

of accident reconstruction used in this study includes the “Calibration” step (Fig. 2.2). In this step, the parameters describing the prior-to-accident situation were calibrated so that the position/location of the pedestrian and vehicle as well as the areas/points of impact between the pedestrian and vehicle obtained from the accident reconstruction agree with those observed in the actual accident (as recorded in the IVAC database).

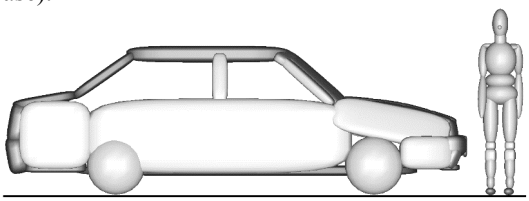

Fig. 2.1 Geometric set-up of the MB models of the pedestrian and car for accident reconstruction

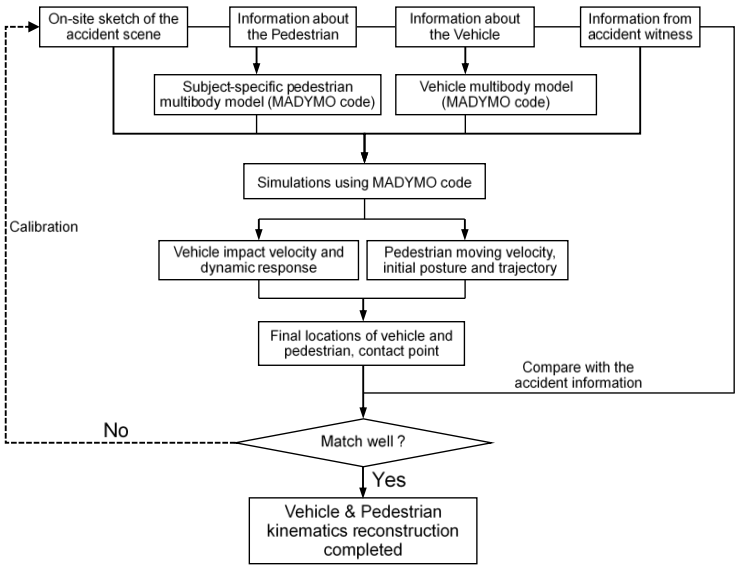

Fig. 2.2 Schematic of vehicle and pedestrian kinematics reconstruction of a real-world car-to-pedestrian accident used in this study

2.2.2 Investigation of the effects of approach for modelling the brain-skull interface on the brain injury

All simulations for investigation of the effects for modelling the brain-skull interface in this study were conducted using the LS-DYNA 971 non-linear explicit dy-

namic FE code by Livermore Software Technology Corporation LSTC (Livermore, CA, USA; http://www.lstc.com).

2.2.2.1 Modelling of impact between the pedestrian head and vehicle windshield

Initial conditions for the head-brain model The head orientation and linear and angular velocities of the head centre of gravity at the instant of contact between the pedestrian head and windshield were obtained from the accident kinematics reconstruction (Section 2.1).

Head-brain model Following our previous study [36], we used the head-brain model from Total HUman Model for Safety THUMS Version 4.0 by Toyota Central R&D Labs [32, 33]. The THUMS model includes the key anatomical structures such as scalp, skull, meninges, CSF, cerebrum, cerebellum, brain stem, falx and tentorium (Fig. 2.3-a). The brain tissues were modelled with linear viscoelastic material, and the strain rate dependency was included in the model [32].

Windshield model The windshield model developed and validated in the previous research [37, 45] was employed here. To represent the laminated glass structure of the vehicle involved in the analysed accident (Jetta 2001), the model consists of two coincident layers of shell element to represent the glass and the polyvinyl butyral PVB (Fig. 2.3-b). The glass layer was modelled using an elastic-plastic constitutive model with the plastic failure strain of 0.0012. For the PVB layer, a Mooney-Rivlin hyperelastic material model was used. The validation of the windshield model was carried out through an impact test, during which a standard EEVC adult headform impactor was propelled to hit the windshield, and comparing the acceleration history of the impactor model with the experimental data.

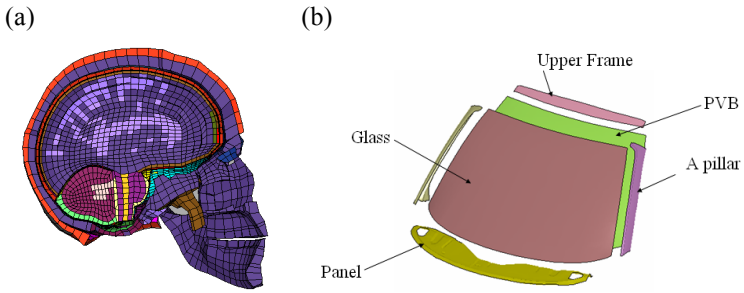

Fig. 2.3 (a) THUMS Version 4.0 head-brain model; (b) FE windshield model used in this study

2.2.2.2 Parametric study of the effects of approach for modelling the brain-skull interface

In THUMS Version 4.0 head-brain model, dura mater, arachnoid and pia mater are modelled with one layer of shell element [32, 33]. Tied contacts, allowing no relative movement, are defined between dura mater and skull, as well as between the dura and arachnoid. The cerebrospinal fluid CSF that fills the subarachnoidal space between the arachnoid and pia mater is simulated using a layer of 8-noded hexahedral element with fluid-like properties. Following our recent research [36], when investigating the effects of brain-skull interface modelling approach on the brain responses, the brain–skull interface model used in THUMS Version 4.0 head-brain was treated as the reference approach (Case 1 in Table 2.3). When conducting the parametric study, three other approaches were analysed: 1) The brain surface rigidly attached to the skull through tied contact interface which allows no movement between the brain outer surface and the skull inner surface (Case 2 in Table 2.3); 2) Frictionless sliding contact between the brain and skull (Case 3 in Table 2.3) which allows not only tangential movement but also separation between the brain and skull; and 3) A layer of spring-type cohesive element (no damping) between the brain and skull (Case 4 in Table 2.3).

To correlate the brain strain responses with injuries observed in real-world accidents, numerous tissue-level injury risk criteria have been proposed in the literature [7, 8, 17, 46-48]. As the analysed accident resulted in cerebral concussion (a commonly occurring diffuse axonal injury DAI) and temporal contusion, we used the following three injury criteria that are known to correlate well with these types of injury:

- Two strain-based injury criteria, cumulative strain damage measure CSDM [8, 17, 46-48] and maximum principal strain MPS [8] that have been widely used to assess DAI risk. CSDM is defined as the percentage of the cumulative volume of brain tissue experiencing principal strains higher than a predefined critical value (typically selected as 0.15 or 0.25) [47, 48].
- Dilatational damage measure DDM that was identified to exhibit a good correlation with the brain contusions [47]. DDM indicates the volume percentage of the brain tissue experiencing negative pressure levels exceeding specified threshold value during the impact [47]. Following the literature [47], in our study, the threshold was set at –14.7psi (equal to around –100kpa) which equals the water vapor pressure.

Following [36], to provide the information on the predicted brain deformations, we also report the quantile plots of the maximum principal strain and shear strain at the time when the maximum strain value was observed.

Table 2.3 Simulation matrix for studying the effects of approach for modelling the brain–skull interface

Approach	Original THUMS head-brain model	Brain rigidly attached to the skull	Frictionless contact between the brain and skull	Cohesive layer (spring-type) between the brain and skull
Simulations	Case 1	Case 2	Case 3	Case 4

3. Results

3.1 Accident reconstruction

The impacts between the pedestrian body segments and vehicle obtained using the accident reconstruction process explained in Fig. 2.2 occurred between the pedestrian's upper leg (thigh) and vehicle's left headlamp (Fig. 3.1-b), between the pelvis and bonnet (Fig. 3.1-c), and between the head and windshield (Fig. 3.1-d). These results are consistent with the observed car exterior damage (Fig. 3.1-e).

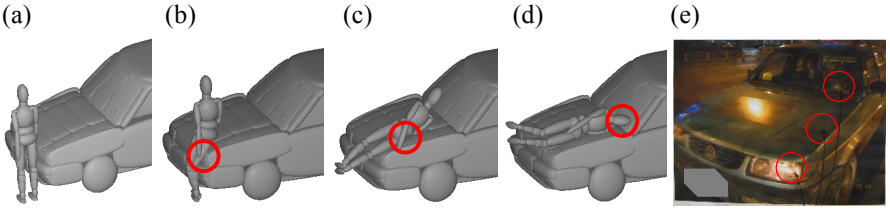

Fig. 3.1 Comparison of the results of accident reconstruction and location of deformations of the actual vehicle involved in the analysed accident. (a) initial pedestrian posture and position in relation to the car; (b) the predicted impact location between the pedestrian upper leg (thigh) and the left headlamp; (c) the predicted impact location between the pedestrian pelvis and the bonnet; (d) the predicted impact location between the pedestrian head and the windshield; (e) the impact locations at the accident scene

The predicted head linear and angular velocities and the pedestrian position relative to the windshield at the instant of impact with the windshield were used to define the initial conditions for the head model when predicting the brain responses. The analysis of these responses is presented in Section 3.2.

Fig. 3.2 below shows that the reconstructed (predicted) windshield fracture pattern agrees well with the windshield damage observed in the vehicle involved in

the analysed accident. This provides indirect confirmation of the accuracy of our accident reconstruction.

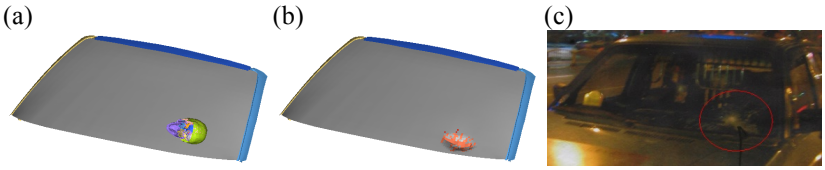

Fig. 3.2 Comparison of windshield damage predicted through the accident reconstruction (FE analysis) and actual damage in the vehicle in the analysed accident. (a) initial conditions for the pedestrian head model for simulation of the impact between the pedestrian head and vehicle windshield; (b) predicted fracture pattern of the windshield; (c) windshield fracture in the vehicle involved in the analysed accident

3.2 Investigation of effects of the approach for modelling the brain-skull interface on the brain injury

Boundary and initial conditions for the head model were defined from the IVAC accident database and accident reconstruction as described in Section 3.1.

The predicted injury Cumulative Strain Damage Measure CSDM — for both 0.15 and 0.25 thresholds, Maximum Principal Strain MPS, and Dilatational Damage Measure DDM criteria are reported in Table 3.1. For comparison with the information about the pedestrian injury in the IVAC database, they need to be expressed in terms of the risk of the DAI and brain contusions and AIS. We established the relationships between these injury criteria and DAI/brain contusions risk using the injury assessment risk curves reported in the literature [17, 47, 48].

For the CSDM, we used the curves by Takhounts et al. [47] (Fig. 3.3) and Marjoux et al. [17] (Fig. 3.4). Takhounts et al. [47] used the data from a series of animal experiments to calculate the CSDM values of different levels (prescribed critical principal strain set as 0.15 and 0.25) and built the logistic fit risk curves to predict the occurrence of DAI (Fig. 3.3). Marjoux et al. [17] analysed and reconstructed sixty-one real-world accidents involving pedestrian brain injury. They classified the DAI injuries observed in the accidents into two injury severity groups: 1) Moderate ($3 \leq AIS \leq 4$) and 2) Severe ($AIS=5$). From this classification, the risk curves as a function of $CSDM_{0.15}$ were built (Fig. 3.4). For MPS and DDM, we used the injury risk curves for DAI and brain contusions established by Takhounts et al. [47, 48], see Fig. 3.5 for MPS and Fig. 3.6 for DDM.

The predicted probability of the DAI injury occurrence was appreciably affected by the approach for modelling the brain-skull interface for all the injury criteria used (Fig. 3.3, 3.4, and 3.5). In particular, for the frictionless contact between the brain and skull (Case 3) and cohesive layer (spring-type) between the brain and

skull (Case 4), the probabilities of DAI predicted using the MPS criterion were over 80% which is much higher than for the remaining two approaches (Fig. 3.5). For the brain rigidly attached to the skull (Case 2), the DAI predicted using the MPS criterion was the lowest (Fig. 3.5). Similar tendency was observed for the CSDM criterion using the risk curves by Takhounts et al. [47] (Fig. 3.3), as one would anticipate, much higher risk for the principal strain threshold of 0.15 ($CSDM_{0.15}$) than for 0.25 ($CSDM_{0.25}$).

For the DAI injury risk curves by Marjoux et al. [17] (Fig. 3.4) and Cases 3 and 4 for modelling the brain-skull interface, the predicted $CSDM_{0.15}$ corresponded to 100% risk of occurrence of the DAI at the moderate and severe levels. For the brain rigidly attached to the skull (Case 2), no risk of DAI was predicted for the $CSDM_{0.15}$. For the approach used in the original THUMS head-brain model (Case 1), the predicted risk of severe DAI was around 50%.

For the injury risk curves by Takhounts et al. [47], the predicted DDM values corresponded to extremely low risk of the brain contusions for all the four approaches for modelling the brain-skull interface (Fig. 3.6). For Cases 1, 2 and 3, the predicted risk was virtually zero.

Table 3.1 The predicted brain injury criteria when changing the approach for modelling the brain-skull interface

Injury Criteria \ Case	Original THUMS head-brain model	Brain rigidly attached to the skull	Frictionless contact between the brain and skull	Cohesive layer (spring-type) between the brain and skull
$CSDM_{0.15}$	0.46	0.11	0.85	0.90
$CSDM_{0.25}$	0.16	0.02	0.46	0.66
MPS	0.98	0.68	1.47	2.18
DDM	0.002	0	0.0025	0.011

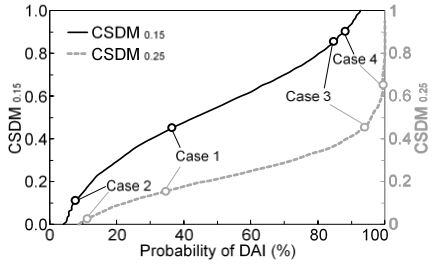

Fig. 3.3 _Predicted probability of the DAI occurrence for the car-to-pedestrian impact accident analysed in this study when varying the approach for modelling the brain–skull interface. The critical values of the probability were determined based on the logistic fit DAI risk curves for the injury criterion CSDM (with prescribed critical principal strain of 0.15 and 0.25) by [47]. Case 1, Case, Case 3 and Case 4 are different approaches for modelling the brain–skull interface (see Table 2.3)

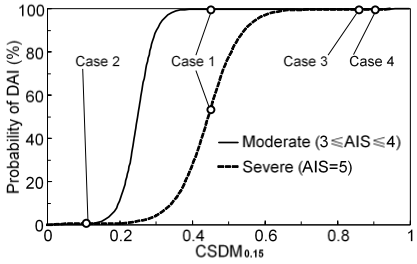

Fig. 3.4 Predicted probability of the DAI (Moderate and Severe) occurrence for the car-to-pedestrian impact accident analysed in this study when varying the approach for modelling the brain–skull interface. The critical values of the probability were determined based on the logistic fit DAI risk curves for the injury criterion CSDM (with prescribed critical principal strain of 0.15) by Marjoux et al. [17]. Case 1, Case, Case 3 and Case 4 are different approaches for modelling the brain–skull interface (see Table 2.3)

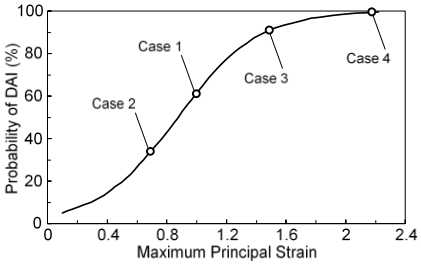

Fig. 3.5 Predicted probability of the DAI occurrence for the car-to-pedestrian impact accident analysed in this study when varying the approach for modelling the brain–skull interfaceThe critical values of the probability were determined based on the logistic fit DAI risk curve for the injury criterion MPS by [48]. Case 1, Case, Case 3 and Case 4 are different approaches for modelling the brain–skull interface (see Table 2.3)

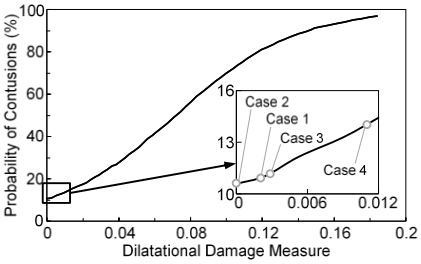

Fig. 3.6 Predicted probability of the brain contusion occurrence for the car-to-pedestrian impact accident analysed in this study when varying the approach for modelling the brain–skull interface. The critical values of the probability were determined based on the logistic fit brain contusions risk curve for the injury criterion DDM (with prescribed critical negative pressure of -100kpa) by [47]. Case 1, Case, Case 3 and Case 4 are different approaches for modelling the brain–skull interface (see Table 2.3)

The effects exerted by varying the approach for modelling the brain-skull interface on both the magnitude and the distribution of the principal strain and shear strain (Fig. 3.7) were consistent with those observed when predicting the risk of DAI and brain contusions (Fig. 3.3, 3.4, 3.5, and 3.6). The approach using the brain rigidly attached to the skull (Case 2) resulted in the smallest magnitude of both principal strain and shear strain. For the brain-skull interface modelled using a layer of cohesive elements (spring-type) between the brain and skull (Case 4), the predicted maximum strains were order magnitude (around 24 times higher) greater than for the approach using the brain rigidly attached to the skull (Case 2).

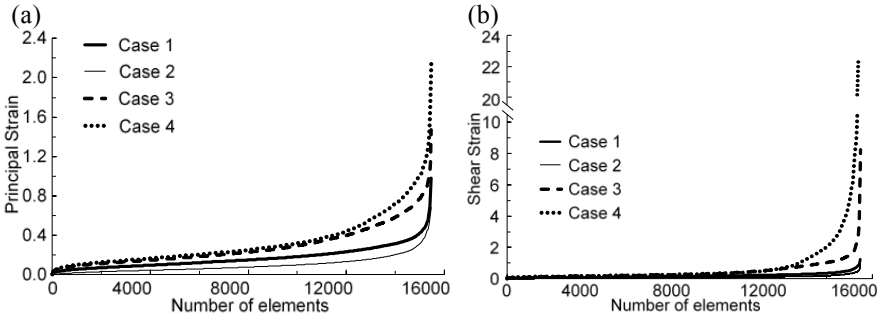

Fig. 3.7 Quantile plots of the principal strain (a) and shear strain (b) within the brain tissue, when changing the approach for modelling the brain-skull interface. See Table 2.3 for the details of the four simulations

4. Discussions and Conclusions

The results of this study indicate that the predicted severity of the brain injury (we focused on DAI) is appreciably affected by the approach for modelling the brain-skull interface (Fig. 3.3, 3.4, 3.5, and 3.6). Similar effects were observed for the predicted magnitude and distribution of the principal strain and shear strain within the brain parenchyma (Fig. 3.7). These findings are consistent with the results we previously reported in [36].

The results seem to suggest that accurate prediction of the brain responses due to violent impact using computational biomechanics models requires direct representation of the subarachnoidal space with the CSF (Case 1). This approach is used in THUMS Version 4.0 head-brain model (Fig. 2.3-a). It includes representation of key anatomical structures of the brain-skull interface. The approach using the brain rigidly attached to the skull through the tied contact interface (Case 2) seems to underestimate the brain injury severity. The fact that this approach allows no movement between the brain and skull might be a possible explanation to this underestimation. The modelling approaches using the frictionless contact between the brain and skull (Case 3) and a layer of cohesive elements (spring-type)

between the brain and skull (Case 4) seem to overestimate the brain injury severity. It should be noted, however, that the approach using a frictionless sliding contact between the brain and skull (Case 3) has been successfully used in the studies on predicting the brain deformations due to craniotomy (surgical opening of the skull) [18, 49].

Although evaluation of various brain injury criteria due to violent impact is not the primary purpose of the current study, comparison of the predicted using computational biomechanics model and observed (in the analysed accident) brain injuries (DAI and brain contusions) (Fig. 3.3, 3.4, and 3.5) appears to suggest that the cumulative strain damage measure CSDM criterion is a good predictor for the diffuse axonal injury DAI while the maximum principal strain MPS is an acceptable predictor. These findings are consistent with the results by Takhounts et al. [8, 48]. On the other hand, the dilatational damage measure DDM predicted very low brain injury severity (Fig. 3.6) for all approaches for modelling the brain-skull interface, which is inconsistent with the fact that the pedestrian involved in the analysed accident suffered from moderate brain contusion.

When investigating the effects of the approach for modelling the brain-skull interface on the predicted brain injury, the current study relies on the injury assessment risk curves that relate the injury criteria to the brain injury observed in a real-world car-to-pedestrian impact accident. To the best of our knowledge, such investigation has not been done before. However, the injury assessment risk curves reported in the literature [17, 46, 47] tend to exhibit appreciable differences (see Fig. 3.3 and Fig. 3.4). One possible reason for these differences can be the fact that the currently available accident databases are limited in a sense that they rarely contain complete accident information due to the technical constraints associated with collecting the data on the accident site. Expanding the accident data collection systems might be one possible solution to overcome this limitation.

Acknowledgements The research was supported by National Natural Science Foundation of China (Grant No. 51605407, 51505403), Fujian Provincial Department of Science and Technology (Grant No. 2017J01652), and State Administration of Foreign Experts Affairs P.R.China. All FE simulations using Total HUman Model for Safety THUMS Version 4.0 human body model and all the simulations for the accident reconstruction using MADYMO multibody code in this research were conducted at Xiamen University of Technology.

References

1. Fahlstedt M, Halldin P, Alvarez VS et al Influence of the body and neck on head kinematics and brain injury risk in bicycle accident situations. In: 2016 IRCOBI Conference Proceedings, Malaga, Spain
2. Gabler LF, Crandall JR, Panzer MB (2016) Investigating Brain Injury Tolerance in the Sagittal Plane Using a Finite Element Model of the Human Head. International Journal of Automotive Engineering 7:37-43

3. Hardy WN, Foster CD, Mason MJ et al (2001) Investigation of Head Injury Mechanisms Using Neutral Density Technology and High-Speed Biplanar X-ray. Stapp Car Crash J 45:337-368
4. Melvin JW, Lighthall JW, Kazunari U (1993) Brain-Injury Biomechanics. In: Nahum AM, Melvin JW (eds) Accidental Injury. Springer New York
5. Bain AC, Meaney DF (2000) Tissue-level thresholds for axonal damage in an experimental model of central nervous system white matter injury. J Biomech Eng 122:615-622
6. Zhang L, Yang KH, King AI (2004) A Proposed Injury Threshold for Mild Traumatic Brain Injury. J Biomech Eng 126:226-236
7. Kleiven S (2006) Evaluation of head injury criteria using a finite element model validated against experiments on localized brain motion, intracerebral acceleration, and intracranial pressure. Int J Crashworthiness 11:65-79
8. Takhounts EG, Craig MJ, Moorhouse K et al (2013) Development of brain injury criteria (BrIC). Stapp Car Crash J 57:243
9. Miller K, Chinzei K (2002) Mechanical properties of brain tissue in tension. J Biomech 35:483-490
10. Hardy WN (2007) Response of the human cadaver head to impact. Dissertation, Wayne State Univesity
11. Mazumder MMG, Miller K, Bunt S et al (2013) Mechanical properties of the brain–skull interface. Acta Bioeng Biomech 15:9
12. Agrawal S, Wittek A, Joldes G et al (2015) Mechanical Properties of Brain-Skull Interface in Compression. In: Doyle B, Miller K, Wittek A, Nielsen PMF (eds) Computational Biomechanics for Medicine. Springer International Publishing, New York
13. Nahum AM, Smith R, Ward CC (1977) Intracranial pressure dynamics during head impact. Stapp Car Crash J 21:339-366
14. Claessens M, Sauren F, Wismans J (1997) Modeling of the human head under impact conditions: a parametric study. SAE Technical Paper:No. 973338
15. Miller RT, Margulies SS, Leoni M et al (1998) Finite element modeling approaches for predicting injury in an experimental model of severe diffuse axonal injury. SAE Technical Paper:No. 983154
16. Wittek A, Omori K (2003) Parametric study of effects of brain-skull boundary conditions and brain material properties on responses of simplified finite element brain model under angular acceleration in sagittal plane. JSME International Journal 46:1388-1398
17. Marjoux D, Baumgartner D, Deck C et al (2008) Head injury prediction capability of the HIC, HIP, SIMon and ULP criteria. Accid Anal Prev 40:1135-1148
18. Wittek A, Joldes G, Couton M et al (2010) Patient-specific non-linear finite element modelling for predicting soft organ deformation in real-time: Application to non-rigid neuroimage registration. Prog Biophys Mol Biol 103:292-303
19. Wittek A, Grosland NM, Joldes GR et al (2016) From Finite Element Meshes to Clouds of Points: A Review of Methods for Generation of Computational Biomechanics Models for Patient-Specific Applications. Ann Biomed Eng 44:3-15

20. Zhang L, Yang KH, Dwarampudi R et al (2001) Recent advances in brain injury research: a new human head model development and validation. Stapp Car Crash J 45:369-394
21. Kleiven S, Hardy WN (2002) Correlation of an FE model of the human head with local brain motion: Consequences for injury prediction. Stapp Car Crash J 46:123-144
22. Yang J, Xu W, Otte D (2008) Brain injury biomechanics in real world vehicle accident using mathematical models. Chin J Mech, Eng-EN 32:81-86
23. Miller K, Wittek A, Joldes G et al (2010) Modelling brain deformations for computer-integrated neurosurgery. Int J Numer Meth Bio 26:117-138
24. Miller K (2011) Biomechanics of the brain. Springer, New York
25. Yang KH, King AI (2011) Modeling of the brain for injury simulation and prevention. In: Miller K (ed) Biomechanics of the Brain. Springer, New York
26. Mao H, Zhang L, Jiang B et al (2013) Development of a Finite Element Human Head Model Partially Validated With Thirty Five Experimental Cases. J Biomech Eng 135:111002
27. Bayly PV, Clayton EH, Genin GM (2012) Quantitative Imaging Methods for the Development and Validation of Brain Biomechanics Models. Annu Rev Biomed Eng 14:369-396
28. Jin X (2009) Biomechanical response and constitutive modeling of bovine pia-arachnoid complex. Dissertation, Wayne State University
29. Jin X, Yang KH, King AI (2011) Mechanical properties of bovine pia–arachnoid complex in shear. J Biomech 44:467-474
30. Jin X, Mao H, Yang KH et al (2014) Constitutive modeling of pia–arachnoid complex. Ann Biomed Eng 42:812-821
31. Mao H, Zhang L, Yang KH et al (2006) Application of a finite element model of the brain to study traumatic brain injury mechanisms in the rat. Stapp Car Crash J 50:583
32. Shigeta K, Kitagawa Y, Yasuki T Development of next generation human FE model capable of organ injury prediction. In: International Technical Conference on the Enhanced Safety of Vehicles (ESV), Stuttgart, Germany
33. Watanabe R, Miyazaki H, Kitagawa Y et al Research of collision speed dependency of pedestrian head and chest injuries using human FE model (THUMS version 4). In: Proceedings of 22nd Enhanced Safety of Vehicles (ESV) conference, Washington DC, USA
34. Yang J (2011) Investigation of brain trauma biomechanics in vehicle traffic accidents using human body computational models. In: Wittek A, Nielsen PMF, Miller K (eds) Computational Biomechanics for Medicine. Springer
35. Al-Bsharat AS, Hardy WN, Yang KH et al Brain/skull relative displacement magnitude due to blunt head impact. In: Proceedings of the 1999 43rd Stapp Car Crash Conference, San Diego, CA, USA
36. Wang F, Geng Z, Agrawal S et al (2017) Computation of Brain Deformations Due to Violent Impact: Quantitative Analysis of the Importance of the Choice of Boundary Conditions and Brain Tissue Constitutive Model. In: Wittek A, Joldes G, Nielsen PMF, Doyle BJ, Miller K (eds) Computational Biomechanics for Medicine. Springer, New York

37. Li F, Yang J (2010) A study of head–brain injuries in car-to-pedestrian crashes with reconstructions using in-depth accident data in China. Int J Crashworthiness 15:117-124
38. Nie J, Yang J (2014) A study of bicyclist kinematics and injuries based on reconstruction of passenger car–bicycle accident in China. Accid Anal Prev 71:50–59
39. Nie J, Li G, Yang J (2015) A Study of Fatality Risk and Head Dynamic Response of Cyclist and Pedestrian Based on Passenger Car Accident Data Analysis and Simulations. Traffic Inj Prev 16:76-83
40. Kong C, Yang J (2010) Logistic regression analysis of pedestrian casualty risk in passenger vehicle collisions in China. Accid Anal Prev 42:987-993
41. AAAM (2008) Abbreviated Injury Scale 2005, Update 2008. Association for Advancement of Automatic Medicine, Barrington, USA
42. Yang J (1997) Injury biomechanics in car-pedestrian collisions: Development, validation and application of human-body mathematical models. Dissertation, Chalmers University of Technology
43. Yang J, Lövsund P, Cavallero C et al (2000) A Human-Body 3D Mathematical Model for Simulation of Car-Pedestrian Impacts. Traffic Inj Prev 2:131-149
44. TNO (2013) MADYMO Utilities Manual, Version 7.5. TASS International, Helmond, The Netherlands
45. Yao J, Yang J, Otte D (2008) Investigation of head injuries by reconstructions of real-world vehicle-versus-adult-pedestrian accidents. Safety Sci 46:1103-1114
46. Bandak FA, Zhang AX, Tannous RE et al SIMon: a simulated injury monitor; application to head injury assessment. In: International Technical Conference on the Enhanced Safety of Vehicles, Amsterdam, The Netherlands
47. Takhounts EG, Eppinger RH, Campbell JQ et al (2003) On the Development of the SIMon Finite Element Head Model. Stapp Car Crash J 47:107-133
48. Takhounts EG, Ridella SA, Hasija V et al (2008) Investigation of traumatic brain injuries using the next generation of simulated injury monitor (SIMon) finite element head model. Stapp Car Crash J 52:1-31
49. Hu J, Jin X, Lee JB et al (2007) Intraoperative brain shift prediction using a 3D inhomogeneous patient-specific finite element model. J Neurosurg 106:164-169

Computational Modeling of Fluid-Structure Interaction between Blood Flow and Mitral Valve

Weixin Si[1], Xiangyun Liao[2*], Jing Qin[1], Pheng Ann Heng[2,3]

1 School of Nursing, The Hong Kong Polytechnic University, Hong Kong, China

2 Shenzhen Key Laboratory of Virtual Reality and Human Interaction Technology, Shenzhen Institutes of Advanced Technology, Chinese Academy of Sciences, Shenzhen, China

3 Department of Computer Science and Engineering, The Chinese University of Hong Kong, Hong Kong, China

* Corresponding author: xyunliao@gmail.com

Abstract— Mitral valve repair is a complex operation, in which the functionality of incompetent mitral valve is reconstructed by surgical techniques. Simulation-based surgical planning system, allowing surgeons to simulate and compare potential repair strategies, could greatly improve surgical outcomes. This paper presents a practical computational framework, combining the Total Lagrangian Explicit Dynamics Finite Element Method (TLED FEM) and Smoothed Particle Hydrodynamics (SPH), to solve the interaction problem of blood and immersed mitral valves. With this completed pipeline, we can not only predict the mechanical behavior of mitral valve, but also analyze the transvalvular pressures distributed on valve leaflets. The experimental results demonstrate that our method has the potential to be applied in surgical planning simulator of mitral valve repair.

1 Introduction

Mitral valve (MV) disease is one of the most common heart valve diseases, with a prevalence sharply increasing with age [1]. Surgical repair of MV results in better outcomes than valve replacement, yet diseased valves are often replaced due to the technical difficulty of the repair process, and outcomes are highly dependent upon the experience of surgeons [2]. Studies show that experienced surgeons at large clinical centers have a much better record of successful MV repairs, and valve replacement is often chosen instead of repair at low volume centers [3].

MV repair is normally performed during open heart surgery when the heart is emptied of blood and the valves are motionless, making it difficult for the surgeon to know how a given surgical modification will translate into valve function after the heart has been closed and blood flow restored. Simulation based surgical planning system has been proposed as a way to improve surgical outcomes. Under the proposed scheme, pre-operative images of computed tomography (CT), magnetic resonance imaging (MRI) or ultrasonic cardiogram are acquired, and a computational mesh of the malfunctioning MV is generated by reconstructing the segmentation results of the pre-operative images. The surgeons explore potential repair strategies on the virtual MV model then use simulation to predict the closure state of MV. For this surgical planning environment to be of practical use to a surgeon, simulations must be fast, not more than a few minutes per MV closing cycle, so that multiple surgical repair strategies could be simulated in succession, with feedback from one simulated repair guiding the subsequent simulated repair in an iterative process. On the other hand, Fluid structure interaction (FSI) models are necessary for comprehensive analysis of MV physiology [4]. The coupled FSI mitral model can provide a unique opportunity to assess both the mechanical effect of repair techniques, as well as the effect on fluid flow, in both the diastolic and the systolic phase, in the setting of MV pathology [5].

2 Related work

Modeling and simulation of the human body by means of continuum mechanics has become an important tool in medical and clinical diagnosis, computer-assisted surgeries, and surgery training and planning systems. Especially during highly complex surgical operations, such as MV repair, requiring an in-depth experience and medical expert knowledge, simulations have the potential to provide the surgeons with additional information. However, from the medical and surgical viewpoint, the theoretical applicability and the usefulness of intraoperative simulations are controversially discussed. Mostly, the high complexity of simulation algorithms causes a lack of real-time capability [6], which is essential for an intraoperative application. Many computational methods have been proposed to study the biomechanical behavior of MV during surgical repair. Among which FEMs have been able to tackle and provide powerful insights into clinically relevant patient-specific situations [7], [4], [8], while mass-spring models (MSMs) have been applied to heart valve modeling to provide real-time simulations [9], [10], [11]. Besides, 3D FSI models are computationally expensive and for that their application has, for the most part, been restricted to study native and prosthetic valves placed in simplified domains, e.g. straight axisymmetric aortic lumens [12]. More recently, attempts to investigate the coupled interaction of valves with the complex hemodynamic environment of the left ventricle in anatomic, patient-specific domains have also begun to emerge [13].

Fluid-structure interaction between blood flow and mitral valve has been an essential issue for modeling the mechanical behaviors of mitral valve. Researchers are focusing on computational analysis of mitral valve dynamics for the purpose of better understanding mitral valve disease and planning personalized surgery. Einstein et al. [14] presented a comprehensive strategy for carrying out a Lagrangian FSI based predictive analysis of mitral valve disease of ischemic regurgitation, integrating ex-vivo MRI image processing, geometry-based deformable registration and validation. The fully Lagrangian interface allows the exact imposition of boundary conditions and provides a path towards boundary layer meshing, a difficult task for embedded or immersed interface methods. Lau et al. [15] proposed to use an anatomically sized model of the mitral valve to compare the difference between structural and fluid–structure interaction techniques in two separately simulated scenarios: valve closure and a cardiac cycle, where the valve has been modelled separately in a straight tubular volume and in a U-shaped ventricular volume during fluid–structure interaction. Mittal et al. [16] reviews the current status and future outlook of the computational modeling of cardiac hemodynamics, including the blood flow modeling and fluid-structure interaction within heart, which can be deployed to greatly enhance existing diagnostic procedures as well as to assess options in treatment and cardiac surgery. Otani et al. [17] proposed an alternative computational approach to perform personalized blood flow analysis and fluid-structure interaction by providing the three-dimensional left atrium (LA) endocardial surface motion estimated from patient-specific cardiac CT images, to develop a clinically feasible methodology to perform personalized blood flow analysis within the heart. Their personalized FSI analysis in LA is a clinically feasible methodology that can be used to improve the understanding of the mechanism of intracardiac thrombosis and stroke in individual patients with LA structural remodeling.

3 Basics

3.1 Mitral valve dynamics

In this paper, we used the TLED FEM [18] to model the dynamics of mitral valve, since all derivatives with respect to spatial coordinates are calculated with respect to the original configuration and therefore can be precomputed. Soft tissues are often modeled using viscoelastic deformation laws, and usually includes dynamics, which leads eventually to a similar mathematical matrix formulation:

$$\mathbf{M}\ddot{\mathbf{u}}_t + \mathbf{D}\dot{\mathbf{u}}_t + \mathbf{K}\mathbf{u}_t = \mathbf{f}_{s \leftarrow f} \tag{1}$$

where t is the time step, $\mathbf{u}_t$ is the current nodes' displacements, $\mathbf{M}$ is the mass matrix, $\mathbf{D}$ is the damping matrix, $\mathbf{D} = \alpha\mathbf{M}$, $\mathbf{K}$ is the global stiffness matrix and $\mathbf{f}_{s\leftarrow f}$ is the current applied force field.

3.2 Smoothed particle hydrodynamics

Smoothed particle hydrodynamics (SPH) [19] is to use a smoothing kernel to approximate field quantities at arbitrarily distributed discretization particles and move these particles with their local velocity. For one particle i at position $\mathbf{x}_t$, its field quantity $A(\mathbf{x}_i)$ can be represented by a weighed sum of contributions from all neighboring particles within a cutoff distance h:

$$\langle A(\mathbf{x}_i)\rangle = \sum_j A(\mathbf{x}_j)\frac{m_j}{\rho_j}W(\mathbf{x}_{ij}, h) \tag{2}$$

where $\mathbf{x}_{ij} = \mathbf{x}_j - \mathbf{x}_i$, m_j and ρ_j denote the mass and density of neighboring particle j, and $A(\mathbf{x}_j)$ is the field quantity at particle j. The function $W(\mathbf{x}_{ij}, h)$ is referred to the smoothing kernel.

4 Methodology

To model the fluid-structure interaction between blood flow and mitral valve, we propose a practical computational framework consisting of embedded model based deformation, Casson equation based non-Newtonian blood modeling, blood-MV interaction and mechanical interactions between valve leaflets. With the proposed framework, we can realistically simulate the dynamic behaviors of mitral valve and evaluate the blood flow status for surgical planning, which allows surgeons to compare potential repair strategies and could greatly improve surgical outcomes. The overview of the proposed framework can be illustrated in Figure 1.

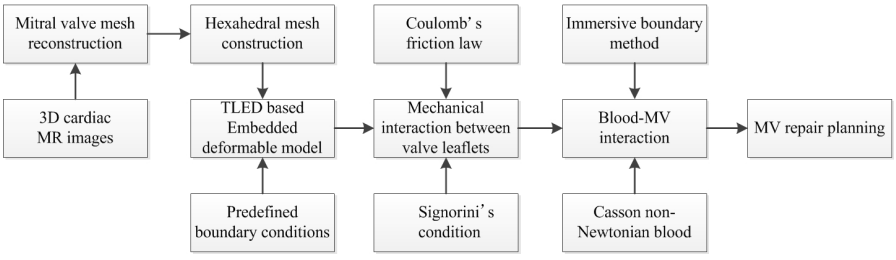

Fig. 1. Overview of the proposed framework.

4.1 Embedded deformable model

During the simulation of mitral valve repair, high degree of morphological detail must be preserved to represent the valve structure accurately. In this paper, we resolve the complicated simulation domain by the TLED FEM based embedded deformable model which constructed on a set of coarser hexahedron [20].

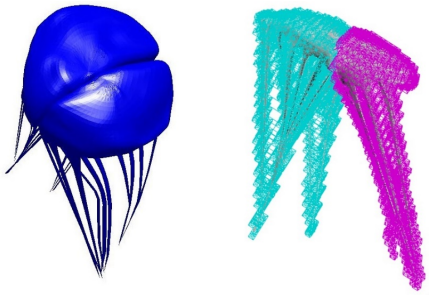

Fig. 2. Mitral valve and hexahedral model

Here the MV surface model was reconstructed with the manually segmented results of cardiac MR images of a patient using adaptive skeleton climbing method [23]. Then we generate coarse resolution hexahedra for the mitral valve. The embedded deformable model can efficiently compute the deformation of complex mitral valve mesh by first solving TLED FEM based embedded hexahedron deformation and then project the deformation to the mitral valve surface via mean value coordinates [24]. In addition, the embedded deformable model can provide the internal structure for the mitral valve, and the uniformly well-conditioned hexahedra mesh is beneficial for long time stability. Figure 2 illustrates the mitral valve surface model and corresponding embedded deformable model.

4.2 Casson non-Newtonian blood

The motion of blood can be described with Navier-Stokes equation:

$$\frac{d\mathbf{v}}{dt} = \frac{-\nabla p}{\rho} + \frac{\nabla \cdot \boldsymbol{\tau}}{\rho} + \mathbf{f}_{f \leftarrow s} \tag{3}$$

where $\mathbf{v}$, ρ, p, $\mathbf{f}_{f \leftarrow s}$ are the velocity, density, pressure and external force respectively, $\nabla \cdot \boldsymbol{\tau}$ describes the viscosity force, $\boldsymbol{\tau}$ is deviatoric stress tensor $\boldsymbol{\tau} = \upsilon \dot{\gamma}$, υ is fluid viscosity and $\dot{\gamma}$ is strain rate tensor, $\dot{\gamma} = (\nabla v + (\nabla v)^T)/2$.

For common Newtonian fluid, the viscosity υ is a constant. However, blood is a kind of non-Newtonian fluid that is mainly made up of erythrocyte and plasma, which is neither uniform nor Newtonian. The most common model to describe blood would be the Casson equation, which can be described as:

$$\upsilon = \boldsymbol{\tau}\dot{\gamma}^{-1} \tag{4}$$

where $\boldsymbol{\tau} = (\sqrt{\eta}\sqrt{\dot{\gamma}} + \sqrt{\tau_y}(1-e^{-n|\dot{\gamma}|}))^2$ and η is the Casson viscosity and $\eta = \rho\mu$. τ_y is the shear yield stress, μ denotes the kinematic viscosity. Here $1-e^{-n|\dot{\gamma}|}$ is introduced to avoid υ becoming a singular value when strain rate is small. n is a finite positive integer, here we set $n = 100$. The constitutive equation of Casson equation can be deduced from Eq. (4):

$$\upsilon(\dot{\gamma}) = \frac{(\sqrt{\eta}\sqrt{\sqrt{2D_\Pi}} + \sqrt{\tau_y}(1-e^{-n\sqrt{2D_\Pi}}))^2}{\sqrt{2D_\Pi}} \tag{5}$$

where D_Π is the second invariant of $\dot{\gamma}$.

In this paper, we approximate the blood equations by SPH discretized formula.

$$\nabla \mathbf{v}_i = \sum_j \frac{m_j}{\rho_j} \nabla W(\mathbf{x}_{ij}, h)(\mathbf{v}_{ji})^T \tag{6}$$

where $W(\mathbf{x}_{ij}, h)$ is the cubic spine kernel. The stress term in Eq. (3) is defined as:

$$\frac{1}{\rho_i}\nabla \cdot \boldsymbol{\tau}_i = \sum_j \frac{m_j}{\rho_i \rho_j}(\boldsymbol{\tau}_i + \boldsymbol{\tau}_j)\nabla W(\mathbf{x}_{ij}, h) \tag{7}$$

4.3 Blood-MV interaction

The dynamical movement of the mitral valve leaflets induce the boundary conditions for the FSI analysis, forcing the blood flow along its right path. To model the dynamic behavior of mitral valve, here we predefine boundary conditions for the mitral valve to provide the driving forces for blood flow.

Inspired by the immersed boundary method [21], we propose a new method that is adaptive to our embedded deformable model of mitral valve and SPH-based blood model to handle the complex blood-MV interactions based immersed boundary method, which enables the elastic boundary mitral valve changes the blood flow and the blood moves the elastic boundary simultaneously. At each time step, for blood particle i, we calculate the volume of each SPH blood particle j that inside the embedded hexahedron as the immersed volume domain to calculate the coupling force between immersed bodies with elastic boundaries and fluid as follows,

$$\mathbf{f}_{s\leftarrow f,i}\Delta t = \sum_j \rho_j V_j \mathbf{v}_i \delta(\mathbf{x}_{ij}) \tag{8}$$

where ρ_j is the density of particle j, V_j is the volume, $\mathbf{v}_i$ is the velocity of particle i, $\mathbf{x}_{ij}$ is the displacement between particle i and j, $\delta(\mathbf{x}_{ij})$ is the sec-

ond-order accurate Peskin function, which is to determine the velocity along the radial direction:

$$\delta(\mathbf{x}_{ij}) = \begin{cases} \frac{1}{4h}\left[1+\cos\left(\frac{\pi \| \mathbf{x}_{ij} \|}{2h}\right)\right] & \| \mathbf{x}_{ij} \| < 2h \\ 0 & \| \mathbf{x}_{ij} \| \geq 2h \end{cases} \tag{9}$$

The symmetric coupling force from a boundary particle to a fluid particle is

$$\mathbf{f}_{f \leftarrow s} = -\mathbf{f}_{s \leftarrow f} \tag{10}$$

Furthermore, the force distribution of SPH particle can be formulated as

$$\mathbf{f}_j = -\frac{\delta(\mathbf{x}_{ij})}{\sum_j \delta(\mathbf{x}_{ij})} \mathbf{f}_{s \leftarrow f} \tag{11}$$

where $\mathbf{f}_j$ is the distributed force of sampled point j.

4.4 Mechanical interactions between valve leaflets

During the cardiac cycle, the valves incorporate two leaflets, which are pushed open to allow blood flow and then close together to seal and prevent back-flow. To model the dynamic behaviors of two leaflets, we adopt the bounding volume hierarchy (BVH) to handle interaction between two valve leaflets. Then, we resolve the frictional contact problems between interacting valve leaflets through the following Coulomb's friction law with Signorini's condition.

$$\begin{cases} 0 \leq \delta_N \perp \mathbf{f}_N \geq 0 & \textit{Signorini} \quad \textit{condition} \\ \delta_T = 0 \Rightarrow \|\mathbf{f}_T\| \leq \mu \|\mathbf{f}_N\| & \textit{Sticking} \quad \textit{mode} \\ \delta_T \neq 0 \Rightarrow \mathbf{f}_T = -\mu \|\mathbf{f}_N\| \delta_T / \|\delta_T\| & \textit{Sliding} \quad \textit{mode} \end{cases} \tag{12}$$

where δ_N and δ_T are the normal and tangential gap in the contact space, and $\mathbf{f}_N$ and $\mathbf{f}_T$ are their corresponding forces. μ is the coefficient of kinetic friction.

5 Results

Our experimental platform is Intel(R) Xeon(R) E5-2640 2.60HZ CPU, 64GB memory and NVIDIA GeForce GTX TITAN X, 12GB memory. In order to reduce the complexity, certain aspects of the MV model have been simplified: the valve leaflets and chordae tendineae have been modeled as linear elastic materials, neglecting their non-linear constitutive behavior and anisotropy, and the surrounding tissues (including the ventricular muscle) have been assumed to be rigid.

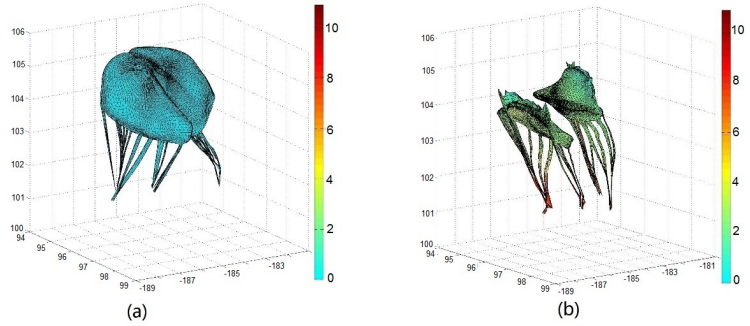

Fig. 3. Mitral valve closure and open. Hexahedral resolution of anterior leaflet and posterior leaflet is 38 × 33 × 32 and 36 × 29 × 36. Young's modulus of anterior leaflet, posterior leaflet and chordae are 6.233 MPa, 2.087 MPa and 0.660 MPa respectively. [4]

In our experiments, we first simulate the dynamic behavior of mitral valve in cardiac cycle. Figure 3(a) and Figure 3(b) are the motion states of mitral valve in systole and diastole phase respectively, where the color bar represents nodal displacement. In systole phase, the mitral valve leaflets close to prevent the blood from going back to the atrium. Two deformable leaflets are contact with each other without interpenetration by applying Signorini contact model. In diastole phase, the leaflets open as the blood enters the left ventricle. In the experiment, the time step is 0.005, we have simulated the MV dynamic behavior for 1600 frames in 8 seconds. We have achieved real-time computation of 200 fps in dynamic behavior simulation of mitral valve, which enables real-time interactive surgical planning of mitral valve repair and test its capability for normal closure and open.

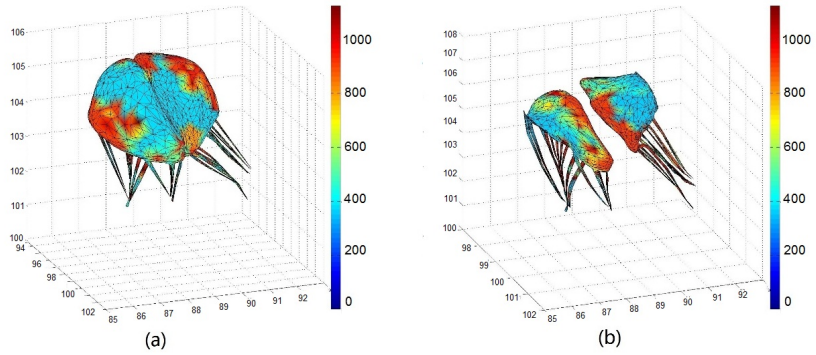

Fig. 4. Pressures distributed on mitral valve calculated by fluid structure interaction under closure situation of normal MV and mitral insufficiency respectively. Initial blood density ρ_0 is 1050 $kg/m3$, yield stress τ_y is 0.04 $dynes/cm^2$.

After that, we evaluate the function of post-operative mitral valve by our method. We compute the stress distributions of normal and pathological mitral

valve in the closure state. Figure 4(a) and Figure 4(b) demonstrate the pressures distributed on MV under closure situation of normal MV and mitral insufficiency respectively, where color bar represents pressures. For patients with MV disease, defects in leaflet morphology can lead to abnormal mitral valve closure, resulting in mitral regurgitation that blood flows back towards the left atrium. In Figure 4, there are transvalvular pressures distributing over the corresponding atrial and ventricular sides of the leaflet structure, which is an important clinical feature for diagnosing mitral insufficiency that usually has lower transvalvular pressures.

However, there are some limitations for our method. The mitral valve in this work is modeled as linear elastic material, which can not well describe the anisotropic and nonlinear characteristics of mitral valve tissue. Besides, the boundary condition of our model only considers chordae tendineae, while mitral valve annulus plays an important role in mitral valve motion. In addition, during fluid structure interaction, the myocardium has been assumed to be rigid, while it will be more accurate to evaluate the transvalvular pressures if the myocardium is modelled as elastomer and starts to contract in systole phase.

6 Conclusion

In this paper, we presented a practical computational framework of fast fluid-structure interaction between blood flow and mechanical mitral valve. Embedded deformable model was adopted to achieve the real time structural dynamics of MV, which can now yield clinically relevant insights into valvular morphology and function. Besides, SPH based FSI method can model the post-operative hemodynamic loading across the valves. Experimental results demonstrate that our method can achieve real-time simulation of mitral valve dynamics without interpenetration of two deformable leaflets, as well as provides post-operative evaluation for MV repair strategies.

In future work, to ensure clinically relevant and useful of our method, the advances in computational modeling should proceed in tandem with carefully designed in vitro and in vivo experiments to yield data for validating the computational models. We will model MV as anisotropic and nonlinear tissue by introducing the material property in MR elastography, acquire the boundary condition from in-vivo patient-specific three-dimensional cardiac MR or echocardiography and extract three-dimensional MV models in time series to establish a more accurate data-driven deformable model [22]. We will also compare our results with COMSOL Multiphysics, which is a multipurpose software platform for simulating physics-based problems, to validate the FSI analysis results.

Acknowledgments The work is supported by grants from Gongdong Natural Science Foundation Project (No. 2016A030313047), Shenzhen Science and Technology Program (No.JCYJ20160429190300857), the Science and Technology Plan Project of Guangzhou (No.201704020141) and National Natural Science Foundation of China (No. 81601576).

References

[1] B. Iung and A. Vahanian, “Epidemiology of valvular heart disease in the adult,” Nature Reviews Cardiology, vol. 8, no. 3, pp. 162–172, 2011.
[2] A. Vahanian, H. Baumgartner, J. Bax, E. Butchart, R. Dion, G. Filippatos, F. Flachskampf, R. Hall, B. Iung, J. Kasprzak et al., “Guidelines on the management of valvular heart disease,” European heart journal, vol. 28, no. 2, pp. 230–268, 2007.
[3] J. S. Gammie, S. M. OBrien, B. P. Griffith, T. B. Ferguson, and E. D. Peterson, “Influence of hospital procedural volume on care process and mortality for patients undergoing elective surgery for mitral regurgitation,” Circulation, vol. 115, no. 7, pp. 881–887, 2007.
[4] T. Mansi, I. Voigt, B. Georgescu, X. Zheng, E. A. Mengue, M. Hackl, R. I. Ionasec, T. Noack, J. Seeburger, and D. Comaniciu, “An integrated framework for finite-element modeling of mitral valve biomechanics from medical images: application to mitralclip intervention planning,” Medical image analysis, vol. 16, no. 7, pp. 1330–1346, 2012.
[5] K. Kunzelman, D. R. Einstein, and R. Cochran, “Fluid–structure interaction models of the mitral valve: function in normal and pathological states,” Philosophical Transactions of the Royal Society of London B: Biological Sciences, vol. 362, no. 1484, pp. 1393–1406, 2007.
[6] E. Votta, T. B. Le, M. Stevanella, L. Fusini, E. G. Caiani, A. Redaelli, and F. Sotiropoulos, “Toward patient-specific simulations of cardiac valves: state-of-the-art and future directions,” Journal of biomechanics, vol. 46, no. 2, pp. 217–228, 2013.
[7] M. Stevanella, F. Maffessanti, C. A. Conti, E. Votta, A. Arnoldi, M. Lombardi, O. Parodi, E. G. Caiani, and A. Redaelli, “Mitral valve patient-specific finite element modeling from cardiac mri: application to an annuloplasty procedure,” Cardiovascular Engineering and Technology, vol. 2, no. 2, pp. 66–76, 2011.
[8] C. Xu, A. S. Jassar, D. P. Nathan, T. J. Eperjesi, C. J. Brinster, M. M. Levack, M. Vergnat, R. C. Gorman, J. H. Gorman, and B. M. Jackson, “Augmented mitral valve leaflet area decreases leaflet stress: a finite element simulation,” The Annals of thoracic surgery, vol. 93, no. 4, pp. 1141–1145, 2012.
[9] P. E. Hammer, J. Pedro, and R. D. Howe, “Anisotropic mass-spring method accurately simulates mitral valve closure from image-based models,” in Functional Imaging and Modeling of the Heart. Springer, 2011, pp. 233–240.
[10] P. E. Hammer, M. S. Sacks, J. Pedro, and R. D. Howe, “Mass spring model for simulation of heart valve tissue mechanical behavior,” Annals of biomedical engineering, vol. 39, no. 6, pp. 1668–1679, 2011.
[11] P. E. Hammer, P. C. Chen, J. Pedro, and R. D. Howe, “Computational model of aortic valve surgical repair using grafted pericardium,” Journal of biomechanics, vol. 45, no. 7, pp. 1199–1204, 2012.
[12] B. E. Griffith, “Immersed boundary model of aortic heart valve dynamics with physiological driving and loading conditions,” International Journal for Numerical Methods in Biomedical Engineering, vol. 28, no. 3, pp. 317–345, 2012.
[13] T. B. Le and F. Sotiropoulos, “Fluid–structure interaction of an aortic heart valve prosthesis driven by an animated anatomic left ventricle,” Journal of computational physics, vol. 244, pp. 41–62, 2013.
[14] Einstein D R, Pin F D, Jiao X, et al. Fluid-Structure Interactions of the Mitral Valve and Left Heart: Comprehensive Strategies, Past, Present and Future.[J]. International Journal for Numerical Methods in Biomedical Engineering, 2010, 26(3-4):348-380.
[15] Lau K D, Diaz V, Scambler P, et al. Mitral valve dynamics in structural and fluid–structure interaction models[J]. Medical Engineering & Physics, 2010, 32(9):1057-1064.
[16] Mittal R, Seo J H, Vedula V, et al. Computational modeling of cardiac hemodynamics: Current status and future outlook[J]. Journal of Computational Physics, 2016, 305:1065-1082.

[17] Otani T, Alissa A, Pourmorteza A, et al. A Computational Framework for Personalized Blood Flow Analysis in the Human Left Atrium.[J]. Annals of Biomedical Engineering, 2016:1-11.
[18] K. Miller, G. Joldes, D. Lance, and A. Wittek, "Total lagrangian explicit dynamics finite element algorithm for computing soft tissue deformation," Communications in numerical methods in engineering, vol. 23, no. 2, pp. 121–134, 2007.
[19] J. J. Monaghan, "Smoothed particle hydrodynamics," Reports on progress in physics, vol. 68, no. 8, p. 1703, 2005.
[20] M. Nesme, P. G. Kry, L. Jerabkova, et al , "Preserving topology and elasticity for embedded deformable models," ACM Transactions on Graphics (TOG), vol. 28, no. 3. ACM, 2009, p. 52.
[21] C. S. Peskin, "The immersed boundary method," Acta numerica, vol. 11, pp. 479–517, 2002.
[22] Su B, San Tan R, Le Tan J, et al. Cardiac MRI based numerical modeling of left ventricular fluid dynamics with mitral valve incorporated[J]. Journal of biomechanics, 2016, 49(7): 1199-1205.
[23] Tim Poston, Tien Tsin Wong, and Pheng Ann Heng. 1998. Multiresolution Isosurface Extraction with Adaptive Skeleton Climbing. Computer Graphics Forum 17, 3 (1998), 137–147. https://doi.org/10.1111/1467-8659.00261
[24] Tao Ju, Scott Schaefer, and Joe Warren. 2005. Mean value coordinates for closed triangular meshes. In ACM Transactions on Graphics (TOG), Vol. 24. ACM, 561–566.

Maximum Principal AAA Wall Stress is Proportional to Wall Thickness

K. Miller[1], G. R. Joldes[1,2], J. Qian[1], A.P. Patel[1], M.S. Jung[1], A.C.R. Tavner[1], A. Wittek[1]

[1]Intelligent Systems for Medicine Laboratory, The University of Western Australia, Crawley, Western Australia, 6009

[2]School of Engineering and Information Technology, Murdoch University, 90 South St, Murdoch, Western Australia 6150

Abstract

Abdominal aortic aneurysm (AAA) is a permanent and irreversible dilation of the lower region of the aorta. It is an asymptomatic condition which if left untreated can expand to the point of rupture. Rupture of an artery will occur when the local wall stress exceeds the local wall strength. Therefore, estimation of a patient's AAA wall stress non-invasively, quickly and reliably is desirable. One solution to this problem is to use recently-published methods to compute AAA wall stress, using geometry from CT scans, and median arterial pressure as the load. Our method is embedded in the software platform BioPARR - Biomechanics based Prediction of Aneurysm Rupture Risk, freely available from http://bioparr.mech.uwa.edu.au/. Experience with over fifty patient-specific stress analyses, as well as common sense, suggests that the AAA wall stress is critically dependent on the local AAA wall thickness. This thickness is currently very difficult to measure in the clinical environment. Therefore, we conducted a simulation study to elucidate the relationship between the wall thickness and the maximum principal stress. The results of the analysis of three cases presented here unequivocally demonstrate that this relationship is approximately linear, bringing us closer to being able to compute predictive stress envelopes for every patient.

Keywords: Abdominal Aortic Aneurysm; Patient-Specific Modelling; Finite Element Method; Stress; Wall Thickness

Introduction

Abdominal aortic aneurysm (AAA) is a permanent and irreversible dilation of the lower region of the aorta. Typically, it is an asymptomatic condition that if left untreated, can result in rupture of the aorta. AAA diagnosis has tripled over the last thirty years and is likely to continue increasing [1]. AAA is found in approximately 7% of elderly men (>65 years) in Australia [2] with similar prevalence in the Western world [3]. This equates to about 114,000 Australian men currently living with AAA. As another example, GBE-Bund statistics show that in 2014 the number of hospitalized AAA patients in Germany was about 85400. The disease also affects women, but to a lesser extent.

Because AAA is typically asymptomatic, most people are unaware of their condition. However, AAA rupture is a catastrophic clinical event with mortality rates of approximately 80-90% [4-6]. Currently, the most evidence-based indicator of rupture threat is the maximum anterior-posterior diameter. Diameters >5.5cm are deemed high risk. However 20% of smaller AAAs rupture, and larger cases often remain quiescent [7, 8]. Surgical repairs of AAAs are expensive. They cost the Australian health system approximately $230m per year and as many as 75% of these operations may be unnecessary. The ability to predict, non-invasively, which cases are at risk of rupture will have a major clinical impact by saving lives and reducing medical costs worldwide.

There are many limitations to the current clinical definition of 'high-risk', and many researchers believe that patient-specific modelling (PSM) has major clinical potential [9-14]. Mechanically-speaking, rupture of an artery will occur when the local wall stress exceeds the local wall strength. With advances in medical imaging technology and medical image analysis software, it is now possible to create patient-specific reconstructions of the AAA, which are then used for computer simulations aimed at computing the wall stress. Such simulations have steadily increased in complexity [11, 15-17]. Significant research effort has been devoted to material models and simulations of such complexity that their implementation would require computer power and specialist knowledge which is simply not available in a typical clinic.

Recently an entirely new, very simple approach to compute AAA wall stress was proposed and validated [13] (see also [14, 18]). The inputs to the model are the (loaded) geometry of an aneurysm (obtained from a CT reconstruction), wall thickness and blood pressure. By treating the aneurysm as if it were in static equilibrium, forces caused by the internal pressure must be balanced by the forces in the AAA wall; hence the stresses in the wall can be calculated based on the wall thickness. This method is embedded in the recently-developed and freely-available software platform

BioPARR - Biomechanics based Prediction of Aneurysm Rupture Risk, available from (http://bioparr.mech.uwa.edu.au/). What is truly exciting about this simple approach is that information about arterial tissue material parameters is not required; this supports the development and use of PSM, where previously [19] uncertainty in material properties has been recognized as a key limitation. Moreover the computation itself is so simple that many repeated simulations for a single patient are feasible, enabling stochastic extension of the models [20].

The accuracy, predictive power and ultimately the clinical utility of this simple and efficient method to compute AAA wall stress is critically dependent on the estimation of the AAA wall thickness. At present, all patient-specific computational biomechanics studies in the field of vascular biomechanics assume homogeneous and constant wall thickness. However Zhu et al. [21] recently demonstrated a novel MR imaging technique that may lead to more accurate measurement of thickness. In [13] we undertook one of the first attempts to measure AAA wall thickness using a CT-MRI fusion. Starting from this imperfect measurement of wall thickness, we can now evaluate the relationship between the AAA wall thickness and the maximum principal stress.

Methods

Complete stress analyses of AAAs were conducted using our software BioPARR. Excluding the 3D reconstruction time, the entire analysis of a single load case scenario took approx. 6 minutes on an Intel(R) Core(TM) i7-5930K CPU @ 3.50GHz with 64GB of RAM running Windows 8 OS. The analysis steps are briefly described below.

Problem Geometry

We used three real-world, patient-specific 3D geometries, sourced from the initial phase of the MA3RS study [22], with all the irregularities that can be expected in clinical simulations, Figure 1.

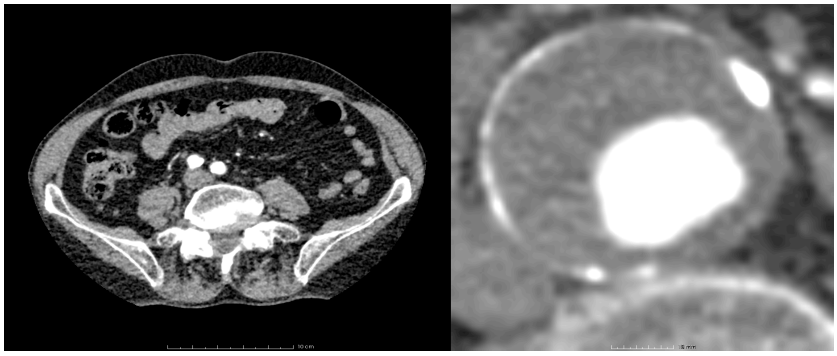

Fig. 1. An example AAA case considered in this study. a) CT image; b) Region of interest, showing the lumen and portions of the AAA wall in white and intraluminal thrombus (ILT) in gray.

Our software system BioPARR allows the analyst to extract and combine data from images from different sources (such as CT and MRI), by implementing a segmentation-based inter-modality image registration algorithm in 3D Slicer [23], as shown in Figure 2. The analyst has control over many parameters influencing the analysis results: the thickness of the AAA wall; inclusion of thrombus; geometry meshing; finite element type selection; and finite element simulation scenarios. The software can be used in the case when both CT and MRI data are available for a patient or, more typically, when only CT is available. The program automatically generates 3D color-contoured visualizations of the key patient-specific components of the analysis, the ILT thickness and the normalized ratio of the maximum AAA diameter and the diameter in the proximal neck of the aneurysm (NORD).

Image Segmentation

The high variability in AAA geometry, as well as the difficulty in discriminating between the AAA and the surrounding tissue in parts of the image, make automatic AAA segmentation practically impossible. Therefore our software uses segmentation tools available in the free, open source image analysis software 3D Slicer [24]. We have found that using the 3D Slicer extension FastGrowCut for segmentation [25] can help reduce the segmentation time. Manual intervention is still required to define the region of interest in the image, cropping, defining the seeds for the FastGrowCut algorithm; and performing corrections and smoothing of the resulting label

maps. Using this method, we can extract the AAA geometry from CT or MRI.

Wall thickness measurement and specification

Although wall thickness has a great influence on the stress distribution within the AAA wall [26], accurate extraction from medical images remains problematic due to the low image resolution and the difficulty of distinguishing the AAA wall from parts of the surrounding tissue, because of similar intensities in the image. This uncertainty is why many authors have used constant wall thickness in their analyses. BioPARR allows the user to specify wall thickness at multiple points on the AAA surface. These discrete thickness measurements are then converted to a smooth model of the aneurysm wall through interpolation.

The uncertainty in the patient-specific AAA wall thickness will propagate through the computational model and result in uncertainty in the computed stress. Therefore, for each case considered we conducted repeated manual measurements of wall thickness in three cross-sections, where the image contrast was best and reasonable accuracy could be obtained, Figures 2 and 3.

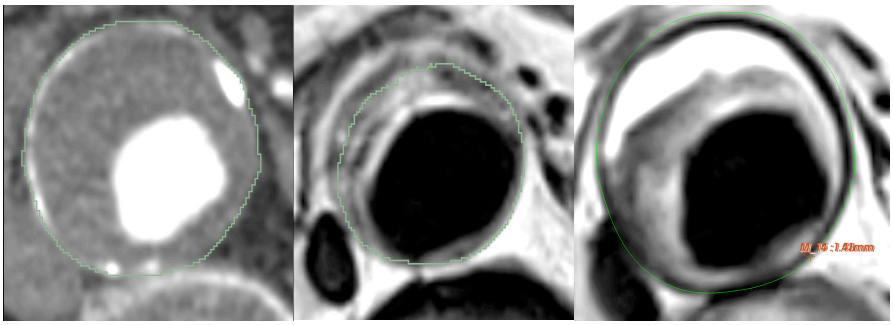

Fig. 2. MRI to CT registration. Axial view of AAA label map (green contour) segmented from CT (left); Axial view of AAA label map segmented from MRI (centre); CT label map over MRI image demonstrated the quality of MRI to CT registration (right).

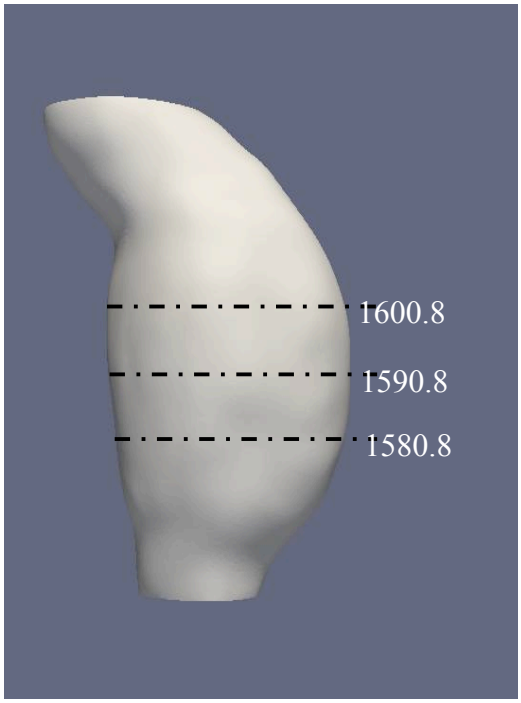

Fig. 3. Cross-sections at which repeated measurements of AAA wall thickness were conducted. Five measurements were taken at two points in each cross-section using the MRI image registered to CT

Estimated variable wall thickness for Case 1 is given in Fig. 4. It is clear that the wall thickness may vary locally from as little as 1.4 mm to about 2.1 mm.

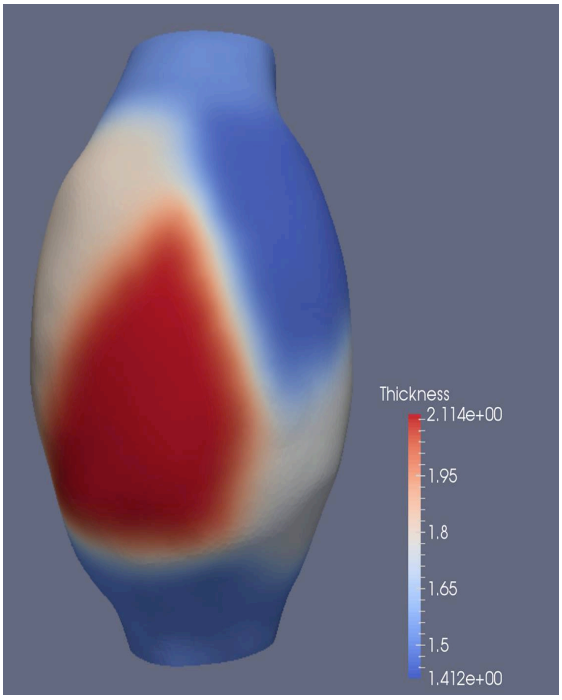

Fig. 4. AAA Geometry (Case 1) generated using varying thickness. Measured thickness varies between 1.4 mm and 2.11 mm for this case.

Geometry creation

The label maps segmented from images, along with the wall thickness information, are used to create the AAA geometry. The external AAA wall surface, the internal AAA wall surface and the internal intraluminal thrombus (ILT) surface are automatically created.

Finite Element Meshing, Model Creation and Analysis

Meshing of the AAA wall and ILT, based on external and internal AAA wall surfaces and the internal ILT surface, is performed using open source meshing software Gmsh [27, 28] called from within BioPARR. A tetrahedral volumetric mesh is created using the element size specified by the user. This process ensures a conforming mesh between the ILT and AAA wall. The meshing approach implemented in BioPARR maintains the geometric accuracy of the meshed surfaces by using very small elements on

these surfaces. At the same time, the element size inside the ILT volume and in the thicker areas of the AAA wall is increased, reducing the overall number of elements in the mesh and hence the computational cost of the finite element analysis.

The element types can be configured as linear or quadratic, displacement only or hybrid displacement-pressure formulation. Finally, Abaqus [29] input (.inp) files are generated and sent for finite element analysis. Figure 6 shows a typical AAA mesh. In the results presented here, we used quadratic tetrahedral elements and a hybrid formulation. The ILT thickness was included in the model and given a typical stiffness of 5% of the stiffness of the AAA wall. [13]

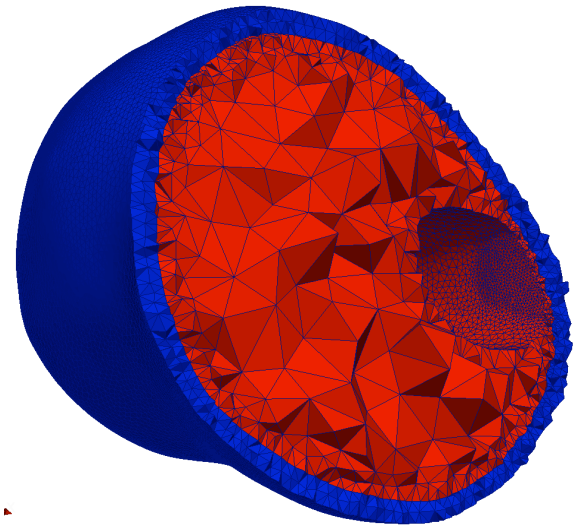

Fig 5. Example of meshing. The AAA wall is meshed using 2 layers of elements (configurable). The ILT is meshed using a minimum of 2 layers of elements (configurable); the element size is increased in the middle of the ILT layer to reduce the number of elements in the mesh.

The finite element simulations are carried out using the procedure described in [13], which allows the computation of stress in the AAA wall without exact knowledge of the material properties. This is of great practical significance, as patient-specific material properties for the AAA wall and ILT are currently impossible to obtain *in vivo*. For a detailed discussion of the problem of obtaining solutions without knowing mechanical properties of tissues see also [19, 30]. The results of finite element simulations (maximum principal stresses in the AAA wall) are extracted by BioPARR for visualization and analysis.

Results

For each case considered we conducted five thickness measurements at six points on the AAA wall. The measurements were then ranked from the smallest to the largest. We then created five geometries (as explained in the Methods section) using measured thicknesses with the same rank. This allowed us to create five finite element models, ranked by average wall thickness, for each of the three cases considered in this study.

We chose to use maximum principal stress as a scalar indicator of the internal forces being withstood by the wall tissue. Typical results are shown in Figure 6.

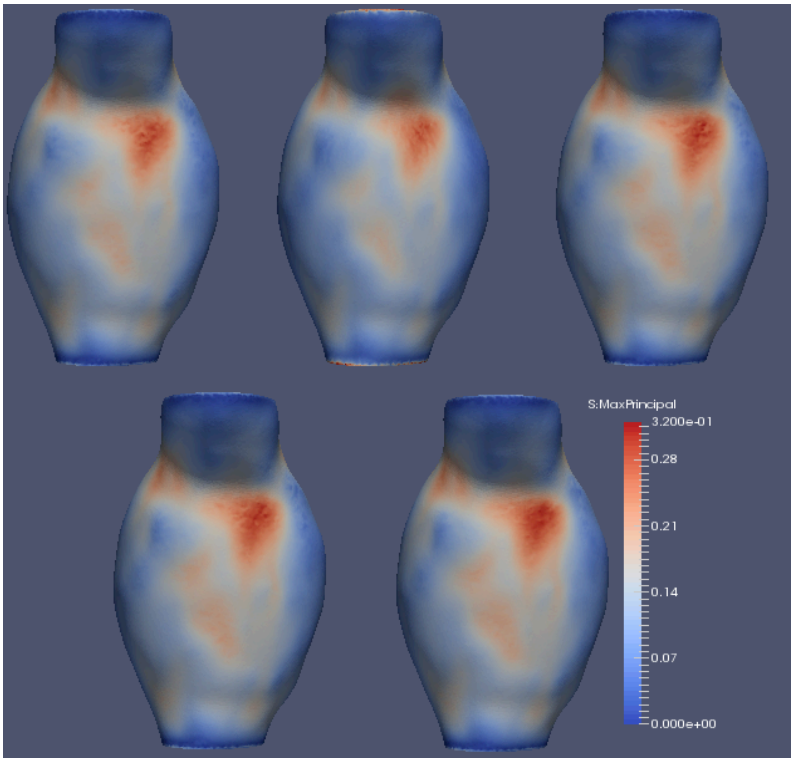

Fig. 6. Maximum principal stress (98 percentile) for Case 1. From the thickest (top left), to the thinnest wall (bottom right)

Figure 7 shows the relationship between the maximum principal wall stress and the average wall thickness. It is clear that this relationship, for every case considered, is approximately linear.

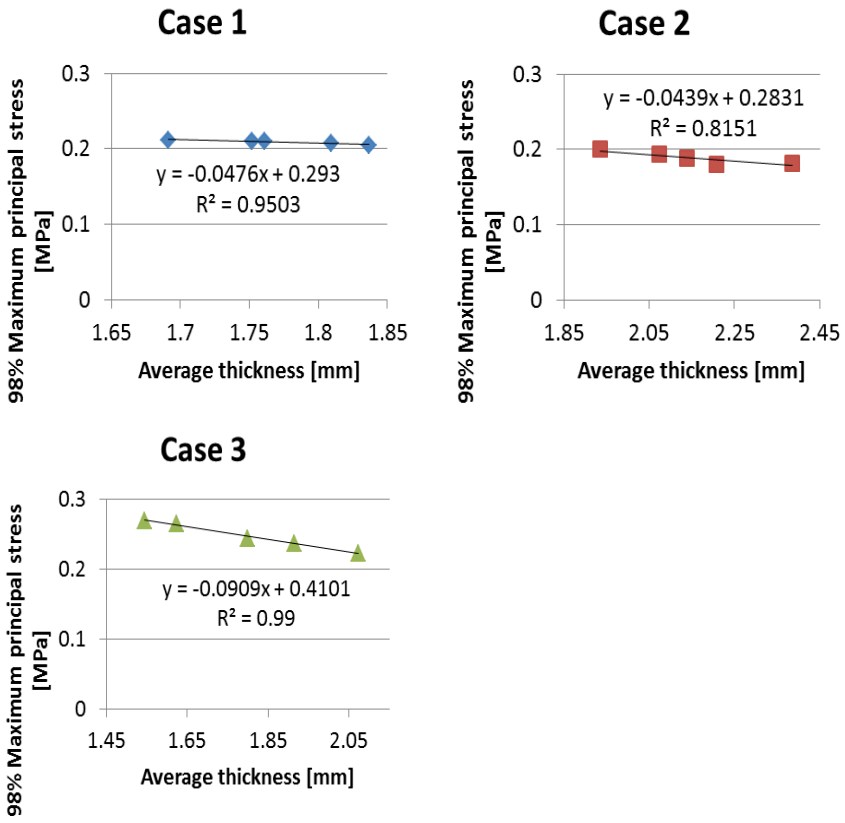

Fig. 7. Relationship between the average AAA wall thickness and maximum principal stress (98 percentile) for the analyzed cases.

Discussion and Conclusions

We used our software BioPARR to analyse the relationship between the difficult to measure AAA wall thickness and the wall stress. Our results indicate that this relationship is approximately linear. The simplicity of this relationship allows a certain level of optimism about the possibility of confidently constructing predictive stress envelopes for individual AAA patients.

The results presented in this paper are not entirely surprising. Standard engineering equations for stress in cylindrical pressure vessels exhibit linearity between vessel wall thickness and maximum stress. Furthermore, the following simple dimensional reasoning[1] suggests that our results, even

[1] We are indebted to Dr. Johann Drexl from Fraunhofer MEVIS for his comments on the results.

though computed for complicated geometries, are not entirely unexpected. Blood pressure acts on the internal surface of an aneurysm with an area proportional to the square of the AAA radius. Internal forces (stresses), balancing the pressure load, act on the cross-section of the AAA wall which is proportional to the radius multiplied by the wall thickness. Therefore the linear variation of stress with the wall thickness should not be entirely unexpected. The results presented here are in agreement with our suggestion from over ten years ago that in biomechanics often seemingly complicated relationships conceal an approximately linear dependence [31].

Acknowledgments

The financial support of the National Health and Medical Research Council (Grant No. APP1063986) is gratefully acknowledged. We wish to acknowledge the Raine Medical Research Foundation for funding G. R. Joldes through a Raine Priming Grant, and the Department of Health, Western Australia, for funding G. R. Joldes through a Merit Award. The AAA data has been obtained from the MA3RS study [22].

References

1. Bosch, J.L., et al., Abdominal Aortic Aneurysms: Cost-effectiveness of Elective Endovascular and Open Surgical Repair. Radiology, 2002. **225**(2): p. 337-344.
2. Norman, P.E., et al., *Population based randomised controlled trial on impact of screening on mortality from abdominal aortic aneurysm.* BMJ, 2004. **329**(7477): p. 1259.
3. Singh, K., et al., *Prevalence of and Risk Factors for Abdominal Aortic Aneurysms in a Population-based Study: The Tromsø Study.* American Journal of Epidemiology, 2001. **154**(3): p. 236-244.
4. Bengtsson, H. and D. Bergqvist, *Ruptured abdominal aortic aneurysm: A population-based study.* Journal of Vascular Surgery, 1993. **18**(1): p. 74-80.
5. Kantonen, I., et al., *Mortality in Ruptured Abdominal Aortic Aneurysms.* European Journal of Vascular and Endovascular Surgery, 1999. **17**(3): p. 208-212.
6. Evans, S.M., D.J. Adam, and A.W. Bradbury, *The influence of gender on outcome after ruptured abdominal aortic aneurysm.* Journal of Vascular Surgery, 2000. **32**(2): p. 258-262.
7. Darling, R.C., et al., *Autopsy study of unoperated abdominal aortic aneurysms. The case for early resection.* Circulation, 1977. **56**: p. 161-164.
8. Greenhalgh, R.M., *Comparison of endovascular aneurysm repair with open repair in patients with abdominal aortic aneurysm (EVAR trial 1), 30-day operative mortality results: randomised controlled trial.* The Lancet, 2004. **364**(9437): p. 843-848.
9. McGloughlin, T.M. and B.J. Doyle, *New Approaches to Abdominal Aortic Aneurysm Rupture Risk Assessment: Engineering Insights With Clinical Gain.* Arteriosclerosis, Thrombosis, and Vascular Biology, 2010. **30**(9): p. 1687-1694.
10. Vande Geest, J.P., et al., *A biomechanics-based rupture potential index for abdominal aortic aneurysm risk assessment: demonstrative application.* Annals of the New York Academy of Sciences, 2006. **1085**: p. 11-21.
11. Gasser, T.C., et al., *Biomechanical rupture risk assessment of abdominal aortic aneurysms:*

model complexity versus predictability of finite element simulations. European Journal of Vascular and Endovascular Surgery, 2010. **40**(2): p. 176-85.
12. Gasser, T.C., et al., *A novel strategy to translate the biomechanical rupture risk of abdominal aortic aneurysms to their equivalent diameter risk: method and retrospective validation.* Eur J Vasc Endovasc Surg, 2014. **47**(3): p. 288-95.
13. Joldes, G.R., et al., *A simple, effective and clinically applicable method to compute abdominal aortic aneurysm wall stress.* Journal of the mechanical behavior of biomedical materials, 2016. **58**: p. 139-148.
14. Zelaya, J.E., et al., *Improving the Efficiency of Abdominal Aortic Aneurysm Wall Stress Computations.* PLoS ONE, 2014. **9**(7): p. e101353.
15. Raghavan, M., et al., *Wall stress distribution on three-dimensionally reconstructed models of human abdominal aortic aneurysm.* J Vasc Surg, 2000. **31**: p. 760 - 769.
16. Doyle, B., A. Callanan, and T. McGloughlin, *A comparison of modelling techniques for computing wall stress in abdominal aortic aneurysms.* Biomed Eng Online, 2007. **6**(1): p. 38.
17. Li, Z.Y., et al., *Association between aneurysm shoulder stress and abdominal aortic aneurysm expansion: a longitudinal follow-up study.* Circulation, 2010. **122**(18): p. 1815-22.
18. Fung, Y.C., *What Are the Residual Stresses Doing in Our Blood Vesssels?* Annals of Biomedical Engineering, 1991. **19**: p. 237-249.
19. Miller, K. and J. Lu, *On the prospect of patient-specific biomechanics without patient-specific properties of tissues.* Journal of the Mechanical Behavior of Biomedical Materials, 2013. **27**: p. 154–166.
20. Calvetti, D., J.P. Kaipio, and E. Somersalo, *Inverse problems in the Bayesian framework.* Inverse Problems, 2014. **30**(11): p. 110301.
21. Zhu, C., et al., *Isotropic 3D black blood MRI of abdominal aortic aneurysm wall and intraluminal thrombus.* Magnetic Resonance Imaging, 2016. **34**(1): p. 18-25.
22. McBride, O.M.B., et al., *MRI using ultrasmall superparamagnetic particles of iron oxide in patients under surveillance for abdominal aortic aneurysms to predict rupture or surgical repair: MRI for abdominal aortic aneurysms to predict rupture or surgery—the MA3RS study.* Open Heart, 2015. **2**(1).
23. Fedorov, A., et al., *3D Slicer as an image computing platform for the Quantitative Imaging Network.* Magnetic Resonance Imaging, 2012. **30**(9): p. 1323–1341.
24. Fedorov, A., et al., *3D Slicer as an image computing platform for the Quantitative Imaging Network.* Magnetic Resonance Imaging, 2012. **30**(9): p. 1323-1341.
25. Zhu, L., et al., *An Effective Interactive Medical Image Segmentation Method Using Fast GrowCut*, in *International Conference on Medical Image Computing and Computer Assisted Intervention (MICCAI), Interactive Medical Image Computing Workshop*2014: Boston, USA.
26. Joldes, G.R., et al., *A simple, effective and clinically applicable method to compute abdominal aortic aneurysm wall stress.* Journal of the Mechanical Behavior of Biomedical Materials, 2015: p. DOI: 10.1016/j.jmbbm.2015.07.029.
27. Geuzaine, C. and J.-F. Remacle. *Gmsh - A three-dimensional finite element mesh generator with built-in pre- and post-processing facilities*. 2016 03 March 2016]; Available from: http://gmsh.info/.
28. Geuzaine, C. and J.-F. Remacle, *Gmsh: a three-dimensional finite element mesh generator with built-in pre- and post-processing facilities.* International Journal for Numerical Methods in Engineering, 2009. **79**(11): p. 1309-1331.
29. ABAQUS, *ABAQUS Theory Manual Version 6.9*2009, Providence, RI: Dassault Systèmes Simulia Corp.
30. Wittek, A., T. Hawkins, and K. Miller, *On the unimportance of constitutive models in computing brain deformation for image-guided surgery.* Biomechanics and modeling in mechanobiology, 2009. **8**(1): p. 77-84.
31. Taylor, Z. and K. Miller, *Using numerical approximation as an intermediate step in analytical derivations: some observations from biomechanics.* Journal of biomechanics, 2005. **38**(12): p. 2497-2502.

An Immersed Boundary Method for Detail-Preserving Soft Tissue Simulation from Medical Images

Christoph J. Paulus, Roland Maier, Daniel Peterseim, and Stéphane Cotin

Abstract Simulating the deformation of the human anatomy is a central element of Medical Image Computing and Computer Assisted Interventions. Such simulations play a key role in non-rigid registration, augmented reality, and several other applications. Although the Finite Element Method is widely used as a numerical approach in this area, it is often hindered by the need for an optimal meshing of the domain of interest. The derivation of meshes from imaging modalities such as CT or MRI can be cumbersome and time-consuming. In this paper we use the Immersed Boundary Method (IBM) to bridge the gap between these imaging modalities and the fast simulation of soft tissue deformation on complex shapes represented by a surface mesh directly retrieved from binary images. A high resolution surface, that can be obtained from binary images using a marching cubes approach, is embedded into a hexahedral simulation grid. The details of the surface mesh are properly taken into account in the hexahedral mesh by adapting the Mirtich integration method. In addition to not requiring a dedicated meshing approach, our method results in higher accuracy for less degrees of freedom when compared to other element types. Examples on brain deformation demonstrate the potential of our method.

Key words: Computational anatomy, medical imaging, computer assisted interventions, Finite Element modeling, Immersed Boundary Method

---

Christoph J. Paulus
Inria Nancy Grand Est, France and Université de Strasbourg, ICube Lab, CNRS, Illkirch, France

Roland Maier
Inria Nancy Grand Est, France and University of Augsburg

Daniel Peterseim
University of Augsburg, supported by DFG-SPP 1748 under the project *Adaptive isogeometric modeling of discontinuities in complex-shaped heterogeneous solids*

Stéphane Cotin
Inria Nancy Grand Est, France and Université de Strasbourg, ICube Lab, CNRS, Illkirch, France

1 Introduction

Computational models in the field of Medical Image Computing and Computer Assisted Interventions play an increasingly important role, in areas such as non-rigid registration, augmented reality, or surgical training. In this context, the Finite Element Method (FEM) is often used as the reference numerical approach, and many works have addressed its computational efficiency and accuracy [3, 10, 15].

An alternative approach are mesh-free methods that can be applied likewise, but need a separate surface representation and hence dealing with boundary conditions can become cumbersome. Additionally, mesh-free methods use integration methods which need a volumetric grid and can be computationally expensive. Thus, mesh-free methods are less appealing for our purposes and this work is based on the FEM.

To construct a Finite Element mesh, the general procedure consists of the following steps: the pre-operative image is segmented, then a surface mesh is built as the isosurface of the segmented image, and finally a volumetric mesh is constructed in the domain enclosed by the boundary surface. At this stage, the geometrical complexity of anatomical structures make the generation of volume meshes from a given surface representation a very challenging task.

Volumetric meshing of the domain is almost always done with linear tetrahedral elements and remains a very active area of research [13, 8]. While simulations with tetrahedral elements may lead to numerical issues, such as volumetric locking [1], hexahedral elements suffer less from volumetric locking and yield an equivalent or higher accuracy per degree of freedom. However, hexahedral meshes can hardly be adapted to complex surfaces [7]. Thus, it is advantageous to either extend the partial differential equation (PDE) outside the actual domain in order to use a domain-independent mesh, which is known as the Finite Cell Method [14], or to work with partially filled elements. In the following, we will focus on the latter approach. The Composite FEM [6, 18, 19], for instance, simulates deformations with a coarse hexahedral grid efficiently, while a fine grid is used to modify the shape functions in such a way that they match the boundary conditions to a given accuracy. The fine grid is also utilized for the numerical integration. Tuning the resolution of the coarse grid increases the accuracy of deformations, while the resolution of the fine grid controls the geometric proximity at the beginning of the simulation. Other popular approaches also require two meshes. For example, the Cut Finite Element Method [2] operates on coarse elements but requires a sub-mesh in order to integrate basis functions over the actual domain. The method proposed in [9] is based on two overlapping Finite Element meshes, a coarse mesh that does not resolve any domain boundaries and one that resolves the boundary. The method is then based on the coarse Finite Element functions enriched by the Finite Element functions of the resolving mesh. Boundary conditions are enforced in integral form with Nitsche's method. The key challenge is to integrate over the cut elements at the boundary and the boundary segments, where an efficient integration method proposed by Mirtich [11] is used. The additional Finite Element functions ensure the accuracy at the boundary but also increase the number of degrees of freedom.

In this paper we present a Finite Element approach derived from the Immersed Boundary Method (IBM), which was first introduced by Peskin [16] to simulate blood flows: A potentially high resolution surface mesh is immersed into a coarse simulation mesh. We solve partial differential equations with a regular hexahedral mesh that can automatically be built from the bounding box of a segmented image. To precompute the system matrices, such as the stiffness, the damping and the mass matrix, our method uses the extension of an integration method dealing with arbitrary polygons [11] and thus with arbitrary geometrical shapes. The efficiency of this integration method yields a fast initialization of our algorithm while the speed depends upon the resolution of the objects surface.

Our approach is very similar to the one presented in [9]. Both methods use Nitsche's method to apply boundary conditions and Mirtich's integration method to integrate over boundary elements. The key advantage of our method, however, is that we do not need a second volumetric mesh to resolve the boundary and only use the basis functions of the coarse volumetric mesh. While this difference results in less accuracy at the boundary itself, the information gathered from the exact integration is enough to efficiently simulate the coarse behavior of an object. The fewer degrees of freedom are particularly appealing since we aim for dynamic simulations in real time. Other methods, such as [9] that resolve the boundary are less suitable for dynamic simulations because of the higher number of degrees of freedom which results in larger linear systems to be solved in every time step. The main difference compared to the Composite FEM or the Cut FEM lies in the fact that no additional refined mesh is needed to resolve complicated structures. Moreover, those methods are mainly based on distance functions to characterize the boundary and not on a surface mesh.

To further increase the speed of the dynamic simulation, we enrich the IBM with the corotational approach, preventing recomputations of the system matrices and thus allowing for real-time computation. The stability of our approach is ensured by the removal of elements that are only filled with a small portion of the complete cube. Evaluations reveal the improved accuracy per degree of freedom of our approach when comparing to the conventional methods, particularly for objects with complex geometries. Thus, our method has an improved efficiency which decreases computational costs. Since the meshing with different resolutions is not an issue, it can be adapted to the power of the device performing the computation. This underlines the importance for the simulation of surgical interventions.

Our paper is structured as follows: After a brief overview of the Immersed Boundary Method from which we derived our approach, section 2 explains the core of the method. Then we present a numerical comparison against other techniques in section 3.1. Finally, we apply our method on a complex brain geometry to simulate a brain shift (section 3.2), and conclude in section 4 discussing future extensions.

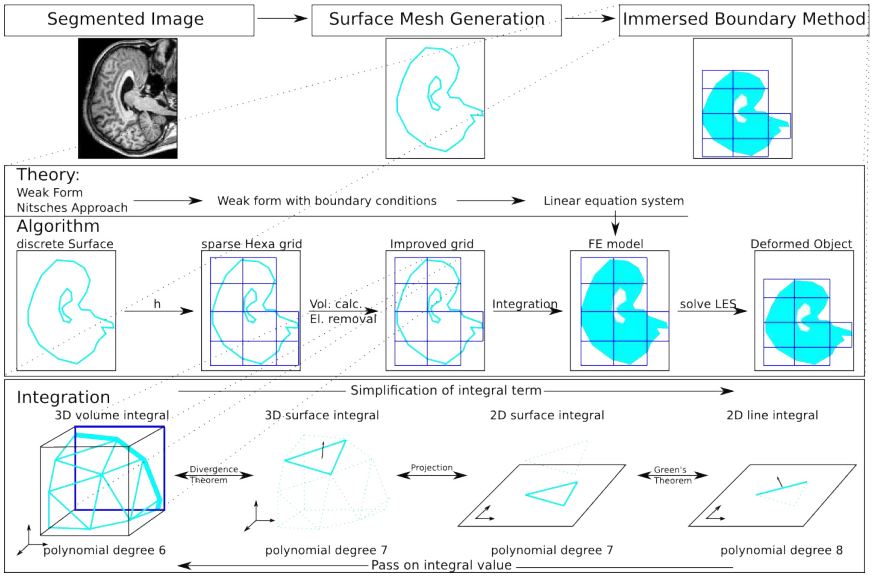

Fig. 1 Overview of our method: general work flow *(top)* and the particular elements of our method *(middle)* with focus on one of the main contributions: the integration

2 Method

This section explains an Immersed Boundary Method (IBM) [17, 20] for dynamic simulations, which has been adapted using an extension of an efficient integration method [11]. This approach allows to embed a discrete representation of complex, high detailed surfaces into the hexahedral simulation mesh, that is potentially coarse and sparse. With the corotational approach, the method keeps its computational efficiency over time. Image processing methods can be used to provide the surface representation. Then our approach can transform this representation directly to a fast, accurate, patient-specific biomechanical model. Circumventing cumbersome and time-consuming volume meshing algorithms thus makes our approach a competitive tool for medical simulations.

Figure 1 summarizes our approach, separating the theory (subsection 2.1) from the algorithmic details and the numerical integration method (subsection 2.2).

2.1 From a continuous problem to a discrete formulation

In order to allow for reasonable computation times while providing accurate deformations, we consider the deformation of objects with initial geometry Ω on a macroscopic scale, which is commonly referred to as the continuum approach. We denote the displacement of a point $X \in \Omega$ to the point x by $u(X,\tau) = x(X,\tau) - X$ at a time $\tau \geq 0$. Using Cauchy's stress tensor σ, the gravity g and density ρ of the

considered material, one can state Cauchy's equation of motion for the dynamic scenario as $\mathrm{div}(\sigma(u)) + \rho g = \rho \ddot{u}$. Additionally, we define boundary conditions fixing the displacement at $u = u_0$ on $\Gamma_D \subseteq \partial\Omega$ and the boundary force or traction at $t(u) = \sigma(u)n = t_0$ on $\Gamma_N = \partial\Omega \backslash \Gamma_D$, where n is the outer normal of our domain Ω. The equation of motion is usually transformed to an integral equation, the so-called weak formulation. In contrary to the standard approach, the IBM incorporates the boundary terms, i.e. as well the Dirichlet boundary condition, in this form. Violations of the conditions are penalized by additional integral terms and using the stabilization parameter γ_D. This is referred to as Nitsche approach [12]. Thus, we search a displacement function u that satisfies

$$\begin{aligned} &\int_\Omega \rho \ddot{u} \cdot v \, dV + \int_\Omega \sigma(u) : \varepsilon(v) \, dV - \int_\Omega \rho g \cdot v \, dV \\ &- \int_{\Gamma_N} t_0 \cdot v \, dA - \int_{\Gamma_D} t(u) \cdot v \, dA - \int_{\Gamma_D} u \cdot t(v) \, dA \\ &+ \int_{\Gamma_D} u_0 \cdot t(v) \, dA - \gamma_D \int_{\Gamma_D} (u_0 - u) \cdot v \, dA = 0 \end{aligned} \tag{1}$$

for all test functions v and all times $\tau \geq 0$. The terms in the first row and the first term in the second row relate to Cauchy's equation of motion and the remaining terms are introduced as a result of the Nitsche approach. The linear elasticity theory defines the linear relationship between the Cauchy stress tensor σ and the strain tensor ε. Since the linearized Green-Lagrange strain is non-zero for rigid body motions such as rotations, we use the corotated strain tensor $\varepsilon(u) = S - I$ with the symmetric stretch matrix S, which is obtained from the deformation tensor.

In order to discretize the object, the surface $\partial\Omega$ is replaced by polygons of arbitrary shape representing a closed, manifold surface $\partial\Omega_h$ potentially of high resolution, that can be obtained by a marching cube algorithm or other image processing methods. Likewise, we replace the boundary domains Γ_D, Γ_N by their discrete counterpart $\Gamma_{D,h}, \Gamma_{N,h}$. Then we overlap the object Ω_h enclosed in $\partial\Omega_h$ with a regular grid of hexahedral elements Ω_e s.t. $\Omega_h \subset \bigcup_e \Omega_e$, and call the hexaeder corner nodes P_i. Note, that the standard Finite Element approach requires equality, i.e. $\Omega_h = \bigcup_e \Omega_e$, which is a strong restriction for the choice of the hexahedral elements. We define the mesh size parameter as $h = \max_e(\max_{X_1, X_2 \in \Omega_e} |X_1 - X_2|)$, which indicates the deformation accuracy of the hexahedral mesh and is independent of the resolution of the surface mesh. The element-wise tri-linear shape functions φ_i of the conventional FEM allow to replace the displacement function by its discrete counterpart $u \approx \sum_i \varphi_i u_i$, with the displacements u_i at the node P_i, forming the vector of displacements $\mathbf{u}(\tau)$ that depends on time. With the Galerkin approach, the integral equation transforms to the semi-discrete equation

$$\begin{aligned} &\rho \mathbf{M}\ddot{\mathbf{u}}(\tau) + \mathbf{D}\dot{\mathbf{u}}(\tau) + \mathbf{K}\mathbf{u}(\tau) - \mathbf{B}_D^T \mathbf{u}(\tau) - \mathbf{B}_D \mathbf{u}(\tau) + \gamma_D \mathbf{M}_D \mathbf{u}(\tau) \\ = \;& \mathbf{M}_N \mathbf{t_0} - \mathbf{B}_D \mathbf{u_0} + \rho \mathbf{M}_\Omega \mathbf{g} + \gamma_D \mathbf{M}_D \mathbf{u_0} \end{aligned} \tag{2}$$

where the terms with the matrix $\mathbf{B}_D$ relate to the integral terms in (1) over the Dirichlet boundary Γ_D and are due to the method of Nitsche. The stiffness matrix $\mathbf{K}$ is

constructed similarly to the conventional FEM, but integrals are computed over the actual domain $\Omega_h \neq \bigcup_e \Omega_e$. $\mathbf{K}$ relates to the second term in (1). Similarly, the mass matrices are adapted to the IBM, i.e. $\mathbf{M}_{Y,ij} = \int_Y \varphi_i \varphi_j$ for $Y = \Gamma_{D,h}, \Gamma_{N,h}, \Omega_h$. Note that the term $\mathbf{D}\dot{\mathbf{u}}(\tau)$ in (2) is artificial and does not correspond to any term in (1). However, the introduction of the damping term is reasonable in the context of dynamic simulation, as damping effects occur in dynamic motions. We choose the damping term to be constant and obtain it using the mass and the stiffness matrix. Such a representation is called modal or Rayleigh damping and can be expressed as

$$\mathbf{D} = \alpha\mathbf{M} + \beta\mathbf{K}.$$

In the general case, an experimental verification of the parameters α and β is essential for real applications [21].

Solving this system of linear equations yields the displacements $u_i(\tau)$ for any time $\tau \geq 0$ of the object Ω at the points P_i, which are propagated to the surface $\partial\Omega$ using the tri-linear shape functions and the initial barycentric coordinates of the surface in the hexahedral mesh. Since (2) is still a continuous formulation with respect to time, the next step to obtain a fully discrete model consists in applying a time-stepping scheme with step size $\Delta\tau$. Here, we use the implicit Euler scheme

$$\begin{aligned} \dot{\mathbf{u}}_{\mathbf{n+1}} &= \dot{\mathbf{u}}_{\mathbf{n}} + \Delta\tau\,\ddot{\mathbf{u}}_{\mathbf{n+1}}, \\ \mathbf{u}_{\mathbf{n+1}} &= \mathbf{u}_{\mathbf{n}} + \Delta\tau\,\dot{\mathbf{u}}_{\mathbf{n+1}}. \end{aligned} \tag{3}$$

Inserting the scheme into (2) leads to a system of linear equations that has to be solved in every time step. For better readability, we only state the equation for the $(n+1)^{th}$ time step under the additional assumption $u_0 \equiv 0$.

$$\begin{aligned} &\left(\rho\mathbf{M} + \Delta\tau\mathbf{D} + \Delta\tau^2(\mathbf{K} - \mathbf{B}_D^T - \mathbf{B}_D + \gamma_D\mathbf{M}_D)\right)\,\dot{\mathbf{u}}_{\mathbf{n+1}} \\ &= \Delta\tau\mathbf{f_0} + \left(\rho\mathbf{M} - \Delta\tau\,(\mathbf{K} - \mathbf{B}_D^T - \mathbf{B}_D + \gamma_D\mathbf{M}_D)\right)\,\mathbf{u}_{\mathbf{n}}, \end{aligned} \tag{4}$$

where $\mathbf{f_0} = \rho\mathbf{M}\mathbf{g} + \mathbf{M}_N\mathbf{t_0}$. Finally, $\mathbf{u}_{\mathbf{n+1}}$ can be calculated using the equations in (3).

2.2 Numerical considerations

The construction of the matrices in the system of linear equations (2) is one of the key challenges of the IBM. To integrate, the domain is split into the volumes of the hexahedral elements. For completely filled elements with $\Omega_e \cap \partial\Omega = \emptyset$, Gauss points commonly yield the integral value. For elements intersecting with the boundary, standard integration techniques do not work as the integration domain might have an arbitrary complexity: the integration domains are either the boundaries intersected with an element, i.e. $\Gamma_{D,h} \cap \Omega_e$ or $\Gamma_{N,h} \cap \Omega_e$, or the intersection of the object with the hexahedral elements, i.e. $\Omega_h \cap \Omega_e$. We integrate exactly over these domains, by using an integration approach depicted in figure 1(bottom), which has been proposed for polynomials up to degree two [11]. The integrands in the last subsection

are polynomial functions where the sum of the polynomial degrees is maximally six, due to the multiplication $\varphi_i\varphi_j$ of the tri-linear shape functions φ_i and φ_j to compute the mass matrices. In the following we use the space of polynomials $\mathbb{P}_M(\mathbb{R}^n)$ that acts on $\mathbb{R}^n$, constructed with monomials, whose sum of degrees is smaller than or equals M. Thus the tri-linear shape functions fulfill $\varphi_i \in \mathbb{P}_3(\mathbb{R}^3)$ and we need to calculate integrals for $\mathbb{P}_6(\mathbb{R}^3)$. For this we extend [11] to arbitrary polynomial degrees: first, the divergence theoreom transforms the volume integral to a sum of integrals of $\mathbb{P}_7(\mathbb{R}^3)$ over polygons in 3D. Then these integrals are projected onto the plane with the biggest surface and one needs to calculate $\mathbb{P}_7(\mathbb{R}^2)$ over polygons in 2D. Finally, these integrals are simplified using Greens' theorem to $\mathbb{P}_8(\mathbb{R}^2)$ over lines in 2D, which can be integrated analytically using binomial coefficients and the positions of the line start and end. For the boundary matrices, the first step is left out but the subsequent steps stay the same with the polynomial degree reduced by one.

Regarding the constitutive model, we use a corotational approach rather than a simple linear strain tensor. This also permits to expand the range of applications of the method. Identically to the conventional approach a rotation matrix $\mathbf{R}_n$ is calculated based on the deformed configuration $\mathbf{u}_n$ of each hexahedral element and incorporated into the system of equations by using $\mathbf{K}_n = \mathbf{R}_n\mathbf{K}_0\mathbf{R}_n^T$, but it is not applied to the other matrices in (2). The rotation matrix in the undeformed configuration equals the identity matrix and is updated when the system of linear equations yields new positions at a time step. In contrary to hyperelastic approaches, the stiffness matrix does not have to be recalculated for every time step, but is updated by multiplying the rotation matrices from both sides. Note that partially filled elements can result in elevated computational costs when integrating for a recalculated matrix, while the calculation of the rotation matrix and the multiplication on the stiffness matrix from both sides is computationally cheap. Thus, the corotational approach is particularly interesting for contexts where the speed of calculation matters, e.g. for simulations in real-time. Moreover, the corotational approach combines nonlinear characteristics with the simplicity of the stress-deformation relationship. However, despite our choices for the corotational approach, we want to emphasize that the IBM we propose is not limited to small strain problems.

Finally, we maintain the numerical stability by ignoring hexahedral elements which are only partially inside the domain. For that, we remove elements where the volume of the integration domain is under 5% of the volume of the hexahedral element. Ignoring these elements has nearly no impact on the end result, improves stability and leads to a slightly smaller system of linear equations.

In summary, the construction of the system matrices and thus the choice of the integration method impacts the initialization time of our algorithm, while the corotational approach reuses the system matrices in order to prevent such time consuming procedures in every time step. To conclude, our method allows for

1. a fast initialization depending upon the number of edges in the high resolution surface mesh, and
2. a fast and stable simulation that depends upon the size and the quality of the linear system of equations which is based on the coarse simulation grid.

3 Results

Here, we present the results of an implementation of our approach into the open source framework SOFA [4]: First, we perform a convergence analysis that compares our algorithm to the classical FEM in beam compression and bending scenarios. Then, we apply the method to simulate a brain shift, a deformation of the brain often observed during neurosurgery.

3.1 Cylinder compression and bending scenarios

To numerically compare our method against the classical FEM, we simulate the compression and bending of beams under gravity while being fixed at one end. The classical bending test results in a deflection, which requires a geometrically nonlinear model of deformation. Thus this example shows one of the motivations to use the corotational approach presented in the previous section.

We consider different cross sections (see figure 2): a circle and a cross section that has convolutions that are similar to the the surface of a brain, see figure 4 bottom. The beam cross sections of the compression example have a radius $r = 0.06$ m, which is expanded $l = 0.1$ m in the length, while for the bending example we have $r = 0.02$ m and $l = 0.2$ m. We choose a Young's modulus of $E = 3000$ Pa and a Poisson's ratio of $\nu = 0.49$ for the compression example and $E = 1$ MPa and $\nu = 0.4$ for the bending to represent deformations close to the application in a brain shift.

We compare our method to the conventional FEM using tetrahedral elements, obtained using the open source meshing library GMSH [5]. For tetrahedral elements with four nodes, incompressible behaviour can yield stiff behaviour, called volumetric locking [1]. Thus, we also compare to the conventional FEM using non-cuboid irregular hexahedral elements in the compression example. Since, to the best of our knowledge, available meshing algorithms can not provide hexahedral meshes, we first mesh a circle with quadrilaterals using GMSH (see figure 3) and then extrude them to hexahedral elements. To show the effect of regular partially filled elements, we compare as well to a sparse regular hexahedral grid: Similarly to our idea, a surfacic structure is overlaid by a regular grid and elements outside of the topology are removed. Contrary to our approach, all elements are filled completely, even elements that are filled only to a small part (see figure 4).

The different results are compared by computing the relative error $d = |\bar{p}_{\mathrm{ref,n}} - \bar{p}_n| / |\bar{p}_{\mathrm{ref,n}} - \bar{p}_0|$, where $|\cdot|$ is the Euclidean norm, $\bar{p}_{\mathrm{ref,n}}$ is the reference beam tip in the middle of the beam, and $\bar{p}_n$ is the tip position for a given simulation after a few simulation steps n (we use subscript 0 for the initial position). The points are depicted as turquoise crosses in figure 2.

The compression example uses a reference solution composed of hexahedra (40887 and 46242 degrees of freedom), while the bending example uses a tetrahedral reference solution (592899 and 514047 degrees of freedom). The high resolution of the chosen reference solutions allows to neglect possible locking error. The

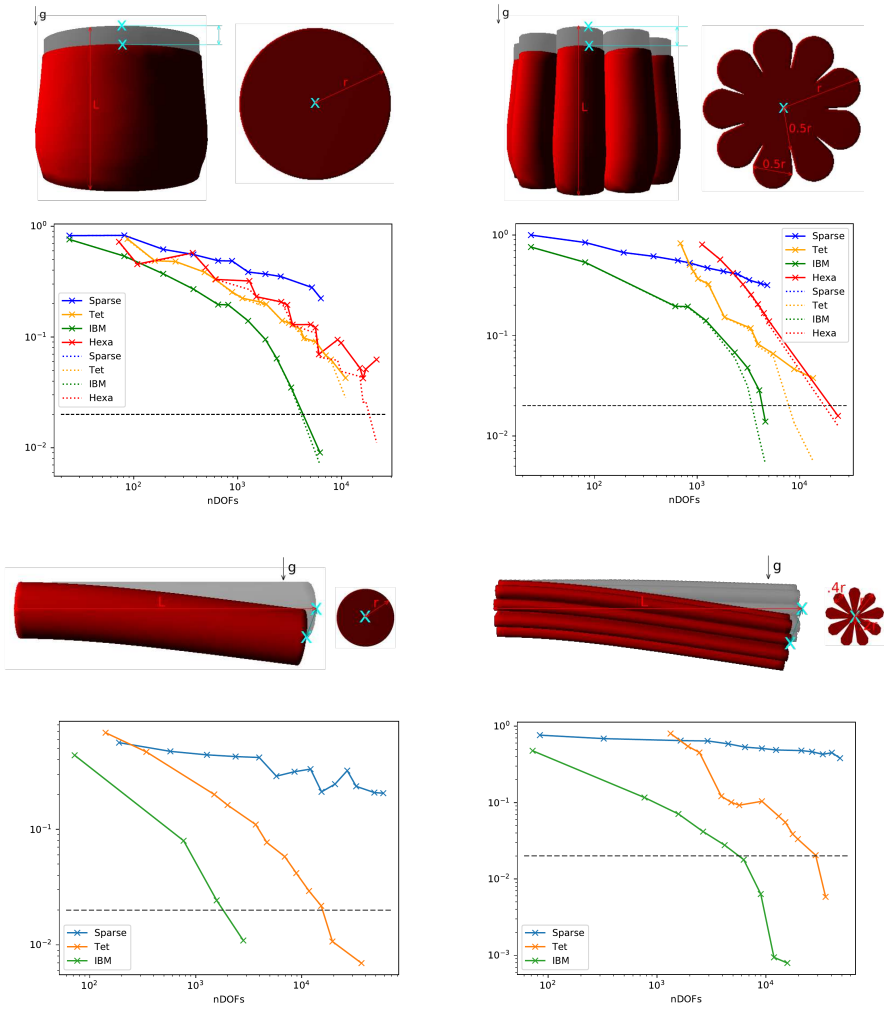

Fig. 2 Compression *(top)* and bending *(bottom)* example with different cross sections *(left/right)*: *Top:* Setup of the example in front *(left)* and top *(right)* view with the initial *(grey)* and final *(red)* configuration of the beam and the point at which we measure the distance in *turquoise*; *Bottom:* Convergence analysis, with the comparison of only the z values as dashed curves and the dashed black line depicts a relative error of 2%.

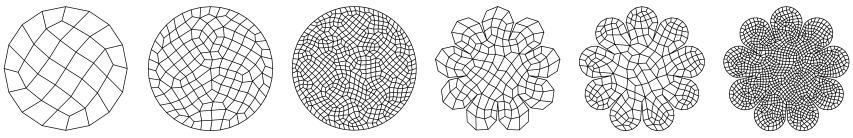

Fig. 3 Cross section of the first example meshed with quadrilaterals of different resolutions.

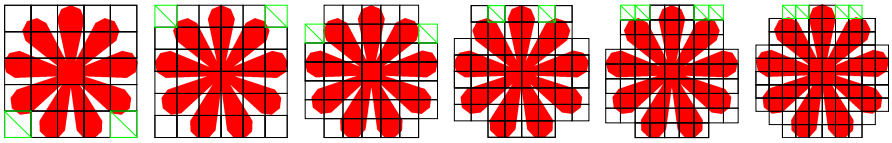

Fig. 4 Bending example: Several chosen resolutions of simulations with a regular hexahedral topology, showing the two-dimensional cross section with the grid: for the sparse grid, all displayed elements are simulated as completely filled, while for the IBM *green* elements are deleted (since they have less than 5% of the hexahedral volume) and boundary elements are partially filled.

results are summarized in a convergence analysis depicted in figure 2. As expected, our approach yields a higher accuracy per degree of freedom than the existing approaches. For the complex geometry with the convolutions in the cross section, the effect is amplified in the second example. When comparing to tetrahedral meshes, our method is particularly interesting for a small number of degrees of freedom. The convergence analysis of the compression example shows for our approach, that the error in the z direction depicted as a dashed line and the relative error are approximately the same. Thus, despite the potentially asymmetric (see figure 4) removal of elements for the immersed boundary method, the impact on the complete mesh stays reasonable low and the deformation is symmetric.

Example	Degrees of freedom			Factor Dofs IBM vs.	
	Tetrahedra	Hexahedra	IBM	Tetrahedra	Hexahedra
Compression	–	–	4956	–	–
Compression with convolutions	–	22892	4368	–	$\frac{22892}{4368} \approx 5.2$
Compression - only z direction	–	18984	4809	–	$\frac{18984}{4809} \approx 3.9$
Compression with convolutions - only z direction	8363	22326	3578	$\frac{8363}{3578} \approx 2.3$	$\frac{22326}{3578} \approx 6.2$
Bending	15924	–	1969	$\frac{15924}{1969} \approx 8.1$	–
Bending with convolutions	28871	–	5813	$\frac{28871}{5813} \approx 5$	–

Table 1 Comparison of the number of degrees of freedom for an accuracy of 2%.

3.2 Brain shift simulation

In order to assess our method in the medical context, it has been applied to simulate a brain deformation, frequently occuring after a craniotomy, see figure 5. The brain surface mesh is highly detailed, with 88,580 triangles and 44,261 points, and contains a lot of anatomical details due to the presence of sulci and gyri. The bounding box of the surface mesh is then simply subdivided into a regular grid with 9, 11 and 11 points in each principal direction, resulting in a sparse grid with 675 nodes P_i. Dirichlet boundary conditions are then applied to the actual surface (and not to the nodes of the grid) as explained in section 2 and depicted in figure 5 (left). Other interactions such as collision between the scull and the brain are disregarded. The convolutions are in most cases inside one element or two neighboring elements that

are connected, which allows to handle auto collisions without external algorithms, iff the elements should not invert themselves. Since Dirichlet boundary conditions in the standard FEM are applied to the nodes and not on a part of a face as in our approach, no comparisons to existing approaches were performed. Using a Young's modulus $E = 3000$Pa, a Poisson's ratio of 0.49 and a mass density of $1027kg/m^3$ the computation of the brain shift did not involve complex volumetric meshing and has been performed using the damping parameters $\alpha = \beta = 0.1$.

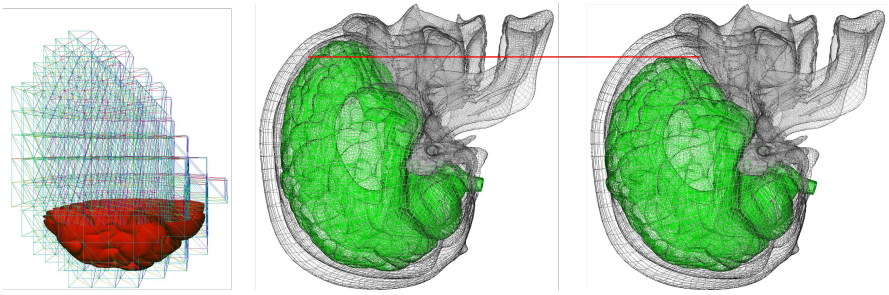

Fig. 5 Simulation of brain shift using a detailed surface mesh embedded into an hexahedral grid. Boundary conditions are applied onto the exact surface, not the grid *(left)*.

4 Conclusion and Perspectives

In this paper, we have introduced an adaptation of the Immersed Boundary Method, generally used for fluid dynamics problems, to the context of patient-specific simulation of soft tissue deformation. The benefit of our method over conventional Finite Element Methods lies in the ability to handle complex geometries while using a regular, relatively coarse, hexahedral, unfitted mesh. In particular, no auxiliary mesh is required. The complexity of the non-standard numerical integration over the cut elements remains proportional to the number of surface elements. The number of degrees of freedom and thus the size of the linear system in every time step is only proportional to the number of coarse elements and independent of the number of geometric features of the boundary. In contrast to the standard Finite Element approach, fixed displacement boundary conditions can be applied to the high resolution surface mesh and are propagated to the potentially coarse hexahedral simulation mesh. These different advantages make the method a promising approach for building patient-specific coarse simulations in an automated way.

Yet, we believe this is only a first step towards a new way of constructing Finite Element simulations over complex domains defined in medical images. As the underlying integration can deal with holes in the surface, the approach has the built-in potential to compensate for incomplete surface reconstruction due to missing or wrong data. This could make the method even more robust and adapted to medical images. Furthermore, the fact that dynamic simulations are directly obtained from surface meshes segmented from medical images and do not require dedicated volu-

metric meshing techniques could make the method a very valuable and user-friendly tool in the context of medical simulation.

References

1. Steven E Benzley et al. A comparison of all hexagonal and all tetrahedral finite element meshes for elastic and elasto-plastic analysis. In Proceedings, 4th International Meshing Roundtable, volume 17, pages 179–191, 1995.
2. Erik Burman, Susanne Claus, Peter Hansbo, Mats G Larson, and André Massing. Cutfem: Discretizing geometry and partial differential equations. International Journal for Numerical Methods in Engineering, 104(7):472–501, 2015.
3. Stéphane Cotin, Hervé Delingette, and Nicholas Ayache. Real-time elastic deformations of soft tissues for surgery simulation. IEEE transactions on Visualization and Computer Graphics, 5(1):62–73, 1999.
4. F. Faure et al. Sofa: A multi-model framework for interactive physical simulation. 2012.
5. Christophe Geuzaine et al. Gmsh: A 3-d finite element mesh generator with built-in pre-and post-processing facilities. 2009.
6. W. Hackbusch and S.A. Sauter. Composite finite elements for the approximation of pdes on domains with complicated micro-structures. Numerische Mathematik, 75(4):447–472, 1997.
7. Songbai Ji, James C Ford, Richard M Greenwald, et al. Automated subject-specific, hexahedral mesh generation via image registration. Finite Elements in Analysis and Design, 47(10):1178–1185, 2011.
8. Vladimir D Liseikin. Grid generation methods. 2009.
9. André Massing, Mats G Larson, and Anders Logg. Efficient implementation of finite element methods on nonmatching and overlapping meshes in three dimensions. SIAM Journal on Scientific Computing, 35(1):C23–C47, 2013.
10. Karol Miller. Constitutive model of brain tissue suitable for finite element analysis of surgical procedures. Journal of biomechanics, 32(5):531–537, 1999.
11. Brian Mirtich. Fast and accurate computation of polyhedral mass properties. journal of graphics tools, 1(2):31–50, 1996.
12. Joachim Nitsche. Über ein variationsprinzip zur lösung von dirichlet-problemen bei verwendung von teilräumen, die keinen randbedingungen unterworfen sind. volume 36, pages 9–15. Springer, 1971.
13. Steven J Owen. A survey of unstructured mesh generation technology. 1998.
14. Jamshid Parvizian, Alexander Düster, and Ernst Rank. Finite cell method. Computational Mechanics, 41(1):121–133, 2007.
15. Christoph J Paulus et al. Handling topological changes during elastic registration. 2016.
16. Charles S Peskin. Flow patterns around heart valves: a numerical method. Journal of computational physics, 10(2):252–271, 1972.
17. Charles S Peskin. The immersed boundary method. Acta numerica, 11:479–517, 2002.
18. Daniel Peterseim and Stefan A Sauter. The composite mini element - coarse mesh computation of stokes flows on complicated domains. SIAM Journal on Numerical Analysis, 46(6):3181–3206, 2008.
19. Markus Rech, S Sauter, and Anton Smolianski. Two-scale composite finite element method for dirichlet problems on complicated domains. Numerische Mathematik, 102(4):681–708, 2006.
20. Thomas Rüberg, Fehmi Cirak, and José Manuel García Aznar. An unstructured immersed finite element method for nonlinear solid mechanics. AMSES, 3(1):22, 2016.
21. Peter Wriggers. Nonlinear finite element methods. Springer Science & Business Media, 2008.

A Flux-Conservative Finite Difference scheme for the numerical solution of the nonlinear bioheat equation

George C. Bourantas[1], Grand R. Joldes[1,2], Adam Wittek[1], Karol Miller[1,3]

[1]Intelligent Systems for Medicine Laboratory, School of Mechanical and Chemical Engineering, The University of Western Australia, 35 Stirling Highway, Crawley/Perth, WA 6009, Australia
[2]School of Engineering and Information Technology, Murdoch University, 90 South St, Murdoch, Australia
[3]School of Engineering, Cardiff University, The Parade, CF24 3AA Cardiff, United Kingdom

Abstract

We present a flux-conservative finite difference (FCFD) scheme for solving the nonlinear (bio)heat transfer in living tissue. The proposed scheme deals with steep gradients in the material properties for malignant and healthy tissues. The method applies directly on the raw medical image data without the need for sophisticated image analysis algorithms to define the interface between tumour and healthy tissues.

We extend the classical finite difference (FD) method to cases with high discontinuities in the material properties. We apply meshless kernels, widely used in Smoothed Particle Hydrodynamics (SPH) method, to approximate properties in the off-grid points introduced by the flux conservative differential operators. The meshless kernels can accurately capture the steep gradients and provide accurate approximations. We solve the governing equations by using an explicit solver. The relatively small time-step applied is counterbalanced by the small computation effort required at each time step of the proposed scheme. The FCFD method can accurately compute the numerical solution of the bioheat equation even when noise from the image acquisition is present.

Results highlight the applicability of the method and its ability to solve tumor ablation simulations directly on the raw image data, without the need to define the interface between malignant and healthy tissues (segmentation) or meshing.

Keywords: Flux-Conservative Finite Difference, Tumor Ablation, Bioheat Equation, Meshless Method

Introduction

Image-guided thermal ablation is a minimally invasive treatment of localized solid tumors. Energy sources, like radiofrequency ablation (RFA), microwaves (MW), high-intensity focused ultrasound (HIFU) and light amplification by stimulated emission of radiation (LASER), deliver thermal energy to cancerous lesions. Exposure to heat may render cancer cells more sensitive to radiation or even directly attack cancer cells that show reduced sensitivity to radiation [1,2].

Tumor ablation simulations are based on the Pennes bioheat equation [3]. Herein, we present a flux conservative finite difference method (FCFD) [4 and references therein], which deals efficiently with high discontinuities in the material properties of the tumor and the healthy tissue when solving Pennes equation. During ablation, the material properties are continuously changing and, in some cases, steep gradients occur. The well-established mesh based methods cannot easily deal with sharp interfaces [5], as they work efficiently only for interface conforming meshes. When the mesh does not conform to the interface (cross the interface), mesh based methods fail to provide accurate numerical results for the bioheat equation. Finite difference (FD) methods treat inhomogeneous material properties without any information about the interface. They can be applied directly on a Cartesian grid. Consequently, there is no need for an explicit representation of the interface in the model.

The proposed FCFD scheme can be incorporated into an integrated feedback control system, that integrates computer models with field measurement systems (e.g. Thermal MRI (TMRI), Ultrasound (US)) to allow near-real-time calibration of the models. These integrated systems can provide predictive guidance and control of medical procedures using medical image modalities already available in the operating theatre. Furthermore, the absence of mesh generation drastically decreases the computational burden and provides avenues for a real-time in-situ treatment planning system. The solution method developed in this work employs a flux-conservative finite difference scheme to solve the nonlinear bioheat equations. The scheme uses a Cartesian grid obtained directly from DICOM image data and, therefore, it can be used directly with magnetic resonance thermal imaging. In this paper, we examine the accuracy of the FCFD scheme against a solution method that takes into account the interface between different materials. Furthermore, we show the applicability of the method on realistic image data and examine the computational cost by considering 2D and 3D examples.

The outline of the paper is as follows. In the Methods Section, we present an overview the governing flow equations and discuss the flux-conservative finite difference discretization and the meshless interpolation scheme employed to approximate material properties when computing the heat fluxes. We demonstrate the accuracy and the robustness of the proposed scheme in the Results Section. We summarize the results of using the flux-conservative FD formulation for solving the bioheat equation in the Conclusions Section.

Methods

Governing Equations

The most popular bioheat equation for modeling thermal therapies is the Pennes bioheat equation, which accounts for blood perfusion and metabolic heat generation [3].

$$\rho c \frac{\partial T}{\partial t} = \boldsymbol{\nabla}(k(\boldsymbol{x}, T)\boldsymbol{\nabla}T) + \omega_b \rho_b c_b (T_a - T) + Q_m + Q_r(\boldsymbol{x}, t) \quad (1)$$

with ρ (kg/m^3) being the mass density, c [J/(kg K)] the specific heat capacity, k [W/(m K)] the tissue (healthy and malignant) thermal conductivity, and ω_b [kg/(m^3 s)], ρ_b (kg/m^3), and c_b [J/(kg K)] represent blood perfusion, density, and specific heat of blood, respectively. T_a(K) is the arterial temperature which is treated here as constant, and $T(\boldsymbol{x},t)$ is the local tissue temperature. Q_m (W/m^3) is the metabolic heat generation, and $Q_r(\boldsymbol{x},t)$ (W/m^3) is the spatial heating rate that is provided by an external heat source. The governing equations represent heat conduction in the tissue, caused by the temperature gradient, and heat transfer between the tissue matrix and local microcirculation.

The majority of bioheat models use the Pennes bioheat equation, which is based on the classical Fourier law and accounts for blood flow through a temperature-dependent heat source term. The Pennes equation cannot capture accurately the effects of large blood vessels. Possible solutions to account for the heat sink caused by large blood vessels would be either to specify an effective convective heat transfer coefficient along the vessel surface or include a complex relationship between blood flow dynamics in the vessel and transient temperature. However, it is widely accepted that even without application of these solutions, the Pennes equation remains a remarkably effective method for modeling heat transfer in tissue during thermal ablation [3].

Pennes equation neglects certain physical phenomena that take place during thermal ablation, mainly water evaporation and thermal tissue damage. Experimental and clinical observations suggest that heating to high temperatures initiates partial evaporation of tissue water [6, 7]. In fact, the entire process of water evaporation, water vapor diffusion, and condensation is a process of water and energy redistribution and is as significant as direct thermal conduction. These processes may become dominant for tissue temperature approaching 100^{o}C. The bioheat equation can be extended to incorporate these phenomena. The power density that is used for evaporation is related to the change in water content of tissue as follows

$$Q_E = -\beta \frac{\partial W}{\partial t} \quad (2)$$

where β is the water latent heat constant, equal to 2260 kJ/kg, and W is the tissue water density (kg/m^3), which is a function of temperature. By using the chain rule, the time derivative of W is

$$\frac{\partial W}{\partial t} = \frac{dW}{dT}\frac{\partial T}{\partial t} \tag{3}$$

Substituting this in Eq. (2) yields

$$Q_E = -\beta \frac{dW}{dT}\frac{\partial T}{\partial t} \tag{4}$$

By including temperature dependent thermal properties and the effect of water evaporation, the extended bioheat equation becomes

$$\left(\rho(T)\frac{dc}{dT}T + \frac{d\rho}{dT}c(T)T + \rho(T)c(T) - \beta\frac{dW}{dT}\right)\frac{\partial T}{\partial t} = \boldsymbol{\nabla}(k(\boldsymbol{x},T)\boldsymbol{\nabla}T) + \omega_b\rho_b c_b(T_a - T) + Q_m + Q_r \tag{5}$$

One of the important challenges in ablation treatment is determining and controlling the amount of tissue damaged during ablation. Several theoretical models have been proposed over the last few years to address this challenge [8]. Measurements have shown that blood perfusion in response to elevated temperature is a complex function of both temperature and time [9, 10]. Moreover, because of differences in the vasculature of tumor, blood perfusion within the tumor is probably quite different from that of normal tissue [11]. Taking these aspects into consideration, tissue thermal damage due to temperature elevations in the tissue over a threshold value for a given time can be described by an Arrhenius-type equation [12]:

$$\Omega = \int_0^t P e^{-\frac{\Delta E}{RT(\boldsymbol{x},t)}}\, dt \tag{6}$$

where Ω is a measure of the extent of thermal damage to the tissue, P is a material dependent proportionality constant, ΔE is the material activation energy, and R is the universal gas constant. The undamaged and damaged fractions of the tissue can be written as f_u=e$^{-\Omega}$ and f_d=1-f_u, respectively. Some of the parameters in the extended bioheat equation can be considered as functions of tissue damage.

Numerical Solution of The Bioheat Equation

Flux-Conservative Finite Difference Scheme

Solving numerically heat conduction in heterogeneous media that include both malignant and healthy tissue is a computationally demanding problem due to the inherent nonlinearity. The identification of different regions and the precise

handling of interfaces require tedious mathematical treatment, mainly for the nonlinear terms and heterogeneities in the material properties, which complicate the solution of the heat conduction problem [13]. The typically used methodology requires the creation of conforming meshes between regions of different conductivity and the calculation of local normal vectors at the tumor/tissue interface, which tends to be a cumbersome for complicated geometries [13].

We propose the flux-conservative finite difference (FCFD) method as a suitable numerical method to solve extended bioheat equation. FCFD method works efficiently on Cartesian grids (that can be directly obtained from DICOM images), and computes the nonlinear convective term $\boldsymbol{\nabla}(k(\boldsymbol{x},T)\boldsymbol{\nabla}T)$ by applying a flux-conservative scheme. This scheme computes spatial derivatives for the temperature field using the stencil defined in Fig. 1.

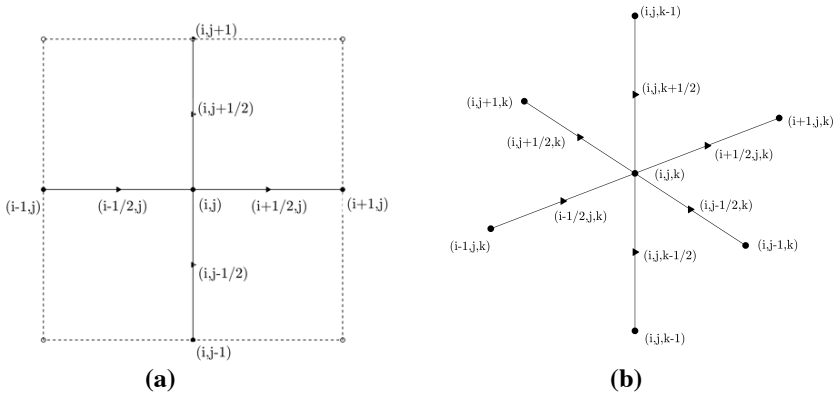

Fig. 1. The stencil configuration used in the flux-conservative finite difference method for **(a)** 2D and **(b)** 3D geometry.

This is identical to the classical FD stencil, with the only difference that in the stencils defined in Fig. 1 fluxes in the fictitious grid points ((i+1/2,j), (i-1/2,j), (i,j+1/2), (i,j+1/2)) are preserved. Flux-conservative finite-difference discretization should be used in cases when the bioheat equation contains a variable thermal conductivity. Computation of the convective term at the grid points ((i,j), (i-1,j), (i,j+1), (i,j+1), (i,j-1)) will lead to an erroneous non-conservative FD formulation. Application of classical (non-conservative) FD stencil by directly applying the chain rule to compute the spatial derivatives of the convective term will lead to incorrect calculation of thermal fluxes. Therefore, we use flux-conservative FD treatment of bioheat equation, with the nonlinear convection term ∇(k∇T) written as:

$$\boldsymbol{\nabla}(k\boldsymbol{\nabla}T) = \frac{\partial}{\partial x_m}\left(k\frac{\partial T}{\partial x_m}\right) \tag{7}$$

with m=(x,y,z) and using the Einstein summation convention. By using the flux conservative approach, the terms at the central node (i,j) of the stencil shown in Fig.1 can be written (for the x coordinate) as

$$\frac{\partial}{\partial x}\left(k\frac{\partial T}{\partial x}\right)=\frac{k_{(i+1/2,j)}\left(\frac{\partial T}{\partial x}\right)_{(i+1/2,j)}-k_{(i-1/2,j)}\left(\frac{\partial T}{\partial x}\right)_{(i-1/2,j)}}{\Delta x} \tag{8}$$

and, by computing the derivative terms based on the Cartesian grid nodes, can be written as

$$\begin{aligned}\frac{\partial}{\partial x}\left(k\frac{\partial T}{\partial x}\right)=&\frac{k_{(i-1/2,j)}}{(\Delta x)^2}T_{(i-1,j)}-\frac{\left(k_{(i-1/2,j)}+k_{(i+1/2,j)}\right)}{(\Delta x)^2}T_{(i,j)}\\&+\frac{k_{(i+1/2,j)}}{(\Delta x)^2}T_{(i+1,j)}\end{aligned} \tag{9}$$

After obtaining the terms for the y- and z- coordinates in the same manner, we can compute the nonlinear convective term in the bioheat equation using Eq. 7. Note that we have to use thermal conductivity values $k_{(i\text{-}1/2,j)}$, $k_{(i+1/2,j)}$, $k_{(i,j\text{-}1/2)}$ and $k_{(I,j+1/2)}$ for the additional nodes where the heat fluxes are defined. If these values are unknown, they can be computed by e.g. arithmetic averaging of known thermal conductivities on the grid nodes or by using the harmonic average. The former applies for the $k_{(i+1/2,j)}$ conductivity as

$$k_{(i+1/2,j)}=\frac{k_{(i+1,j)}+k_{(i,j)}}{2} \tag{10}$$

while the latter is written as

$$k_{(i+1/2,j)}=\frac{2k_{(i+1,j)}k_{(i,j)}}{k_{(i+1,j)}+k_{(i,j)}} \tag{11}$$

These two approaches, despite their success in delivering reliable results, may result in decreased accuracy of the numerical solution when steep gradients in material properties (higher than 6 orders of magnitude) are present. This is because only the two nodes adjacent to the fictitious point are used in the computation, disregarding all the other nodes in the close vicinity.

Meshless methods are numerical methods initiated two decades ago, which use sophisticated techniques to approximate unknown field functions in point clouds. In the following subsection, we briefly describe the meshless method used to approximate the thermal conductivity at the fictitious points defined in the FCFD stencils.

Meshless Approximation Methods

A number of interpolating/approximating methods are described in the meshless literature [14, 15]. Among them, the most widely used are the Moving Least Squares (MLS) [16], Modified Moving Least Squares (MMLS) [17], Radial Basis Functions (RBF) [15], Discretization Corrected Particle Strength Exchange

(DC PSE) [18] and Smoothed Particle Hydrodynamics (SPH) [14]. Each one of these approximation methods can be used for projecting field values from markers to Eulerian grid nodes. In our approach, we are using SPH kernels, due to their simplicity and low computational cost (there is no need to construct and numerically invert a matrix when computing the shape functions).

In the context of kernel-based interpolation, any function $A(\boldsymbol{x})$ is approximated by an integral:

$$A(\boldsymbol{x}) \approx \int A(\boldsymbol{x}) W(||\boldsymbol{x} - \boldsymbol{x}'||, h) d\boldsymbol{x}' \tag{12}$$

where W is the weighting function (or kernel) and h is the smoothing length. Based on the above continuum approximation, a discrete approximation can be obtained as:

$$A(\boldsymbol{x}) \approx \sum_i A_i W(||\boldsymbol{x} - \boldsymbol{x}_i||, h) \tag{13}$$

with A_i being the values of the function $A(\boldsymbol{x})$ at discrete points $\boldsymbol{x}_i$ and the summation being over particles i located in the support domain of the kernel function. The accuracy of the approximation scheme depends on the choice of the weighting function, which is a normalized function, positively defined, with compact support and monotonically decreasing with increasing distance from the node with coordinate $\boldsymbol{x}$. Among a variety of possible kernels, we use in our simulations the quadratic kernel

$$W(r, h) = a_Q \left(\frac{3}{16} q^2 - \frac{3}{4} q + \frac{3}{4} \right), \quad 0 \le q \le 2 \tag{14}$$

with q being the normalized distance q=r/h and a_Q the dimension-dependent normalization constant.

Results

Code verification

To verify the accuracy of the proposed scheme, the Pennes equation (Eq. (1)) is numerically solved on a rectangular region with dimensions 2L (L=0.05 m), with a square tumor of size L/4 located at the center of the region, as shown in Figure 2a. The physical properties of tissues are realistic, with the thermal conductivity for the healthy tissue given as k_{HT}=0.5 W/(m K) and for the tumor k_T=10 W/(m K), the density of the tumor and healthy tissue ρ_{HT}=ρ_T=1052 kg/m^3, heat capacity c_p=3800 J/(kg K), blood perfusion for the healthy tissue ω_{HT}=0.0001 s^{-1} and for the tumor ω_{bT}=0.01 s^{-1}, metabolic Q_m=4000 W/m^3, and a heating source Q_r=100t W/m^3 that covers this region. At the boundaries, h=20 W/(m^2 K), T_f=20ºC, and T_a=37ºC [12]. The time step is set to dt=1 s, and the initial temperature distribution is obtained from the steady state solution [13]. The heating source form used is arbitrarily

chosen; the only purpose is to validate the applicability of the proposed scheme to cases with time-dependent heat sources. The domain has been discretized using 100x50 equally spaced nodes.

Figure 2b presents the transient temperature profiles along the line x=0. The results are compared with the ones obtained using the meshless point collocation method [13], which takes into account the boundary between tumor and healthy tissue. The results obtained using the two methods are in excellent agreement.

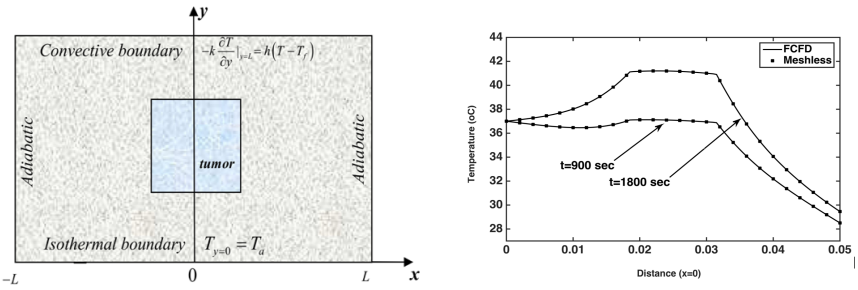

Fig. 2. (a) Geometry and boundary conditions used in the verification study and **(b)** transient temperature profiles for the verification test case along the line y=0 using the proposed flux-conservative finite difference scheme combined with the meshless approximation method (results are compared against the meshless point collocation method [12], which takes into account the boundary between tumor and healthy tissue)

Example 1: 2D computation of temperature distribution within soft tissue using image data

The next case study considers a random conductivity field with different mean values for the tumor and healthy tissue, similar to the ones obtained from noisy medical images. Using the same problem setup as in the previous example, the conductivity in each region is assigned values that are randomly sampled from a uniform distribution with mean values of k_{HT}=0.5 W/(m K) and k_T=10 W/(m K) for the healthy tissue and the tumor, respectively, and a variation interval of 10% in both cases. Such data is similar to actual data from medical DICOM images, such as thermal MRI scans, and brings out the frequent, practical problem of a relatively uncertain definition of the precise border between the pathological and healthy parts of the tissue. A gray-scale representation of the conductivity field is shown in Fig. 3a.

We solve the bioheat equation using the flux-conservative finite different solver, without the need to define the interface between the healthy tissue and the tumor. The temperature profile along the midline (x=0) is in excellent agreement with that computed in the previous example, which assumes that the conductivity in each region is uniform and equal to the mean value that was prescribed here.

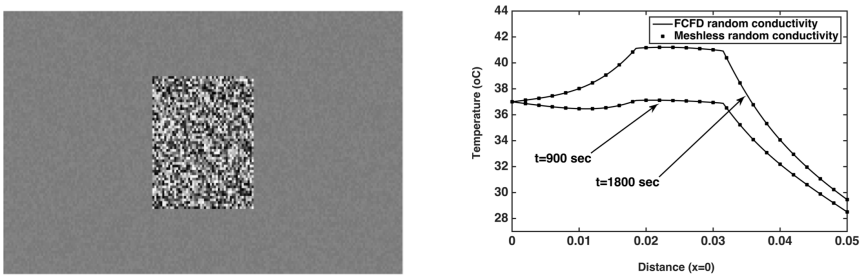

(a) **(b)**

Fig. 3. (a) Gray-scale representation of the random conductivity field with k_{HT}=0.5 W/(*m* K) and k_T=10 W/(*m* K), uniform distributed within a 10% variation interval. **(b)** Transient temperature profiles for the verification test case along the line x=0 using the flux-conservative finite difference scheme

Example 2: 3D computation of temperature distribution within soft tissue

We solve the extended bioheat equation in 3D, accounting for water evaporation and tissue damage and considering temperature dependence of all major physical and thermal properties of the tissue (malignant and healthy). Given small changes in density and conductivity, the first two terms in the left-hand side in Eq. (7) can be neglected [19] and the bioheat equation becomes:

$$\left(\rho(T)c(T) - \beta\frac{dW}{dT}\right)\frac{\partial T}{\partial t} = \boldsymbol{\nabla}(k(\boldsymbol{x},T)\boldsymbol{\nabla}T) + \omega_b\rho_b c_b(T_a - T) + Q_m + Q_r \quad (15)$$

The dependence of the tissue water content on temperature is obtained by fitting experimental data, to obtain an empirical function [19]:

$$w(T) = \begin{cases} 0.728 + 8.48e^{-2\left(\frac{T-123.286}{16.634}\right)^2} & T \le 103 \\ 0.024 + \dfrac{4.531}{1 + e^{\left(\frac{T-30.173}{28.012}\right)^2}} & T > 103 \end{cases} \quad (16)$$

Dynamic changes in blood perfusion rate with temperature and tissue damage are included in the model as

$$\omega_b(T,\Omega) = \omega_{b0} f_T f_u \quad (17)$$

where ω_{b0} is the constitutive perfusion rate and f_u=1–f_T, with f_T being a dimensionless function that accounts for vessel dilation at slightly elevated temperatures, which can be approximated as

$$f_T = \begin{cases} 4 + 0.6(T - 42°\text{C}) & 37°\text{C} \le T < 42°\text{C} \\ 4 & T > 42°\text{C} \end{cases} \quad (18)$$

We solve the extended bioheat equation numerically using the FCFD method over a cubical geometry of length L=0.02 *m* and assuming adiabatic boundary conditions at all six faces. A heat source of finite volume is placed at the middle of a circular tumour of radius 0.002 *m*.

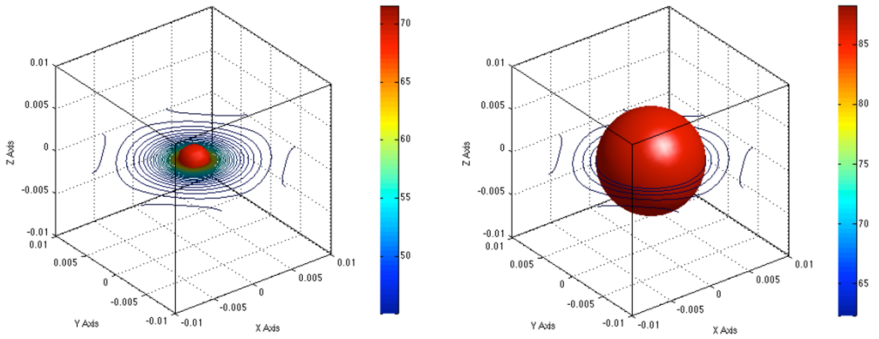

(a) **(b)**

Fig. 4. Temperature isocontour values (T=65ºC) plots at (a) 600 s and (b) 1800 s obtained by using the flux-conservative finite difference scheme. The heat source is placed in the center of the tumor located in the cube center.

The symmetrical geometry setup used facilitates the imposition of thermal boundary conditions. The length of the surrounding tissue has to be large enough compared to the dimensions of the tumor and sufficiently far from the heat source in order for the imposed boundary conditions to accurately describe the actual phenomena. We solve the governing equations for a time of 1800 s, applying a uniform heat source of Q_r=750 MW m^{-3}. Initially, the temperature is set to T_0 = 37°C for the entire spatial domain. The material properties are the same as the ones used in reference [19]. Figure 4 shows the isocontour value for T=65ºC, obtained using the proposed scheme FCFD method, at different time steps of the ablation treatment.

Conclusions

In the present study, we present a flux-conservative finite difference scheme combined with a meshless approximation method to solve transient bioheat transfer problems using a Eulerian-type approximation. The bioheat equation was extended to account for water evaporation, tissue damage, and temperature-dependent properties. Using this formulation, one can circumvent the need for segmenting the problem domain in order to define the precise interface between healthy tissues and tumor. This simplifies the treatment of parameter discontinuities in the model.

We illustrate the applicability of the proposed method using typical examples that appear in therapeutic treatments, such as ablation of a tumor surrounded by healthy tissues, in two and three dimensions. Comparison of numerical results obtained with other numerical methods, which take into consideration the interface between tissues, showed that the method provides excellent predictions of the temperature profile, both in tumors and in the healthy parts of the tissue, when directly using the image as a model.

Acknowledgements

This research was supported partially by the Australian Government through the Australian Research Council's Discovery Projects funding scheme (project DP160100714). The views expressed herein are those of the authors and are not necessarily those of the Australian Government or Australian Research Council. In addition, we wish to acknowledge the Raine Medical Research Foundation for funding G. R. Joldes through a Raine Priming Grant, and the Department of Health, Western Australia, for funding G. R. Joldes through a Merit Award.

Bibliography

1. van der Zee, J., *Heating the patient: a promising approach*?. Annals of oncology: official journal of the European Society of Medical Oncology/ESMO, 2002. **13**: p. 1173-1184.
2. Moyer, H.R. and Delman, K.A., *The role of hyperthyrmia in optimizing tumour response to regional therapy*. International journal for hyperthermia, 2008. **24**: p. 251-261.
3. Pennes, H.H., *Analysis of tissue and arterial blood temperatures in the resting human forearm*. Journal of applied physiology, 1948. **1**: p. 93-122.
4. Gerya, T.V., Introduction to Numerical Geodynamic Modelling. Cambridge University Press, New York, 2010.

5. Moresi, L., Zhong, S., and Gurnis M,. *The accuracy of finite element solutions of Stokes's flow with strongly varying viscosity*. Physics of the Earth and Planetary Interiors, 1996. **97**(1-4): p. 83-94.
6. Yang, D., et al., *Measurement and analysis of tissue temperature during microwave liver ablation*. IEEE Transactions on Biomedical Engineering, 2007. **54**: p. 150-155.
7. Stauffer, P.R., et al., *Phantom and animal tissues for modelling the electrical properties of human liver*. International Journal of Hyperthermia, 2003. **19**: p. 89-101.
8. Dewey, W.C., Diederich, C.J., *Hyperthermia classic commentary:'Arrhenius relationships from the molecule and cell to the clinic*'. International Journal of Hyperthermia, 2009. **10**: p. 457-483.
9. van Vulpen, M., et al., *Prostate perfusion in patients with locally advanced prostate carcinoma treated with different hyperthermia techniques*. Journal of Urology, 2009, **168**: p. 1597-1602.
10. He, X., et al., *Investigation of the thermal and tissue injury behaviour in microwave thermal therapy using a porcine kidney model*. International Journal of Hyperthermia, 2004. **20**: p. 567-593.
11. Prakash, P., *Theoretical modeling for hepatic microwave ablation*. The Open Biomedical Engineering Journal, 2010. **4**: p. 27-38.
12. Welch, A.J., van Gemert, M., Optical-thermal Response Of Laser-irradiated Tissue. Plenum Press: New York, 1995.
13. Bourantas, G.C., et al., *A meshless point collocation treatment of transient bioheat problems*. International Journal for Numerical Methods in Biomedical Engineering, 2014. **30**(5): p. 587-601.
14. Liu, G.R., *Mesh Free Methods: Moving Beyond the Finite Element Method*. CRC Press, 2002.
15. Fasshauer, G., Meshfree Approximation Methods with MATLAB. World Scientific Publishers. Singapore, 2007.
16. Lancaster, P., Salkauskas, K., *Surfaces generated by moving least squares methods*. Mathematics of Computation, 1981. 37(155): p. 141-158.
17. Joldes, G.R., etal., *Modified moving least squares with polynomial bases for scatterd data approximation*. Applied Mathematics and Computation, 2015. **266**: p. 893-902.
18. Bourantas, G.C., et al., *Using DC PSE operator discretization in Eulerian meshless collocation methods improves their robustness in complex geometries*. Computers & Fluids, 2016. **136**: p. 285-300.
19. Bourantas, G.C., et al., *Real-time tumor ablation simulation based on the dynamic mode decomposition method*. Medical Physics, 2014. 41(5): p. 053301-11.

Quantifying Carotid Pulse Waveforms Using Subpixel Image Registration

[1]Amir HajiRassouliha, [1]Emily Lam Po Tang, [1,2]Martyn P. Nash, [1,2]Andrew J. Taberner, [1,2]Poul M. F. Nielsen, and [3]Yusuf O. Cakmak

[1]Auckland Bioengineering Institute (ABI), The University of Auckland,
[2]Department of Engineering Science, The University of Auckland,
[3] Department of Anatomy, University of Otago
ahaj975@aucklanduni.ac.nz

Abstract. Cardiovascular diseases are a common cause of death. Symptoms of cardiovascular disease often arise at a stage of the disease where treatments are ineffective. Hence, methods that can help early diagnosis of heart problems are essential for preventing heart failure. Assessing the shape of the carotid artery waveforms is one of the methods that clinicians use to diagnose heart and valvular diseases, such as hypertrophic obstructive cardiomyopathy, aortic stenosis, and aortic regurgitation. The carotid artery waveforms may be estimated using pulsed-Doppler ultrasound devices, or quantified using catheterisation. However, both of these solutions have limitations. Currently, among available solutions, there is no inexpensive, non-invasive objective method, or diagnostic tool for estimating or quantifying the carotid waveforms. To address these limitations, we have designed a portable non-contact camera-based device to quantify the carotid arterial waveforms. The proposed device calculates the vessel-induced deformation of skin from videos taken from the neck to estimate the carotid artery pressure waveforms. This device takes advantage of our precise and sensitive subpixel image registration algorithm to measure skin deformations from sequential frames of the videos. The skin deformations obtained using our device were compared against a laser displacement measurement device with a resolution of 0.2 μm, and a correlation score of 0.95 was achieved for five subjects.
The carotid artery waveforms measured using this device can provide beneficial information for early detection of heart disease. Furthermore, the data gathered using this device can be used to develop computational models of the carotid artery and/or the cardiac systolic and diastolic phases.

Keywords: Carotid artery, pressure, deformation, subpixel image registration

1. Introduction

Cardiovascular disease causes 31.5 % of all deaths — more than twice the number caused by cancer [1]. The heart pumps blood through arterial vessels to

deliver oxygen and nutrients to tissue, and blood returns to the heart via venous vessels. The examination of pressure within blood vessels can give clinicians an indication of the status of the heart. The pressure wave travels quickly in the arterial tree with each contraction of the heart, at a rate far faster than the blood flow itself. While peripheral arteries are not suitable for detecting related pathological waveforms of the cardiac systolic and diastolic phases, the carotid artery and the jugular vein can be of great use to clinicians to detect heart problems as they are situated close to the heart [2]. The pressure in the carotid artery is an important measure, as it can indicate to clinicians some of the heart problems, such as hypotension, hypertension, aortic valve stenosis, aortic valve regurgitation, and hypertrophic obstructive cardiomyopathy [3].

Pulsed-Doppler ultrasound devices have often been used to estimate the shape of the pressure and flow waveforms in the vessels, and thereby reveal abnormalities in the cardiovascular system. The changes in the internal diameter are closely related to the pressure in the artery and can be estimated using, for example, ultrasound images. The shape of the carotid blood pressure waveform in normal subjects has two peaks. Fig. 1**:** shows the blood flow waveforms caused by the carotid artery and arterial diameter changes in a healthy male subject measured by Soleimani et al. [4]. Variations of the carotid arterial waveforms from its normal shape (Fig. 1**:**) can be a sign of heart disease. For instance, in patients with hypertrophic obstructive cardiomyopathy (HCM) [5], there is a rapid upstroke to the first peak and a slower rise to the second peak of the arterial pressure waveform [6] (HCM is a relatively common cardiac disease which affects 1 out of 500 in the general population [7]). Furthermore, examination of the waveform can help with the diagnosis of valvular heart disease, such as aortic stenosis and aortic regurgitation. Measurement of the carotid blood flow waveforms is thus an important clinical procedure. Moreover, the carotid arterial waveform and pressure data provides useful information for modelling and predicting the heart function [8, 9].

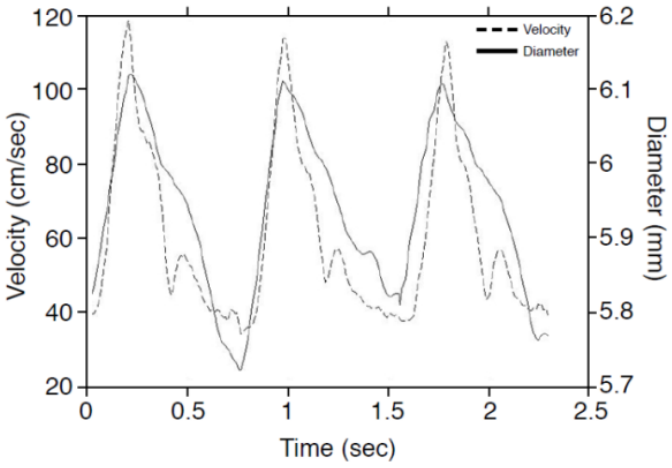

Fig. 1: Superposition of the blood flow waveform and arterial diameter changes caused by the carotid arterial pulse in a healthy male subject measured by Soleimani et al. [4].

The use of pulsed-Doppler ultrasound devices to measure blood flow and pressure waveforms has several limitations. For instance, such devices are expensive, should be used by specialists (i.e. cannot usually be operated by general practitioners), and the operation of ultrasound devices is difficult to master. In addition, since it is necessary to press the ultrasound probe against the neck to obtain images, the applied force may alter the amplitude of the pressure/flow waveforms. Inter-operator repeatability is thus another issue with contact devices. Operators may place the probes on different areas of the neck, with inconsistent levels of pressure. Achieving repeatable results generally requires clinical operators who have been specially trained and frequently use such devices [10]. A further limitation of contact devices is the discomfort of the patient as the device is pressed against the neck [11].

To address some of the limitations of pulsed-Doppler ultrasound devices, Almeida et al. [12] proposed a piezoelectric probe that could measure the carotid waveforms. The probe is directly strapped over the neck adjacent to the carotid artery to measure waveforms. This device also applies pressure to the neck that may alter the waveforms by distorting features of the waveform. Furthermore, the output waveform may be significantly affected by patient movement.

Amelard et al. [13] recently developed a non-contact imaging device for measuring the carotid artery and the jugular vein pressure waveforms. This device is a photoplethysmographic (PPG) imaging system that uses infrared light to illuminate the neck and a camera with an infrared filter. In this method, the videos taken of the subjects were post-processed to obtain pulsatile flow waveforms. Each frame was divided into 5 mm by 5 mm regions, and the pixel intensities in these regions were averaged. The changes in pixel intensities over time were used to generate a reflected illumination signal. The light absorbance was calculated from the reflected signal using the Beer-Lambert law [14], and a detrending method developed by Tarvainen et al. [15] was employed to remove environmental illumination variations. Waveforms of the absorbance over time for each region were analysed to find waveforms of pulsatile blood flow (flow with a periodic variation). It was hypothesised that pulsatile flow waveforms with a strong positive correlation ($r = 0.85 \pm 0.08$) with the finger PPG waveform were carotid arterial pulse waveforms, and waveforms that had a strong negative correlation ($r = -0.73 \pm 0.17$) with the finger PPG waveform were jugular venous pulse waveforms. For validation, after the videos were taken, ultrasound was used to spatially locate the carotid artery and jugular vein. The locations of the vessels were compared to the locations in which the strongest correlated pulsatile flows were present.

The major limitation of the approach of Amelard et al. [13] is the requirement of the additional finger PPG measurement, as it was used not only for validation, but also for comparison to the absorbance waveforms to identify if they were arterial or venous waveforms. No other methods were suggested for independent identification of the waveforms. The finger PPG signal, used regularly in clinical environments, does not contain all the information/features that are present in the carotid pulse waveform due to the peripheral nature of the finger PPG recording. For example, the reflected wave, the timing of which can change with changes in arterial stiffness, is not present in the finger PPG waveform [11].

We have designed a portable camera-based device to quantify, non-invasively, the carotid arterial waveforms, thereby addressing many of the limitations of current techniques and devices. Our method takes advantage of our precise and sensitive subpixel image registration algorithm that uses phase-based Savitzky-Golay gradient-correlation (P-SG-GC) [16]. The P-SG-GC algorithm has been previously used to measure skin deformations using only intrinsic skin surface features [17]. In this method, we process video recordings of the skin of a subject's neck, using the P-SG-GC algorithm to quantify the deformation of intrinsic skin features caused by the pulsatile flow of blood through the underlying vessels. The relative movement of the subject or the camera was corrected using a motion correction method proposed in [18] to calculate the vessel-induced deformation of skin. In this way, we quantify the skin deformation over time to produce a waveform that relates to the pressure pulse waveform of the carotid artery.

2. Method

The device consists of a Flea 3 USB3 camera (FL3-U3-13Y3M-C) to capture video recordings of the neck, a light emitting diode (LED) to provide illumination, a custom-built camera rig to hold the camera and the LED, an electrocardiogram (ECG) recording device, and a laser displacement sensor for validation of the data. The camera rig was designed using SolidWorks and constructed from poly(methyl methacrylate). Although the rig was primarily designed to maintain the position of the light source and camera throughout the recording, other factors such as ease-of-use, straightforward adjustment of camera and light source position between subjects, and portability were considered in the design.

Five healthy subjects were selected for the tests. The location of the carotid artery on subject's neck was visually detected, and videos were captured from this selected location at 90 frames per second (fps) with a resolution of 1280 pixel × 1024 pixel. The camera system was synchronised with a 3-lead chest ECG recording (9 kHz). The ECG signals and video recordings of the skin displacements of neck caused by the carotid artery were thus recorded at the same time.

The P-SG-GC algorithm [16] was used to compare each frame of the captured video to the first reference frame to determine skin deformations. Each frame was divided into subimages of 64 pixel × 64 pixel with an overlap of 49 pixel between subimages. The subimage size and comparatively large overlap between subimages enabled measurement of localised deformations of the skin caused by the carotid pulse wave. A control point was defined at the centre of each subimage, and the locations of all control points were tracked and used to determine the average displacements of the subimages between frames.

Prior to calculating the vessel-induced deformation of the skin from displacements of the control points, the relative movements of the subjects were corrected in each of the subimages using the motion correction method proposed in [18]. 128 pixel × 128 pixel subimages with an overlap of 64 pixel were selected for the motion correction algorithm. This larger subimage size and comparatively small

overlap enabled large rigid movements to be calculated while avoiding being confounded by the movement caused by the carotid pulse wave.

After correcting the motion artifacts, magnitudes of the displacements of subimages were calculated for each frame (with reference to the first frame), and were plotted over time to produce a waveform of skin deformation. A laser displacement measurement sensor (LC-2400A Keyence laser displacement meter, and LC-2440 laser displacement head) was used to validate the displacement measurements of our device. The laser displacement sensor simultaneously recorded the displacement data from the same location of the neck that was recorded by the camera in our device. The laser displacement sensor had a resolution of 0.2 μm and was placed at a distance of approximately 20 mm from each subject's neck, to measure skin displacements normal to the surface. The camera was placed at 90° to the laser sensor, so that the skin deformation could be seen in the horizontal plane. However, the bright red laser point of the displacement sensor caused intensity saturations across the region of interest (ROI) in the camera images. Since the P-SG-GC algorithm [16] estimates deformations based on the intensity values, intensity saturations reduce its accuracy. To avoid intensity saturations in the images, a green band-pass filter with a centre wavelength of 526 nm was placed on the camera and the skin was illuminated with a green LED of wavelength 525 nm.

In order to determine the similarity between laser displacement measurements and displacements calculated using our device, the two measurements were normalised, and the correlation score ($r_{x,y}$) (Pearson's correlation coefficient) was calculated between the waveforms using Equation 1 [19].

$$r_{x,y} = \frac{n(\sum x_i y_i) - (\sum x_i)\,(\sum y_i)}{\sqrt{[n\sum {x_i}^2 - (\sum x_i)^2][n\sum {y_i}^2 - (\sum y_i)^2]}} \tag{1}$$

where $r_{x,y}$ is the cross correlation score, x_i and y_i are the signal values at time-step i, and n is the number of time steps.

3. Results and discussion

Our device is shown in Fig. 2 (a) The proposed device. (b) Using the device to record the carotid artery waveforms in a subject(a). The camera rig of this device has a backboard for the subject to lie on. It has adjustable arms that allow movement of the camera to adjust for people with different neck sizes. The LED illuminates the skin on the neck of the subject, powered by a DC power supply. Subjects were sitting at an angle of 45° when imaging the carotid pulse waveforms (Fig. 2 (a) The proposed device. (b) Using the device to record the carotid artery waveforms in a subject(b)) because clinicians usually conduct normal manual examinations at this angle.

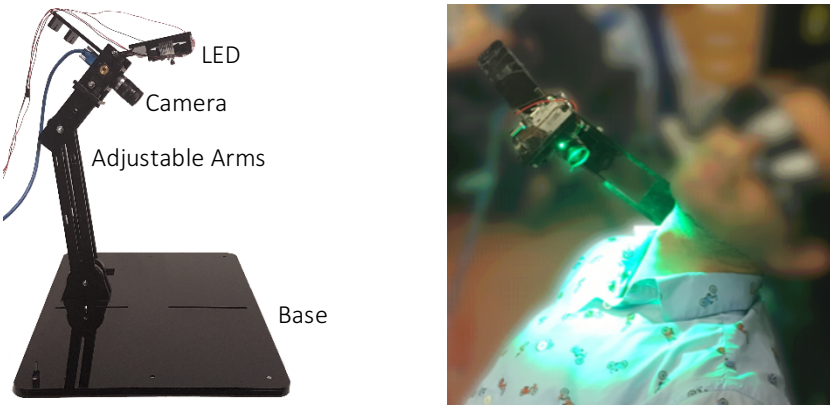

(a) (b)

Fig. 2 (a) The proposed device. (b) Using the device to record the carotid artery waveforms in a subject in a subject.

Fig. 1 illustrates the subimage size, the overlap between two subimages, and the control points of the subimages within the region of interest (ROI) of a sample captured image for measuring the carotid artery deformations in one of the subjects. As can be seen in Fig. 1, no extrinsic features were applied to the skin.

Error! Reference source not found. shows the ROI that was used for the validation of the displacement measurement of our device using the laser displacement sensor. The green band-pass filter significantly decreased the saturation effects of the laser displacement sensor in the captured images, and only a small bright point is evident from the laser. The yellow circle is the ROI selected for performing displacement measurements using the proposed device, and the small bright point is where the displacements were measured using the laser displacement measurement device.

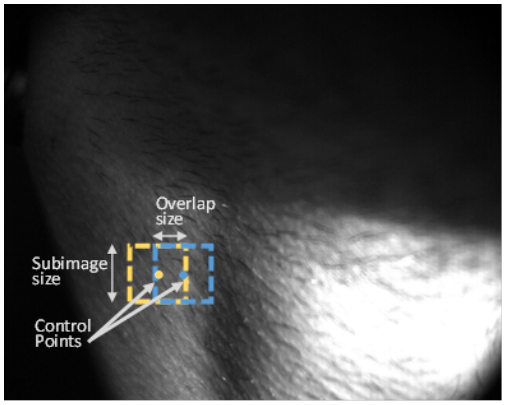

Fig. 1: The ROI of measuring the carotid artery deformations in one of the subjects. The subimage size, the overlap between two subimages, and the control points of subimages are shown on the image.

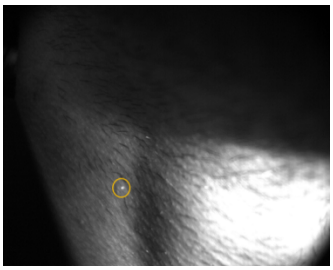

Fig. 4: The small bright spot shows the laser displacement pointer in the camera images. The green band-pass filter removed most of the saturation effects. The yellow circle is the ROI selected for performing displacement measurement using the proposed device.

A sample carotid artery waveform measured using the laser displacement measurement device, and a waveform measured using our camera-based device is illustrated in **Error! Reference source not found.**. As shown in **Error! Reference source not found.**, the two measurements were very similar. The overall correlation score (Equation 1) between the measurements of the laser measurement device and the proposed device in the five subjects of this study was $r_{xy} = 0.955 \pm 0.018$, which indicates a high degree of similarity between the displacement measurements of the proposed device and the laser measurement device.

Error! Reference source not found. shows arterial waveforms measured in one of the subjects synchronised with the ECG signal. The waveforms were compared to the ECG signal to validate that the features were occurring at the right time during the cardiac cycle. The normal shape of the carotid artery has two peaks (**Fig. 1:**), with the largest peak occurring after the QRS complex in the ECG. This was in agreement with the measurements of the proposed device for healthy subjects of this study (**Error! Reference source not found.**).

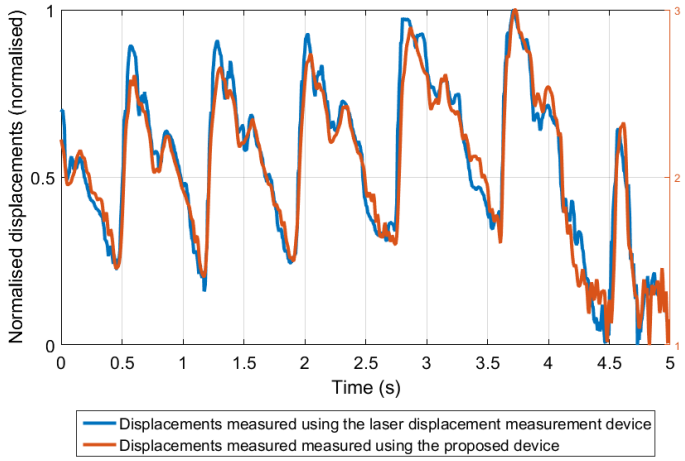

Fig. 5: One sample measured carotid artery waveforms using the device and the laser displacement measurement sensor. The overall cross-correlation score between the measurements of the laser measurement device and the proposed device in the five subjects of this study was $r_{x,y}$ = 0.9546 ± 0.0184.

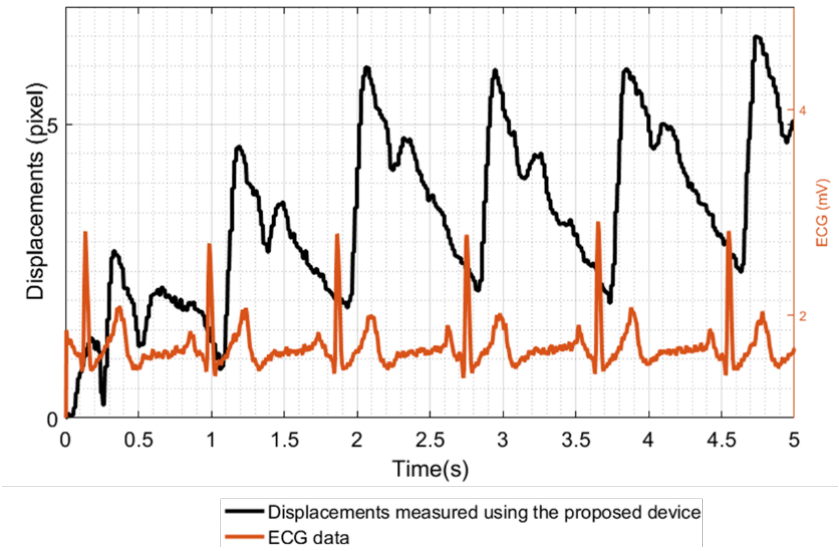

Fig. 6: One sample measured carotid artery waveforms using the device synchronised with the ECG signal.

4. Discussion and Conclusion

The current clinical methods of measuring the carotid waveforms either require invasive catheterisation or do not use an objective form of quantification. In contrast, our device is both non-invasive and non-contact, and can precisely and robustly measure the skin deformation caused directly by the pressure pulse waveforms. Since the device is non-contact, there is no force exerted on the vessels, and hence the measurements are not influenced by compression as they might be, for example, using ultrasound imaging. The displacement measurement provided by our device was tested against a laser displacement sensor with a resolution of 0.2 μm, and this resulted in a correlation score of 0.95 for five subjects. The measured waveforms of the carotid pulse were in good agreement with their expected shape in healthy subjects (**Error! Reference source not found.**).

Although the displacement waveforms show the distinct features that are present in the arterial pressure waveforms as reported in the literature, it is not possible to determine the intra-vascular pressure accurately. Such estimates would require knowledge of the mechanical properties of the surrounding tissues, such as the dermis, that lie between the epidermis and the arterial wall [11]. The displacement waveforms are also influenced by some other factors, such as the thickness of intermediate tissues of the subject in question and boundary conditions. The measured displacement vectors thus will not be identical to the pressure waveforms. Although it is unlikely that these factors alter the shape and timing of the pressure-induced skin deformation waveforms, their effects are yet to be determined.

In future work, the device will be tested for measuring jugular venous waveforms, and the relationship between the skin displacement and the internal pressure of veins and arteries will be explored. In addition, the skin displacements will be measured for patients with heart disease to investigate the sensitivity and accuracy of our device in identifying abnormalities in the pressure waveforms.

References

1. Townsend, N., Wilson, L., Bhatnagar, P., Wickramasinghe, K., Rayner, M., Nichols, M.: Cardiovascular disease in Europe: Epidemiological update 2016. Eur. Heart J. 37, 3232–3245 (2016).
2. Bickley, Lynn, A., Szilagyi., P.G.: Bates' guide to physical examination and history-taking. (2017).
3. Chutka, D.S.: A Practical Guide to Clinical Medicine. Mayo Clin. Proc. 76, 962 (2001).
4. Soleimani, E., Mokhtari-Dizaji, M., Nasser Fatouraee, A., Saberi, H.: Assessing the blood pressure waveform of the carotid artery using an ultrasound image processing method. Ultrasonography. 2, 144 (2017).
5. Veselka, J., Anavekar, N.S., Charron, P.: Hypertrophic obstructive cardiomyopathy. Lancet. 389, 1253–1267 (2017).
6. Kasper, D., Fauci, A., Hauser, S., Longo, D., Jameson, J.L., Loscalzo, J.: Harrison's Principles of Internal Medicine. McGraw Hill, New York (2015).
7. Maron, B.J.: Hypertrophic cardiomyopathy: a systematic review. JAMA. 287, 1308–1320 (2002).

8. Cheng, H.-M., Chuang, S.-Y., Wang, J.-J., Shih, Y.-T., Wang, H.-N., Huang, C.-J., Huang, J.-T., Sung, S.-H., Lakatta, E.G., Yin, F.C.P., Chou, P., Yeh, C.-J., Bai, C.-H., Pan, W.-H., Chen, C.-H.: Prognostic significance of mechanical biomarkers derived from pulse wave analysis for predicting long-term cardiovascular mortality in two population-based cohorts. Int. J. Cardiol. 215, 388–395 (2016).
9. Bonnet, B., Jourdan, F., du Cailar, G., Fesler, P.: Non invasive evaluation of left ventricular elastance according to pressure-volume curves modeling in arterial hypertension. Am. J. Physiol. - Hear. Circ. Physiol. (2017).
10. O'Rourke, M.F., Pauca, A., Jiang, X.-J.: Pulse wave analysis. Br. J. Clin. Pharmacol. 51, 507–522 (2001).
11. Casaccia, S., Sirevaag, E.J., Richter, E.J., O'Sullivan, J.A., Scalise, L., Rohrbaugh, J.W.: Features of the non-contact carotid pressure waveform: Cardiac and vascular dynamics during rebreathing. Rev. Sci. Instrum. 87, (2016).
12. Almeida, V.G., Pereira, H.C., Pereira, T., Figueiras, E., Borges, E., Cardoso, J.M.R., Correia, C.: Piezoelectric probe for pressure waveform estimation in flexible tubes and its application to the cardiovascular system. Sensors Actuators, A Phys. 169, 217–226 (2011).
13. Amelard, R., Hughson, R.L., Greaves, D.K., Pfisterer, K.J., Leung, J., Clausi, D.A., Wong, A.: Non-contact hemodynamic imaging reveals the jugular venous pulse waveform. Sci. Rep. 7, 1–10 (2017).
14. Swinehart, D.F.: The Beer-Lambert Law. J. Chem. Educ. 39, 333 (1962).
15. Tarvainen, M.P., Ranta-aho, P.O., Karjalainen, P.A.: An advanced detrending method with application to HRV analysis. IEEE Trans. Biomed. Eng. 49, 172–175 (2002).
16. HajiRassouliha, A., Taberner, A.J., Nash, M.P., Nielsen, P.M.F.: Subpixel phase-based image registration using Savitzky-Golay differentiators in gradient-correlation. under Rev. IEEE Trans. image Process.
17. HajiRassouliha, A., Taberner, A.J., Nash, M.P., Nielsen, P.M.F.: Subpixel measurement of living skin deformation using intrinsic features. Proceedings of Computational Biomechanics of Medicine XI Workshop, MICCAI (2016).
18. HajiRassouliha, A., Taberner, A.J., Nash, M.P., Nielsen, P.M.F.: Motion correction using subpixel image registration. Springer International Publishing, Cham (2017).
19. Ahlgren, P., Jarneving, B., Rousseau, R.: Requirements for a cocitation similarity measure, with special reference to Pearson's correlation coefficient. J. Am. Soc. Inf. Sci. Technol. 54, 550–560 (2003).

A Discrete Element Method for modelling cell mechanics – application to the simulation of chondrocyte behavior in the growth plate

Grand R. Joldes[1,2], George C. Bourantas[2], Adam Wittek[2], Karol Miller[2,3], David W. Smith[4], Bruce S. Gardiner[1]

[1]School of Engineering and Information Technology, Murdoch University, 90 South St, Murdoch, Australia

[2]Intelligent Systems for Medicine Laboratory, The University of Western Australia, Perth, Australia

[3]School of Engineering, Cardiff University, The Parade, CF24 3AA Cardiff, UK

[4]Engineering Computational Biology, School of Computer Science and Software Engineering, The University of Western Australia, Perth, Australia

Abstract

In this paper we describe a discrete element method (DEM) framework we have developed for modelling the mechanical behavior of cells and tissues. By using a particle method we are able to simulate mechanical phenomena involved in tissue cell biomechanics (such as extracellular matrix degradation, secretion, growth) which would be very difficult to simulate using a continuum approach.

We use the DEM framework to study chondrocyte behavior in the growth plate. Chondrocytes have an important role in the growth of long bones. They produce cartilage on one side of the growth plate, which is gradually replaced by bone. We will model some mechanical aspects of the chondrocyte behavior during two stages of this process.

The DEM framework can be extended by including other mechanical and chemical processes (such as cell division or chemical regulation). This will help us gain more insight into the complex phenomena governing bone growth.

Keywords: Discrete Element Method, chondrocyte, extracellular matrix, bone growth, growth plate

Introduction

The behavior of cells and tissues in the human body is governed by complex, interconnected physical phenomena. The mechanical behavior of cells is regulated by complicated chemical signaling pathways, with different signals either promoting or inhibiting certain cell activities [1]. Computer modelling can help us understand these complex connections and the effect of different signals on the cell and tissue behavior. A first step in this direction consists of the ability to model the mechanical behavior of cells.

From a mechanical point of view, modelling cell behavior is complicated by the multitude of phenomena and interactions that have to be taken into account, including cell growth and proliferation, secretion, degradation of the extra cellular matrix (ECM), active interaction with the ECM and cell death [1]. Such complex behavior would be very difficult to model using a continuum approach. Therefore, we have proposed to use the discrete element method (DEM), with the domain of interest (cells, ECM) is discretized using simple round particles. The behavior of cells and tissues emerges from simple interaction laws between the domain discretizing particles [2]. This allows the simulation of complex cell behavior with relatively low implementation and computation cost.

We will use the proposed DEM framework to model the behavior of chondrocytes in the epiphyseal growth plate. The chondrocytes are involved in the longitudinal growth of long bones through the endochondral ossification process, in which new cartilage is formed at one side of the epiphyseal growth plate and is gradually replaced by bone. Growth plate chondrocytes differentiate through multiple stages of this process (from a resting state through proliferative, prehypertrophic and hypertrophic stages) as the growth plate moves past. The differentiation pathway ends in cell death and the replacement of the chondrocyte generated cartilage by bone [3]. Chondrocytes synthetize the cartilage extra cellular matrix (ECM), consisting of collagen fibers and non-collagenous glycoproteins, hyaluronan and proteoglycans. The ECM defines the mechanical and physical properties of cartilage [4, 5].

In this paper we described the proposed DEM framework and use it to simulate some of the mechanics of chondrocyte behaviour in the growth plate during two of the stages of the bone growth process. In our approach, each cell (and the ECM) is modelled by a collection of particles. This allows us to control the properties and behaviour of different parts of the cell (such as the mechanical properties of cytoplasm and nucleus or the interaction properties between different parts of the cell membrane and the ECM). The simulated phenomena require the modelling of complex behaviour such as cell growth, secretion and degradation of ECM.

The paper is organized as follows: the discrete element model used is described in the next Section, followed by the results of simulating mechanical behavior of chondrocytes in the growth plate and ending with the discussion and conclusions Section.

Discrete Element Model of the Chondrocyte and ECM

Domain Discretization and the Equation of Motion

In our DEM framework the physical domain (in our case a chondrocyte and the surrounding ECM) is discretized using a set of circular particles. The macroscopic behavior of the cell and surrounding tissue is governed by simple interaction laws between neighboring particles (Figure 1). The ECM, cell membrane, cytoplasm, nucleus membrane and nucleus are all discretized using particles having different properties [2]. Furthermore, membrane particles are differentiated based on their position in order to capture the behavior of polarized cells; particles on the leading or trailing edge of the cell can have special behavior which allows the modelling of ECM degradation or hyaluronic acid production.

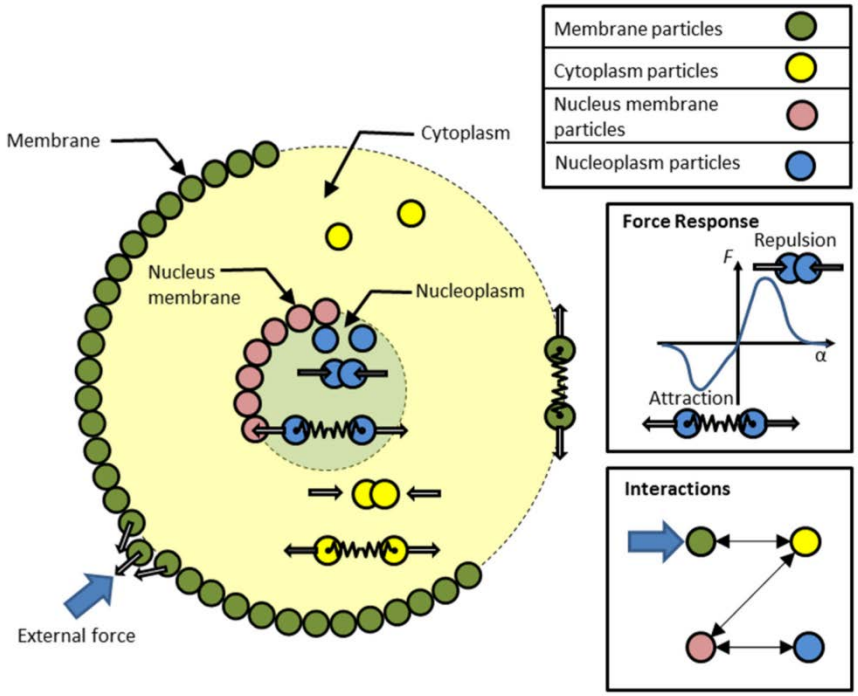

Fig. 1. The DEM model of a chondrocyte. Each cell is modelled as a collection of particles having different properties and behavior. Each particle interacts with its neighboring particles through simple interaction laws.

The mechanical behavior of each particle is governed by the interaction forces with its neighboring particles. We only consider short-range normal interaction

forces between particles, which we model as a nonlinear spring [6]. The elastic (spring) interaction force acting on particle *I* due to particle *J* is defined as:

$$\mathbf{F}_{I-J} = \left[F_I^a - P_{I-J}(\alpha_{I-J})\right]\mathbf{n}_{I-J} \tag{1}$$

where F_I^a is a constant attractive force between particles of the same type and P_{I-J} is a force dependent on the overlap/separation between particles, defined as the sum of particles' radii minus the distance between the particles' centers position:

$$\alpha_{I-J} = (R_I + R_J) - \|\mathbf{x}_I - \mathbf{x}_J\| \tag{2}$$

and $\mathbf{n}_{I-J}$ is the unit vector from the position of particles *I* towards the position of particle *J*:

$$\mathbf{n}_{I-J} = \frac{\mathbf{x}_J - \mathbf{x}_I}{\|\mathbf{x}_I - \mathbf{x}_J\|} \tag{3}$$

In the simplest form, the force P_{I-J} is chosen as a linear elastic force [6]:

$$P_{I-J}(\alpha_{I-J}) = \begin{cases} 0, & -\delta_{I-J} > \alpha_{I-J} \\ s_{I-J}R_{I-J}\alpha_{I-J}, & \alpha_{I-J} \geq -\delta_{I-J} \end{cases} \tag{4}$$

where s_{I-J} is the stiffness parameter for the spring between particles I and J and R_{I-J} is the equivalent radius.

The elastic force is zero if particle *J* is outside the interaction distance for particles *I* and *J*, $-\delta_{I-J} > \alpha_{I-J}$ (have limited range). More complicated interactions can be included, such as non-linear normal forces, tangential forces and torques, in order to capture complex macroscopic material behavior [6]; however, given the already large variability in tissue properties and the uncertainty in determining mechanical parameters, we have not included such forces.

The equivalent radius appearing in eq. (4) is computed based on the individual radii of the two particles, and is included for scaling the response with the size of the particles:

$$R_{I-J} = \frac{R_I R_J}{R_I + R_J} \tag{5}$$

The total force acting on particle *I* due to its neighbouring particles is obtained by summing the influences of all surrounding particles:

$$\mathbf{F}_I = \sum_{J \neq I} \mathbf{F}_{I-J} \tag{6}$$

Because only short range interactions are considered, the summation in eq. (6) has non-zero terms only for n_I neighbouring particles, as resulting from eq. (4). We will name this set of neighbouring particles N_I.

The motion of particle *I* is governed by Newtonian physics [6]:

$$m_I \ddot{\mathbf{x}}_I = \sum_{J \in N_I} \mathbf{F}_{I-J} + \mathbf{F}_I^E \tag{7}$$

with the externally applied force $\mathbf{F}_I^E$ including any other forces other than particle interactions (such as gravity).

Given the very slow evolution of the growth plate, we can consider the chondrocyte behavior a very slowly evolving phenomena; therefore, the viscous interaction forces are ignored and do not appear in the above equation of motion. For the same reason, the inertial forces can also be ignored, and the mechanical system can be considered in a quasi-static equilibrium at any point in time.

Quasi-static Solution Method

The quasi-static equilibrium equation obtained by ignoring the inertial term from eq. (7) requires the solution of a very large (and possible non-linear) system of equations at each time step. We propose to use an explicit solution method, based on the addition of artificial transients to eq. (7) (dynamic relaxation), to reach the steady state solution, as described in the following sections. Such solution method allows the equations in the system of equations (7) to be decoupled and solved individually at each time step, being well suited for parallel implementation. We adopted the following procedure, inspired from the finite element [7, 8] and meshless [9, 10] methods, consisting of the inclusion of a mass proportional damping term in the equation of motion (7):

$$m_I \ddot{\mathbf{x}}_I + c \cdot m_I \dot{\mathbf{x}}_I = \sum_{J \in N_I} \mathbf{F}_{I-J} + \mathbf{F}_I^E \tag{8}$$

where c is the damping coefficient.

The fastest convergence is obtained [7] when the damping parameter and time step values are:

$$c \approx 2\sqrt{A_0} = 2\omega_0, \tag{9}$$

$$\Delta t \approx 2/\sqrt{A_m} = 2/\omega_{max}, \tag{10}$$

where A_0 and A_m are the minimum and maximum eigenvalues of matrix $\mathbf{A}=\mathbf{M}^{-1}\mathbf{K}$, $\mathbf{K}$ being the stiffness matrix and $\mathbf{M}$ the mass matrix of the structure (therefore, ω_0 and ω_{max} are the lowest and highest circular frequencies of the un-damped equation of motion). Given that the assembly of particles is equivalent to an assembly of bar elements, a similar procedure to the one described in [7] is used to allocate mass to each particle, which promotes fast convergence to the steady state and guarantees stability of the explicit time integration procedure.

Neighbor Search Algorithm

The computation of interactions between the particles involved in a simulation requires the neighbors of each particle to be identified at each time step. In explicit dynamic simulation this process becomes a major computational bottleneck; it is therefore important that the neighbor search algorithm is highly optimized [11].

To optimize the bin search algorithm, we perform the discretization using only similar sized particles. We then adopt a binning algorithm, which partitions the

problem domain into equally sized bins, with the size of the bins selected in such a way that the neighbors of a given particles can be found in the bin containing the particle or in the neighboring bins. Once the particles are distributed into bins, their neighbors can be easily found by looking in the neighboring bins. The restriction on the particle size ensures that only a small number of particles are included in each bin. This algorithm has O(*N*) complexity, therefore its computation time increases linearly with the number of particles.

Modelling of Special Cell-ECM Interactions

To complete the modelling of chondrocyte migration through ECM, there are several special interactions which need to be considered apart from the simple particle to particle forces. These include: a membrane model which ensures cell integrity and prevents seepage of cell particles outside the cell [12], modelling ECM degradation by the chondrocyte and modelling secretions by the chondrocytes.

We implemented the membrane behavior by including constant attractive forces between the membrane particles, to create a constant tension in the membrane. Also, each membrane particle is aware of its neighboring membrane particles and does not interact with other particles of the same membrane, in order to avoid membrane folding onto itself. If a membrane particle is displaced from the central position between its neighbors, an elastic restoring force is applied to it. This is required in order to maintain the relative positions of the membrane particles.

ECM degradation by the chondrocyte has been implemented by introducing an integrity measure for each of the ECM particles. When an ECM particle *I* comes into contact with a membrane particle *J* located on the leading edge of the chondrocyte, its integrity is reduced by a constant value (degradation factor, *D*) multiplied by the particle penetration (as a measure of the contact surface) at each time step:

$$\mathrm{I}_I^{\,t+1} = \mathrm{I}_I^{\,t} - D\alpha_{I-J}, \quad \alpha_{I-J} > 0 \tag{11}$$

When the integrity of a particle becomes negative the particle is removed from the simulation.

The forces between particles are modified by introducing the integrity measure above as:

$$\bar{P}_{I-J} = \mathrm{I}_I \mathrm{I}_J P_{I-J} \tag{12}$$

The secretions generated by the chondrocyte are modelled by increasing the size of any ECM particle *I* which come into contact with a membrane particle *J* located on the secreting part of the membrane. The size increase is generated by multiplying the radius of the ECM particles by a constant growth factor $G > 1$ at each time step:

$$R_I^{\,t+1} = GR_I^{\,t}, \quad \alpha_{I-J} > 0 \tag{13}$$

Cell growth is modelled in a similar manner, using pre-defined growth factors for cytoplasm and nucleus particles. When the radius of the particle becomes

higher than the maximum radius used in the simulation (imposed due to the neighbor search algorithm, which is optimized for same size particles), the particle is split into 3 equally sized particles (in 2D), whose radius is selected so that the occupied area is preserved.

Simulation of Chondrocytes in the Growth Plate

Chondrocytes in the growth plate undergo a differentiation cascade which drives the longitudinal growth of the skeletal elements through chondrocyte proliferation, cellular enlargements via hypertrophy, ECM synthesis and controlled matrix degradation [5]. The growth plate is organized into layers of resting, proliferative and hypertrophic chondrocytes. In the resting layer the chondrocytes are round and rarely divide. In the proliferative zone, the cells undergo rapid division, are flattened along the mediolateral axis, and form columns along the proximodistal axis of the long bones. Chondrocytes end their cycle at the proximal end of the column and increase their volume to become hypertrophic before the zone is calcified and replaced by trabecular bone [5].

Chondrocytes are surrounded by a thin pericellular matrix (PCM), which is enveloped by the territorial matrix (TM). The ECM around the columns is called the inter-territorial matrix (ITM) and fills up the longitudinal septum between the chondrocyte clusters. One column in the proliferative zone usually consists of several flattened chondrocytes surrounded by different matrix compartments. The PCM and TM together with the clustered chondrocytes define the columnar chondron, the functional unit of the cartilage [1], which is considered to play an important role in regulating the interactions between chondrocytes and their surrounding matrix. Investigations of the elastic properties of the proliferative zone of the murine growth plate by atomic force microscopy (AFM) have indicated that ITM has an approximately two times higher stiffness compared to TM/PCM [5].

During its life cycle, the growth plate chondrocyte secrets different molecules, ranging from randomly oriented type II collagen and hydrophilic proteoglycans in the proliferative zone to metalloproteinases (MMPs), which participate in the reabsorption of the ECM, in the hypertrophic zone [13]. We are going to use our DEM framework to study the effect of aggrecan secretion on the shape of the chondrocytes in the proliferative zone and chondrocyte enlargement, combined with ECM degradation by MMPs, in the hypertrophic zone. The particle interactions used in the simulation are described in Table 1, with the parameter values given in Table 2. The boundary conditions consisted of fixed ECM particles on the edges of the problem domain. We consider the cell to be polarized, with the secretion/ECM degradation only happening on an active portion of the cell membrane. We investigated the influence of nucleus stiffness on the cell flattening by running a simulation with the nucleus having the same stiffness as the cytoplasm.

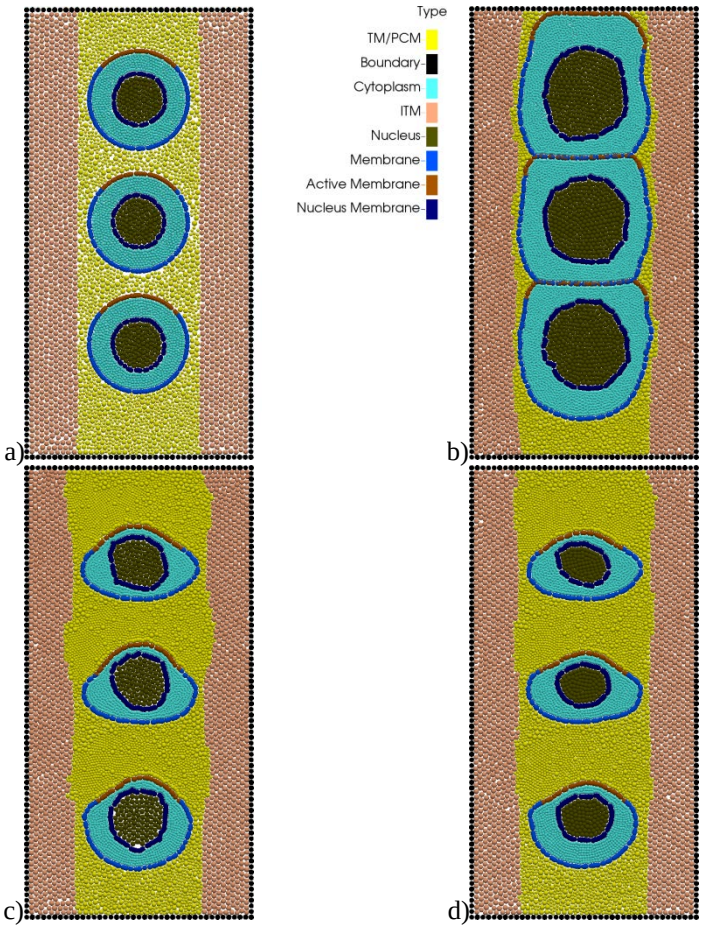

Fig. 2. Results of simulating mechanical behavior of chondrocytes in the growth plate. a) Initial configuration (7121 particles); b) Results for chondrocyte enlargement in the hypertrophic zone, with ECM degradation by MMPs at the active edge (22068 particles); c) Results for aggrecan secretion in the proliferative zone, nucleus 2.5 times stiffer than cytoplasm (16304 particles); d) Results for aggrecan secretion in the proliferative zone, nucleus same stiffness as cytoplasm (14941 particles).

Table 1. Particle types and interactions used in the simulation (the table is symmetrical).

Particle Type	T	I	C	N	M	NM	AM
TM/PCM (T)	P_T						
ITM (I)	P_{TI}	P_I					
Cytoplasm (C)			P_C				
Nucleus (N)				P_N			
Membrane (M)	P_{TM}	P_{IM}	P_{CM}		F_M^a, P_M		
Nucleus membrane (NM)			P_{CNM}	P_{NNM}		F_{NM}^a, P_{NM}	
Active membrane (AM)	D, G, P_{TM}	P_{IM}	P_{CM}		F_M^a, P_M		F_M^a, P_M

Because this simulation belongs to a class of problems where deformation is only driven by displacements [14], the simulation results do not depend on the actual stiffness defining the elastic forces between different particles; we only have to estimate the ratios between the stiffness of different types of tissues. Therefore we considered the nucleus to be 2.5 times stiffer than the cytoplasm [2] and the ITM 2 times stiffer than the TM/PCM [5]. Elastic forces between membrane particles were chosen to prevent particle seepage through the membrane [12]. The simulation results are presented in Figure 2.

Table 2. Simulation parameters

Simulation parameters	**Parameter Values**
Domain size	40um x 80 um
Chondrocyte radius	10 um
Particle radius	0.30 – 0.52 um
Number of time steps	2000
Elastic force between TM/PCM particles P_T	s_T =0.5; $\delta_T = 0.01$
Elastic force between ITM particles P_I	s_I =1; $\delta_I = 0.01$
Elastic force between cytoplasm particles P_C	$s_C = 0.2$; $\delta_C = 0.01$
Elastic force between nucleus particles P_N	$s_N = 0.5$; $\delta_N = 0.01$
Elastic force between membrane particles P_M	$s_M = 5$; $\delta_M = 0$
Constant force between membrane particles F_M^a	0.05
Elastic force between membrane particles P_{NM}	$s_{NM} = 0.5$; $\delta_{NM} = 0$
Constant force between membrane particles F_{NM}^a	0.02
Elastic force between T,I, C and membrane P_{XM}	$s_{XM} = 1$; $\delta_{XM} = 0.01$
Elastic force between C, N and NM P_{XNM}	$s_{XNM} = 0.5$; $\delta_{XNM} = 0.01$
Elastic force between TM/PCM and ITM P_{TI}	$s_{TI} = 2$; $\delta_{TI} = 0$
Degradation factor D	0.05
Growth factor G	1.005

Discussion and Conclusions

This paper presents a discrete element method for modelling cell and tissue mechanics. By adopting a discrete element modelling framework we are able to simulate complex mechanical phenomena, including large cell deformations, ECM degradation, cell growth and cell secretions; such simulations would be very difficult to perform using continuum based simulation methods. The discrete element method facilitates easy particle insertion and removal, which is needed in simulating some of these phenomena.

We apply the proposed DEM framework to the modelling of chondrocyte behavior during its different life stages in the growth plate. We modelled the secretion of ECM components in the proliferative zone and the chondrocyte enlarge-

ment in the hypertrophic zone combined with ECM degradation by MMPs on part of the cell's membrane. The simulation produced the expected cell behavior, resulting in some flattening of the chondrocytes in the proliferative zone and in large and square-like shaped chondrocytes in the hypertrophic zone.

The cell flattening in the proliferative zone could not be completely explained by the cell secretion alone, especially for high cell aspect ratios. This may be due to complex interactions between the chondrocyte, its pericellular microenvironment and the load bearing extracellular matrix [15]; this includes vectorial production and resorption of ECM around the chondrocytes as well as rapid cell division and reorientation [1], processes that are not captured by our current model.

The simulations took approximatively 69 s for the chondrocyte enlargement in the hypertrophic zone and 44 s for the secretion in the proliferative zone on a PC having an Intel Core i7-5930K @ 3.5 GHz processor and running Windows 8, using a single threaded implementation of the explicit integration algorithm. Given its explicit nature, the algorithm is very well suited for parallel implementation on Graphics Processing Units (GPU); we expect a large speed improvement for such an implementation, based on our previous experience with explicit finite element codes [16].

The DEM framework can be extended by including other mechanical and chemical processes (such as cell division and cell activity regulation). The possibility to couple mechanical and chemical interactions happening in the growth plate will help us gain more insight into the complex phenomena governing bone growth.

Acknowledgments

This research was supported partially by the Australian Government through the Australian Research Council's Discovery Projects funding scheme (project DP160100714). The views expressed herein are those of the authors and are not necessarily those of the Australian Government or Australian Research Council. We wish to acknowledge the Raine Medical Research Foundation for funding G. R. Joldes through a Raine Priming Grant, and the Department of Health, Western Australia, for funding G. R. Joldes through a Merit Award.

Bibliography

1. Hunziker, E.B., *Mechanism of longitudinal bone growth and its regulation by growth plate chondrocytes.* Microscopy Research and Technique, 1994. **28**(6): 505-519.
2. Gardiner, B.S., et al., *Discrete element framework for modelling extracellular matrix, deformable cells and subcellular components.* PLoS Computational Biology, 2015: DOI: 10.1371/journal.pcbi.1004544.
3. Alman, B.A., *The role of hedgehog signalling in skeletal health and disease.* Nat Rev Rheumatol, 2015. **11**(9): 552-560.

4. Gentili, C. and R. Cancedda, *Cartilage and bone extracellular matrix.* Current Pharmaceutical Design, 2009. **15**(12): 1334-48.
5. Prein, C., et al., *Structural and mechanical properties of the proliferative zone of the developing murine growth plate cartilage assessed by atomic force microscopy.* Matrix Biology, 2016. **50**: 1-15.
6. Luding, S., *Introduction to discrete element methods.* European Journal of Environmental and Civil Engineering, 2008. **12**(7-8): 785-826.
7. Joldes, G.R., A. Wittek, and K. Miller, *Computation of intra-operative brain shift using dynamic relaxation.* Computer Methods in Applied Mechanics and Engineering, 2009. **198**(41-44): 3313-3320.
8. Joldes, G.R., A. Wittek, and K. Miller, *An adaptive Dynamic Relaxation method for solving nonlinear finite element problems. Application to brain shift estimation.* International Journal for Numerical Methods in Biomedical Engineering, 2011. **27**(2): 173-185.
9. Horton, A., et al., *A Meshless Total Lagrangian Explicit Dynamics Algorithm for Surgical Simulation.* International Journal for Numerical Methods in Biomedical Engineering, 2010. **26**(8): 977-998.
10. Joldes, G.R., A. Wittek, and K. Miller, *Stable time step estimates for mesh-free particle methods.* International Journal for Numerical Methods in Engineering, 2012. **91**(4): 450-456.
11. Williams, J.R., E. Perkins, and B. Cook, *A contact algorithm for partitioning N arbitrary sized objects.* Engineering Computations, 2004. **21**(2/3/4): 235-248.
12. Gardiner, B.S., et al., *Controlling seepage in discrete particle simulations of biological systems.* Computer Methods in Biomechanics and Biomedical Engineering, 2016. **19**(10): 1160–1170.
13. Blair, H.C., M. Zaidi, and P.H. Schlesinger, *Mechanisms balancing skeletal matrix synthesis and degradation.* Biochemical Journal, 2002. **364**(Pt 2): 329-341.
14. Miller, K. and J. Lu, *On the prospect of patient-specific biomechanics without patient-specific properties of tissues.* Journal of the Mechanical Behavior of Biomedical Materials, 2013. **27**: 154–166.
15. Poole, C.A., S. Ayad, and R.T. Gilbert, *Chondrons from articular cartilage. V. Immunohistochemical evaluation of type VI collagen organisation in isolated chondrons by light, confocal and electron microscopy.* Journal of Cell Science, 1992. **103**(4): 1101-1110.
16. Joldes, G.R., A. Wittek, and K. Miller, *Real-Time Nonlinear Finite Element Computations on GPU - Application to Neurosurgical Simulation.* Computer Methods in Applied Mechanics and Engineering, 2010. **199**(49-52): 3305-3314.

Image-based biomechanical modelling of heart failure

Martyn Nash

Auckland Bioengineering Institute, University of Auckland,
70 Symonds Street, Auckland 1010, New Zealand

Abstract

Effective diagnosis and treatment of cardiovascular disease is hampered by a lack of knowledge of the underlying pathophysiological mechanisms on a patient-specific basis. Biomechanical factors, such as intrinsic myocardial stiffness and tissue stress, are known to have important influences on heart function, but these factors cannot be measured directly. Mathematical modelling provides a rational integrative basis for interpreting the rich variety of physiological data that are available in the laboratory and clinical settings. This seminar will discuss how image-based, individualised biomechanical models of the heart can be used to characterise the relative roles of anatomical, microstructural and functional remodelling in heart failure. Methods and examples from pre-clinical and clinical studies will be presented to demonstrate this approach. Individualised mathematical models of this kind can to help to more specifically stratify the different forms of heart pathology, and thus have the potential to inform patient therapy and management of care.

A comparison of biomechanical models for MRI to digital breast tomosynthesis 3D registration

P. Cotič Smole[1,3], C. Kaiser[2,3], J. Krammer[2,3], N.V. Ruiter[1], T. Hopp[1,3]

[1] Karlsruhe Institute of Technology, Institute for Data Processing and Electronics Karlsruhe, Germany
[2] University Medical Centre Mannheim, Medical Faculty Mannheim, University of Heidelberg, Institute of Clinical Radiology and Nuclear Medicine Mannheim, Germany
[3] HEiKA – Heidelberg Karlsruhe Research Partnership, Heidelberg University, Karlsruhe Institute of Technology (KIT)
patricia.smole@kit.edu
torsten.hopp@kit.edu

Abstract. Increasing interest in multimodal breast cancer diagnosis has led to the development of methods for MRI to X-ray mammography registration. The severe breast deformation in X-ray mammography is often tackled by biomechanical models, yet there is no common consensus in literature about the required complexity of the deformation model and the simulation strategy. We present for the first time an automated patient-specific biomechanical model based image registration of MRI to digital breast tomosynthesis (DBT). DBT provides three-dimensional information of the compressed breast and as such drives the registration by a volume similarity metric. We compare different simulation strategies and propose a patient-specific optimization of simulation and model parameters. The average three-dimensional breast overlap measured by Dice coefficient of DBT and registered MRI improves for four analysed subjects by including the estimation of unloaded state, simulation of gravity and a concentrated pull force that mimics manual positioning of the breast on the plates from 88.1 % for a mere compression simulation to 93.1 % when including all our proposed simulation steps, whereas additional parameter optimisation further increased the value to 94.4 %.

Keywords: Breast image registration, Biomechanical model, Magnetic Resonance Imaging, Digital Breast Tomosynthesis

1 Introduction

Medical imaging is essential for early breast cancer diagnosis. Due to several screening programs around the world, X-ray mammography became the current standard method [1], while additional imaging by e.g. magnetic resonance imaging (MRI) is frequently used in case of suspicious findings. An increasing interest in multimodal diagnosis [2] has led to the development of image registration methods to enable intuitive spatial correlation of three-dimensional MRI

volumes and two-dimensional X-ray mammograms. Such a registration poses a challenge as nonlinear deformations that occur when the breast is subject to mammographic compression can only be depicted in a 2D projection image.

Several approaches including affine transformations [3], spline transformations [4] and biomechanical models [5–8] have been presented to predict the deformation of the breast. The complexity of biomechanical models used vary from simplified geometries [9], homogeneous material [5], more complex patient-specific models with respect to inner structures [6, 8] and advanced boundary conditions [7]. The necessary complexity of a biomechanical model and simulation strategies to derive realistic deformations of a compressed breast is still an unsolved problem.

To obtain a deeper understanding of the complex compression deformation process, we apply for the first time a registration of MRI to X-ray digital breast tomosynthesis (DBT) volumes. DBT [10] is an emerging technology that provides three-dimensional information of the breast anatomy in the compressed state same as in X-ray mammography. As the modality is still paving the path into clinical practice, there is not yet evidence in the literature that co-location of lesion in DBT and MRI could improve the diagnosis of breast cancer. However, due to the three-dimensional information that DBT introduces compared to mammography it has the potential to even improve the diagnosis of breast cancer reached for multimodal MRI and mammography [11]. We extend our automated patient-specific biomechanical model generation method by additionally including the simulation of gravity for a standing patient after the estimation of the unloaded state. Furthermore, we adapt the compression simulation by introducing a concentrated pull force of adjustable size that mimics the manual positioning of the breast on the compression plate by the radiologist assistant. We propose a patient-specific optimization of the model and simulation parameters and present preliminary registration results with in-vivo data.

2 Methods

The aim of the registration is to bring the breast shape in the MRI into a configuration which is comparable to the shape in DBT. The MRI images are warped using the deformation field obtained from a biomechanical simulation of the breast deformation during DBT acquisition. An overview of the whole registration process is shown in Figure 1.

2.1 Automated biomechanical model generation

To obtain the patient-specific breast geometry, the MR volume is segmented into background, fatty tissue, glandular tissue and breast muscle. We first separate the breast from the background using a two-class Fuzzy-C-means clustering (FCM). Afterwards the MR volume is divided at the sternum into a dorsal and ventral part. In the ventral part fatty and glandular tissue are segmented by a two-class FCM similar to [12], while in the dorsal part, a three-class FCM

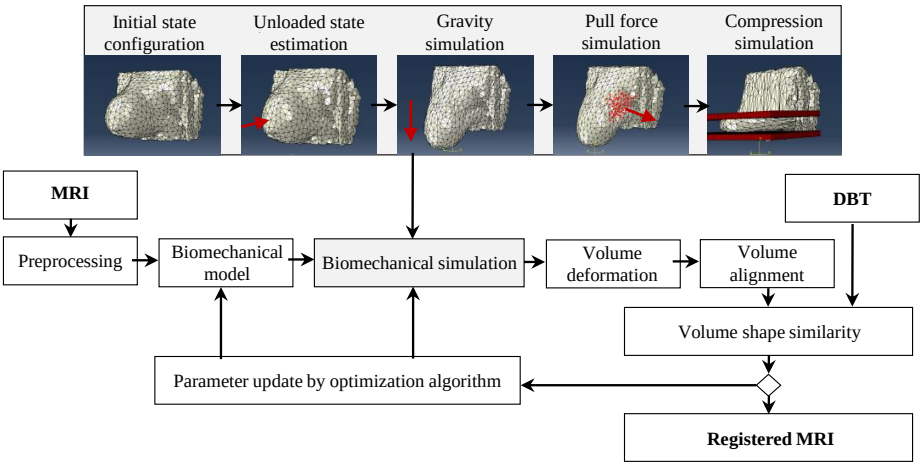

Fig. 1: Overview of the registration process including preprocessing, model generation, different simulation strategies, post-processing and parameter optimization. The inset figures present the breast shape after successive simulation stages, where the red arrow marks the loading direction.

is applied. To correct for outliers due to MRI field inhomogeneities, the breast muscle is detected slicewise by thresholding the directional gradient of the image after applying an anisotropic diffusion filter. Ventral and dorsal segmentations are combined and the tissue classes with maximum likelihood are used as final segmentation. According to the segmented tissue type, voxels are assigned tissue-specific material properties [13].

To create the model geometry, a tetrahedral meshing algorithm [14] based on Delaunay triangulation converts the segmented MRI volume into approximately 9000-11000 4-node elements depending on the breast volume. At tissue interfaces, the algorithm is allowed to increase the density of the mesh to better reflect the physical breast. Though the limited number of elements may not accurately reflect tissue interfaces, this tradeoff was made to reduce the computational expense. A layer of membrane elements with a thickness of 2.5 mm is added on top of breast surface elements to model skin. The thickness selection was supported by our initial tests, which revealed an increase in the registration accuracy with increased skin thickness and a convergence reached at around 2.5 mm. Nodes at the back of the model are fixed in all directions as suspension at the chest. For the compression simulation, acrylic glass plates consisting of 8-node hexahedrons are added to the model. A small-sliding interface with adjustable friction between plate and breast surface is defined.

An isotropic hyperelastic neo-hookean material model [15] is implemented. The isotropic material deforms uniformly in all directions of space and is defined by two material constants C_{01} and D_1, which are determined by the Young's modulus E and the Poisson ratio ν as $C_{01}=\frac{E}{4(1+\nu)}$ and $D_1=\frac{2}{3E(1-2\nu)}$. A constant

ν of 0.495, which is within the range used in literature (e.g. [6]), is applied to model nearly incompressible material.

Biomechanical simulations are formulated with the Finite Element Method (FEM) and computed using the dynamic FE solver for large deformations of the software package ABAQUS [16] in a quasi-static configuration. The following simulation strategies are used:

(1) DBT compression simulation.
(2) The estimation of the unloaded state and DBT compression simulation.
(3) The estimation of the unloaded state, simulation of gravity for a standing patient and DBT compression simulation.
(4) The estimation of the unloaded state, simulation of gravity for a standing patient and DBT compression simulation with the concentrated pull force effect.
(5) The estimation of the unloaded state, simulation of gravity for a standing patient, DBT compression simulation with the concentrated pull force effect and parameter optimization.

The estimation of the unloaded state follows an inversion of the gravity by applying a body load with an acceleration of $g = 9.81\,\mathrm{m/s^2}$ in dorsal direction due to its computational benefit and comparable accuracy with more complex methods. However, it is worth noticing that this approach has shown to introduce errors compared to more sophisticated inversion techniques when biomechanical models of larger breast are considered [17]. Although our initial tests derived comparable results when using both body load application and the iterative approach, we plan to further investigate both approaches. Similarly to the esetimation of unloaded state, the gravity for a standing patient is estimated by applying a gravitational body load in caudal direction. To simulate the DBT compression, the lower plate is first moved to the position where the inferior breast reaches its maximal coordinate in cranial-caudal direction, which is followed by a movement of the upper plate to the distance expressing the compression thickness initially given by the DBT's meta data. The concentrated pull force that is introduced in the compression simulation step is designed to account for manual positioning of the breast on the compression plate. The force acts on a set of lateral nodes of the model within 40 % of the breast size with ventral-lateral direction (Fig. 1). The initial force magnitude is set to $F = 0.05\,\mathrm{N}$ as the first test simulations delivered an enhanced registration accuracy at this value for all datasets. After the FEM simulation, the deformation is applied to the MRI volume by linear interpolation of the deformation within the 4-node tetrahedrons and tri-linear interpolation of intensity values [18]. Finally, the MRI and DBT volumes are aligned at their centres of mass.

To allow for comparison of the results, the tissue material parameters are applied constant for all patients in the first four analysed simulation configurations. The initial Young's moduli are in the range of values obtained in our previous studies [19]: $E_{fat} = 1200\,\mathrm{Pa}$, $E_{gland} = 2500\,\mathrm{Pa}$ and $E_{muscle} = 5000\,\mathrm{Pa}$.

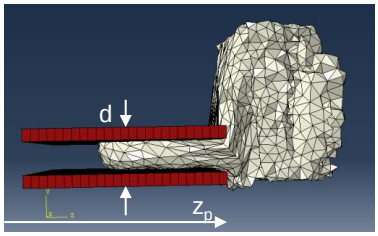

Fig. 2: Schematic presentation of the compression thickness (d) and plate position in ventral-dorsal direction (z_p).

2.2 Patient-specific optimization

To adapt the image registration to patient-specific conditions and overcome uncertainties in image acquisition, the fifth simulation configuration incorporates optimisation of the most influencing parameters using particle swarm [20]. A maximum number of iterations of 100 is used as a stopping condition. For the optimization criterion, we used the Dice coefficient (Dice) [21], which expresses the overlap of the DBT breast volume and the registered deformed MRI breast volume and is used to estimate the three-dimensional shape similarity. Among the material parameters, Young's moduli of fat (E_{fat}), glandular (E_{gland}) and muscle (E_{muscle}) tissue are optimised. Additionally, the concentrated pull force magnitude F, compression thickness (d) and plate position in ventral-dorsal direction (z_p) are set as degrees of freedom along with the rotations of the mesh in all three directions of space. A schematic presentation of compression thickness and plate position in ventral-dorsal direction is given in Figure 2. The compression thickness is allowed to slightly deviate from its initial value given in the image metadata to allow for uncertainties in the exact detector position. A rotation around the ventral-dorsal axis (rot_z) is applied to compensate for uncertainties in the measured tomosynthesis projection angle from the imaging system and manual positioning of the breast on the compression plate. A rotation around the caudal-cranio axis (rot_y) is introduced to meet the tomosynthesis guidelines, which suggest a tilting of the patient by approximately 5° to the not imaged side [22]. Additionally, the mesh can be rotated around the left-right axis (rot_x) to account for patient tilting in DBT acquisition.

2.3 Evaluation method

For evaluation of the registration accuracy, four clinical routine examinations were used, each consisting of a T1-weighted MRI volume and a corresponding cranio-caudal (CC) DBT volume with one lesion clearly detected in both modalities. The lesions that were used as landmarks were manually annotated in the unregistered MRI and DBT volumes using a freehand tool in 3D. The lesions serve as ground truth for calculating the target registration error (TRE) given by the three-dimensional Euclidean distance between the DBT lesion centre

and MRI lesion centre after deformation simulation and alignment. Additionally Dice, which also acts as the optimization criterion, is used to estimate the breast overlap enhancement between different registration strategies.

3 Results

The evaluation results of registration approaches with different simulation strategies are depicted in Figure 3. To provide an indication of the magnitude of registration error in the absence of the biomechanical modelling, the results obtained for mere volume alignment are added to Figure 3. With the application of biomechanical modelling before volume alignment, the average Dice across datasets increase for more than a factor 2 compared to mere volume alignment. The increment between two successive simulation strategies is relatively consistent across datasets as its standard deviation is kept below 1 % for all successive strategy pairs. The estimation of the unloaded state increases the average Dice across datasets by 4 %, whereas by also simulating gravity the additional increment is in average around 0.5 %. Both incorporation of the pull force into the simulation and the parameter optimization using particle swarm give an additional gain of more than 1 % each, which delivers a resulting average Dice of 94.4 % compared to 88.1 % for a mere DBT compression simulation and 41.5 % for a mere volume alignment.

Contrary to Dice, TRE does not exhibit a consistent behaviour across datasets for different simulation strategies. This could arise both due to different lesion positions in the breast, as well as variable lesion size. In datasets 2 and 4, where TRE increased with simulation complexity, the lesion was located further away from the chest wall that in datasets 1 and 3. This indicates that the proposed simulation strategies may better mimic the physical deformation of lesions close to the chest wall. Moreover, in datasets 2 and 4 the lesion diameter was far larger than 1 cm, which also poses a limitation on the accuracy of the generated model since the lesion was treated as glandular tissue. Furthermore, in the case of large lesions, also the centre positions of the annotated lesion volume could deviate considerably between MRI and DBT. Although one would assume that the mapping of the deformation field may be more accurate for lesions close to the chest wall, a lesion close to the chest wall did not guarantee a small registration error (see dataset 3). This could be overcome by introducing even more complex biomechanical models and optimization criteria relying on texture features. Furthermore, we plan to assess the registration accuracy with additional landmarks such as the nipple position and fat/fibroglandural tissue features.

A comparison of the accuracy in estimating the volume shape with different registration approaches is shown in Figure 4 for dataset 1. Consistently with Figure 3, it is clearly seen that biomechanical modelling greatly contributes to better volume shape agreement than mere volume alignment. Moreover, the overlap between volumes increases considerably by optimizing the pull force magnitude (see xz plane).

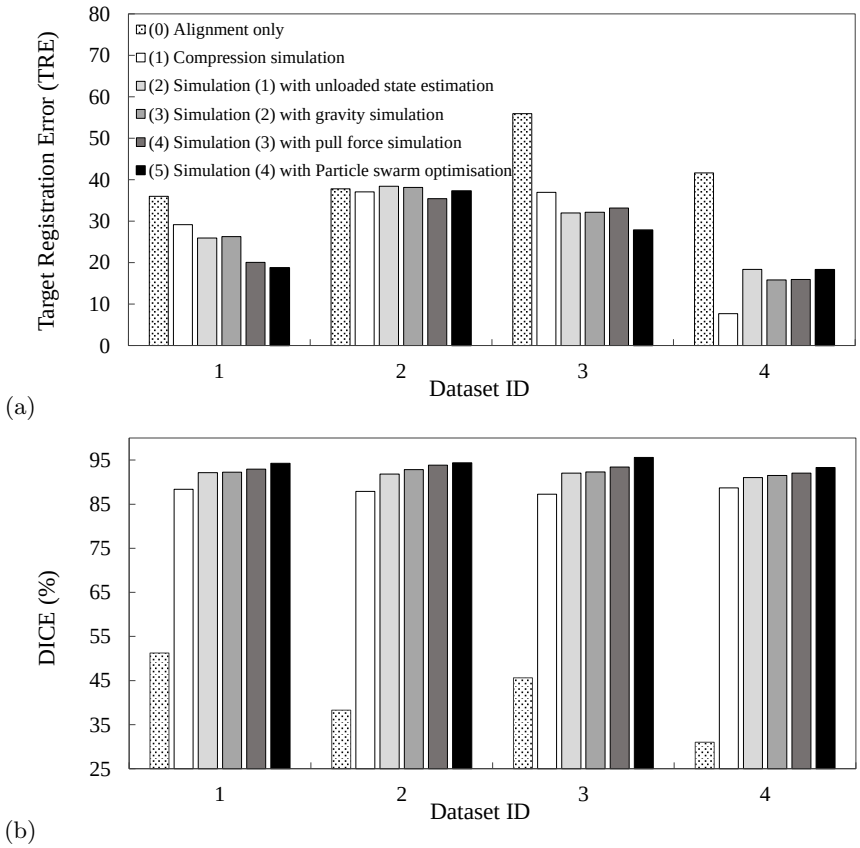

Fig. 3: a) Target registration error (TRE) and b) Dice coefficient per dataset for registration approaches (1)–(5). Input (0) refers to registration results obtained after mere volume alignment.

The average computation times across datasets and their standard deviation for different simulation stages, as well as for the complete pipeline are depicted in Table 1. By including all the proposed simulation stages, the computation time is approximately doubled compared to mere compression simulation. The estimation of unloaded state and gravity simulation require similar times, whereas the application of pull force only slightly increases the overall computation time as it is applied during compression simulation. Among all simulation stages, the compression simulation shows to be the most computationally expensive part of the biomechanical simulation. By compressing both plates simultaneously, the average compression time could be reduced to 50 s, but resulted in decreased volume overlap for about 0.5 %. The biomechanical simulation takes on average about 1/3 of the time for the complete pipeline, whereas 1/2 of the time is spent for the MRI volume segmentation.

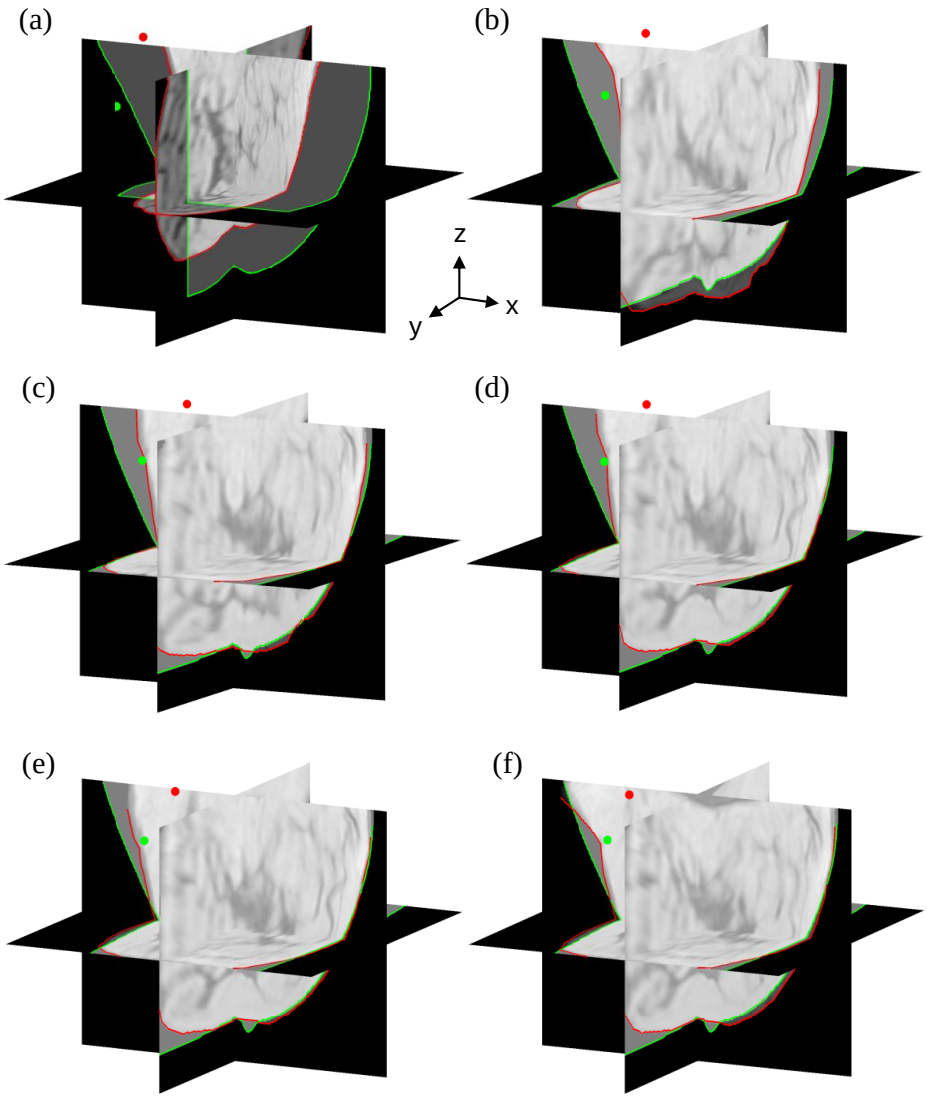

Fig. 4: Comparison of the accuracy of different approaches for the registration of deformed MRI volume with DBT volume for dataset 1 with marked surface border of both volumes. The green dot depicts the lesion annotation in the DBT volume, the red dot the lesion annotation in the deformed MRI volume. a) With volume alignment only b) DBT compression simulation, c) as (b) with additional unloaded state estimation, d) as (c) with additional simulation of gravity, e) as (d) with additional pull force simulation, f) as (e) with additional parameter optimization. xz plane refers to the transverse plane, xy to the coronal plane and yz to the sagittal plane.

Table 1: Computation times for different simulation stages and for the complete pipeline (mean and standard deviation of computation times is given across datasets) obtained on Intel Core i7-7700 3.6 GHz. For description of the stages, refer to Methods.

Computation time	Stage 1	Stage 2	Stage 3	Stage 4	Complete pipeline
Mean	96 s	133 s	187 s	188 s	564 s
St. dev.	4.4 s	4.6 s	7.3 s	8.5 s	12.3 s

4 Discussion and Conclusion

The presented image registration framework for the registration of MRI with DBT volume has opened new possibilities in investigating and comparing material models, registration strategies and patient-specific optimization that have not been possible in the registration of MRI with X-ray mammograms due to the projection of deformations. We increased the complexity of our previous model [23] by introducing additional gravity simulation along with the estimation of the unloaded state, as well as a pull force of adjustable size that could recover the manual positioning of the breast on the compression plate. Our preliminary results with a limited number of datasets show that by incorporating both loading steps, the agreement of breast shapes expressed by the Dice coefficient can be considerably increased compared to a registration with compression simulation and estimation of unloaded state.

In the current study, we evaluated only the performance of the isotropic material model. The anisotropic material model was not taken under consideration as our previous studies [23] showed that the isotropic material in combination with the estimation of the unloaded state delivered comparable results to the more complex anisotropic material model. Beside that the anisotropic model also showed to be sensitive to the selections of material characteristics.

With the complex simulation strategy the optimization of model and simulation parameters delivered material stiffness values of low variability across datasets ($E_{fat} = 930 \pm 295$ Pa, $E_{gland} = 3195 \pm 630$ Pa, $E_{muscle} = 5490 \pm 130$ Pa) that were well in the range of other studies as e.g. *Samani et al.* [24] and *Hopp et al.* [19]. Furthermore, the optimal relative rotations were kept below 10°, which agrees with the expected rotations in CC view. This demonstrates that a physically more realistic model could potentially decrease the search space for optimizing parameters, thereby reducing the computational time.

The presented results were achieved with a fixed number of 100 iterations as stopping condition for parameter optimization using particle swarm. Although the optimization enhanced the Dice coefficient for all datasets, we noticed that even after 100 iterations the selection of parameter combinations did not converge, which suggest that the parameter selection could potentially further improve. In general, the global minima of the objective function were clearly separated from other functional values. However, for dataset 4 it was observed that the global minimum appeared for two different parameter combinations. This

calls for the integration of an optimization approach specific for our biomechanical model that would allow a more intelligent search of parameter combinations. Furthermore, to judge the registration accuracy, additional optimization criteria along with the single scalar Dice coefficient are planned to be investigated, such as incorporating the information about the local shape of the breast to tune parameters to match the skin surface boundary.

Despite these limitations, the results of the registration are promising as our complex simulation model with patient-specific optimization enhanced the Dice coefficient from an average of 88.1 % for a mere DBT compression simulation to approximately 94.4 %. For a proof of principle, CC view mammograms were used in this study. In future we will apply the framework to an extend patient collective and oblique mammographic views to investigate the influence of registration parameters more deeply.

References

[1] Altobelli E, Lattanzi L (2014) Breast cancer in European Union: An update of screening programmes as of March 2014 (Review). Int J of Oncology 45:1785–1792

[2] Tempany C.M.C, Jayender J, Kapur T, Bueno R, Golby A, Agar N, Jolesz F.A (2015) Multimodal Imaging for Improved Diagnosis and Treatment of Cancers. Cancer 121:817–827

[3] Mertzanidou T, Hipwell J, Cardoso M. J, Zhang X, Tanner C, Ourselin S, Bick U, Huisman H, Karssemeijer N, Hawkes D (2012) MRI to X-ray mammography registration using a volume-preserving affine transformation. Medical Image Analysis 16(5):966–975

[4] Krüger J, Ehrhardt J, Bischof A, Handels H (2014) Simulation of Mammographic Breast Compression in 3D MR Images Using ICP-Based B-Spline Deformation for Multimodality Breast Cancer Diagnosis. Int J of Computer Assisted Radiology and Surgery 9(3):367–377

[5] Ruiter N.V, Stotzka R, Müller T.O, Gemmeke H, Reichenbach J.R, Kaiser W.A (2006) Model-based registration of X-ray mammograms and MR images of the female breast. IEEE Trans. on Nuclear Science 53(1):204–211

[6] Mertzanidou T, Hipwell J, Johnsen S, Han L, Eiben B, Taylor Z, Ourselin S, Huisman H, Mann R, Bick U, Karsse-meijer N, Hawkes D (2014) MRI to X-ray mammography intensity-based registration with simultaneous optimisation of pose and biomechanical transformation parameters. Medical Image Analysis 18(4):674–683

[7] Lee A.W.C, Rajagopal V, Bararenda Gamage T.P, Doyle A.J, Nielsen P.M.F, Nash M.P (2013) Breast lesion co-localisation between X-ray and MR images using finite element modeling. Medical Image Analysis 17(8):1256–1264

[8] Hopp T, Dietzel M, Baltzer P.A, Kreisel P, Kaiser W.A, Gemmeke H, Ruiter N.V (2013) Automatic multimodal 2D/3D breast image registration using biomechanical FEM models and intensity-based optimization. Medical Image Analysis 17(2):209–218

[9] Mertzanidou T, Hipwell J, Han L, Huisman H, Karssemaijer N, Hawkes D (2011) MRI to X-ray Mammography Registration Using an Ellipsoidal Breast Model and Biomechanically Simulated Compressions. In: Proc. of the Workshop on Breast Image Analysis, MICCAI 2011, pp. 161–168

[10] Niklason L.T, Christian B.T, Niklason L.E et al (1997) Digital tomosynthesis in breast imaging. Radiology 205:399–406
[11] Hopp T, Ruiter N.V, Dietzel M, Baltzer P, Kaiser W (2010) Bildfusion von Röntgen–Mammogrammen mit Magnetresonanztomographie–Volumen. In: Proc. Deutscher Röntgenkongress 2010.
[12] Wu S, Weinstein S, Keller B.M, Conant E.F, Kontos D (2012) Fully-Automated Fibroglandular Tissue Segmentation in Breast MRI. In: Proc. IWDM 2012, LNCS 7361, pp. 244—251
[13] Bliznakova K, Bliznakova Z, Bravou V, Kolitsi Z, Pallikarakis N (2003) A three-dimensional breast software phantom for mammography simulation. Physics in Medicine and Biology 48:3699–3719
[14] Fang Q, Boas D (2009) Tetrahedral mesh generation from volumetric binary and gray-scale images In: Proc. of IEEE Int. Symp. on Biomedical Imaging 2009, pp. 1142–1145
[15] Rivlin R.S (1948) Large Elastic Deformations of Isotropic Materials. In: Fundamental Concepts, Philosophical Transactions of the Royal Society of London. Series A, Mathematical and Physical Sciences 240(822):459–490
[16] Dassault Systemes: ABAQUS/CAE 6.13 User's Manual, Online Documentation
[17] Eiben B, Vavourakis V, Hipwell J, Kabus S, Lorenz C, Buelow T, Hawkes D (2014) Breast deformation modelling: comparison of methods to obtain a patient specific unloaded configuration. In Proc. SPIE Medical Imaging, 9036, 903615
[18] Amidror I (2002) Scattered data interpolation methods for electronic imaging systems: a survey. Journal of Electronic Imaging 11(2):157—176
[19] Hopp T, Dapp R, Zapf M, Kretzek E, Gemmeke H, Ruiter N.V (2015) Registration of 3D Ultrasound Computer Tomography and MRI for evaluation of tissue correspondences. In: Proc. SPIE 9419, Medical Imaging 2015: Ultrasonic Imaging and Tomography, 94190Q
[20] Kennedy J, Eberhart R. C (1995) Particle swarm optimization. In: Proc. of the IEEE international conference on neural networks IV, Piscataway: IEEE, pp. 1942—1948
[21] Dice L.R (1945) Measures of the Amount of Ecologic Association Between Species. Ecology 26(3):297—302
[22] Duda V.F, Schulz-Wendtland R (2004) Mammadiagnostik, Springer Berlin
[23] Hopp T, de Barros Rupp Simioni W, Exposito Perez J.A, Ruiter N.V (2015) Comparison of biomechanical models for MRI to X-ray mammography registration. In: Proc. 3rd MICCAI Workshop on Breast Image Analysis, München, October 9, 2015
[24] Samani A, Zubovits J, Plewes D (2007) Elastic moduli of normal and pathological human breast tissues: An inversion-technique-based investigation of 169 samples. Physics in Medicine and Biology 52(6):1565

Towards a real-time full-field stereoscopic imaging system for tracking lung surface deformation under pressure controlled ventilation

Samuel Richardson[a,1], Thiranja P. Babarenda Gamage[a,1], Amir HajiRassouliha[a], Toby Jackson[a], Kerry Hedges[a], Alys Clark[a], Andrew Taberner[a,b], Merryn H. Tawhai[a], Poul M.F. Nielsen[a,b]

a Auckland Bioengineering Institute, University of Auckland, New Zealand

b Department of Engineering Science, University of Auckland, New Zealand

Abstract. The normal decline in lung function that occurs with age is virtually indistinguishable from early disease, leading to frequent misdiagnosis in the elderly. Computational modelling promises to be a useful tool for improving our understanding of lung mechanics. However, there is currently no unified structure-function computational model that explains how age-dependent structural changes translate to decline in whole lung function. Furthermore, existing models suffer from weak parameterisation due to lack of available data. To begin addressing this issue, we have developed a real-time full-field stereoscopic imaging system for tracking surface deformation of the rat lung during pressure-controlled ventilation. The system will enable the acquisition of novel physiological data on lung tissue mechanics. This study presents preliminary lung surface tracking results from experiments on Sprague-Dawley rats under pressure controlled ventilation. This rich data will provide us with previously unavailable information for constructing and validating more realistic computational models of the lung to help us better understand the mechanisms behind decline in lung function with aging and help guide the development of new diagnostic methods to distinguish age from lung disease.

[1]Authors acknowledge joint first authorship

1 Introduction

The mechanics of lung tissue is challenging to characterise because standard methods to measure stress and strain cannot be applied to the extremely delicate and highly deformable alveolar tissue of the lung. Knowing how the mechanical constituents of the alveolar wall interact with the complex "sponge-like" geometry of the alveoli is key to understanding how microstructural remodelling, which occurs with both increasing age and disease, translates to diagnostic measurements of lung function and to the progression of pathology. This is particularly relevant to the older population because the normal decline in lung function that occurs with age is virtually indistinguishable from early disease. For example, with early emphysema, the age dependent changes in alveolar structure are indistinguishable in standard imaging functional tests. This can lead to misdiagnosis in the elderly.

The elastic behaviour of alveoli is tightly coupled to surface tension in the thin layer of liquid with which they are lined, and they operate under significant pretension that causes collapse when the lung tissue is excised or sliced. Basic understanding of how alveolar volume and shape changes during lung inflation and deflation still remains strongly debated [1,2]. Various modes have been proposed [3] including isotropic expansion [4,5], septal folding/unfolding at low volumes [6] and stretch at high volumes [7], and alveolar recruitment/derecruitment [8,9]. These modes have implications for stress transmission during normal and ventilator-assisted breathing, and in stress-associated propagation of pathology [10,11]. More evidence is required to determine whether one or more of these modes of inflation are dominant in normal and pathological breathing.

Computational modelling may prove to be a useful tool for improving our understanding of lung mechanics, and several computational models have been proposed for the mechanics of lung tissue [12-16]. However, there is currently no unified structure-function computational model that explains how age-dependent structural changes translate to decline in whole lung function. Existing models suffer from weak parameterisation due to lack of available data. For example, constitutive relations for biological tissues are typically parameterised by fitting their coefficients to data acquired during uni- or bi-axial stretching of tissue strips *ex vivo*. While these approaches have been attempted for lung parenchymal (alveolar) tissue [11,16-18], they suffer from distortion of alveoli at the cut surfaces of the samples, obliteration of the air-liquid interface that normally contributes a significant proportion of the elastic response, and small airway smooth muscle contraction via calcium release from disrupted cells. The mechanical parameters and stress-strain relationships determined from this data thus exhibit a large degree of variability, making it difficult to parameterise and interpret results from computational models [19]. Robust quantification of the mechanical behaviour of the lung therefore requires measuring its function while the lung is intact and normal surface forces are present.

To date, there have been limited measurements of the deformation of the intact lung during ventilation. A previous study in the mid 1980s used synchronised stroboscopic photography to stop motion in a dog heart at 20 evenly spaced intervals

over a respiratory cycle during ventilation at 1 Hz [20]. The lungs were then photographed during quasi-static deflation. Prior to imaging, ink dots were marked on a portion of the pleural surface with 84 square markers, and the side lengths and areas of these squares were measured during quasi-static deflation to quantify lung surface deformation. Nonuniformities in change in areas of the squares were shown and were attributed to interregional airflow and elastic wave propagation in the parenchyma during high-frequency ventilation. Limitations of this study include the use of only a single camera view for estimating side lengths and areas from the relatively complex shape of the lung and manual digitisation of markers for tracking surface motion. This prevents accurate estimation of surface displacements and strains for parameterising computational models. Stereophotogrammetry has also been used for reconstructing surfaces of biological tissues, for example, a previous study used a single-camera for capturing exposed in vivo geometric data in an open surgical environment [25]. However, reconstructions using a single camera are not well suited for accurately capturing the shape of deforming surfaces Furthermore, few studies make use of intrinsic surface texture for tracking surface deformation.

In this study, we aimed to design a real-time full field stereoscopic imaging system for tracking lung surface deformation under pressure-controlled inflation. This system will enable us to acquire rich, accurate, robust, and previously unavailable physiological data on lung tissue mechanics from whole rat lungs. Such data could be interpreted using computational models to improve our understanding of lung mechanics.

Section 2 describes the methodology used for designing and constructing the full-field stereoscopic imaging system, the apparatus developed for controlling inflation of the lung, and the experimental protocol performed on the rat lungs and the. Section 3 presents preliminary pressure-volume results from the experiments and lung surface tracking results. Limitations of the imaging system are described and approaches for improving the system are discussed in Section 4.

2 Methodology

2.1 Measuring the pressure-volume relationships in rat lungs

Sprague-Dawley rats were used in this study for two key reasons: their similarities to humans in alveolar air-space enlargement with age [21], and their relatively large alveoli (~90 μm diameter) [21] compared with lung size (~20 mL) [22], enabling visualisation of subpleural alveolar deformation by optical coherence tomography (which has a voxel size of ~15 μm × ~15 μm × ~15 μm). The animals used in this study were large male (350 ± 50) g Sprague-Dawley rats, taken as cull rats

from breeding stock. Due to the nature of cull rats, their ages were unknown. A real-time pressure control system was developed to measure quasi-static lung pressure-volume relationships.

A compactRio (National Instruments) based real time pressure control system has been developed to control the inflation of the lungs of the Sprague-Dawleys. A syringe pump set up gives us the ability to control pressure in real time with volume and pressure resolutions of ±5 µl and ±5 Pa respectively. To achieve this a 100 ml glass syringe has been mounted and actuated by a Physik Instrumente DC-Mike linear actuator that has an accuracy of of 0.0592 µm. The system is currently set up to servo on pressure, inflation routines step the pressure in 100 Pa increments up to a set point.

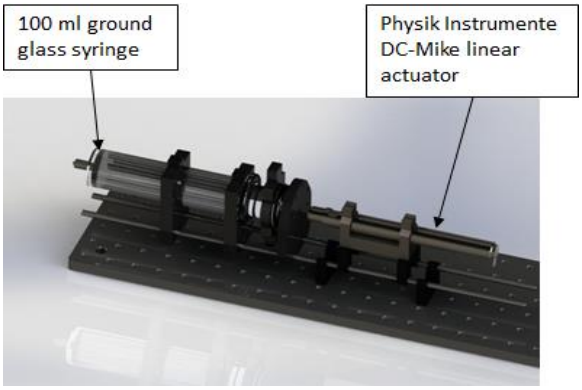

Fig. 1. Annotated CAD model of the syringe pump setup mounted on an optical board.

2.2 Imaging lung surface displacement during inflation

A full field stereoscopic imaging rig was designed and built to track the surface displacement of the lung during pressure-controlled inflation. The design and construction of this rig is described in the following sections.

2.2.1 Rig design

FLIR BlackflyS monochrome cameras that feature a SONY IMX250 sensor were selected for imaging the lung due to their high quantum efficiency and high signal to noise ratio (4760 signal to noise ratio or 73 dB dynamic range). The sensors had a 2448 pixel × 2048 pixel resolution (5.0 MP) with a 3.45 µm pixel size and were capable of imaging at 75 frames per second.

A theoretical analysis was performed to determine the optimal number of cameras that would be required to reconstruct the shape of the lung surface during the lung ventilation experiments. A geometric model based virtual camera rig was used to determine the number and optimal placement of the cameras. This was achieved by using stereo vision techniques to back-project points on the surface of a representative rat lung surface mesh onto each of the camera views. The focal distance of the lens, and the arrangement of the cameras, were then selected to maximise the field of view of the lens while also ensuring that at least 3 cameras could see corresponding points on the majority of the lung surface to ensure robust 3D surface reconstruction. Surface points were only back-projected and used in the analysis if the angles between the surface normal of the lung mesh and the camera's optic axis were under 45°. Surfaces that were very oblique to the camera's optic axis were not considered for this analysis. This led to the final design of an eight-camera stereo imaging system shown in Figure 2 that used Fujinon 25 mm lenses (HF25SA-1), which had a minimum object distance of 100 mm. In this configuration, 97 % of points on the lung surface could be seen in at least two cameras, while 92 % of points could be seen in at least 3 cameras. While, the individual cameras could have been placed at arbitrary positions, the camera placements were constrained to regular shapes to simplify machining of the frame and ensure the frame was rigid.

The octahedron and camera mounts were all designed to ensure that the centres of the camera sensors were held at least 223 mm apart to allow the lung to be viewed at the minimum object distance for the selected lenses.

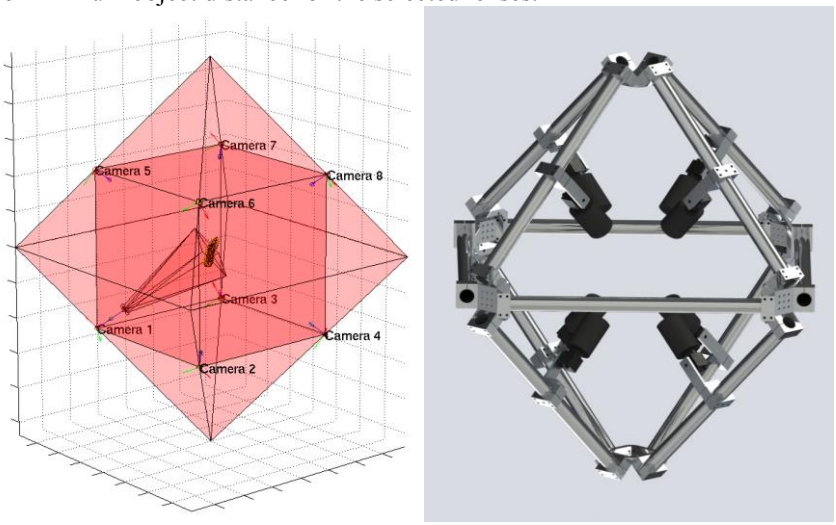

Fig. 2. a) The optimal 8 camera design of the stereo imaging system that will be used to reconstruct the shape of the lung surface and track surface deformation at different inflation pressures. The virtual camera rig with the optimal camera arrangement is shown on the left. An example field of view for camera 1 is shown, along with the mesh model used for designing the rig at the centre of the octahedron. b) The CAD of the rig was developed in SolidWorks to mount the cameras at the required locations on the rig.

2.2.2 Rig construction

With the theoretical analysis of camera placement completed, a rigid camera rig was designed in Solidworks. To ensure complete rigidity between the cameras, the geometry of the camera rig was designed as a regular octahedron. The camera mounts and octahedron corners were machined, in house, out of aluminium for rigidity, and connecting pipes were selected with an outer diameter of 30 mm and a wall thickness of 1.6 mm. The constructed rig is shown in Fig 3. The preliminary lung surface tracking results described in Section 3.2 were obtained using a single camera. To obtain these results, four high power 1270 lm LED Engin LZ1-10R200 light emitting diodes were used with diffusers to ensure even lighting and to reduce noise in the camera images. Image acquisition from the cameras was performed in Labview and the cameras were synchronized using a software trigger.

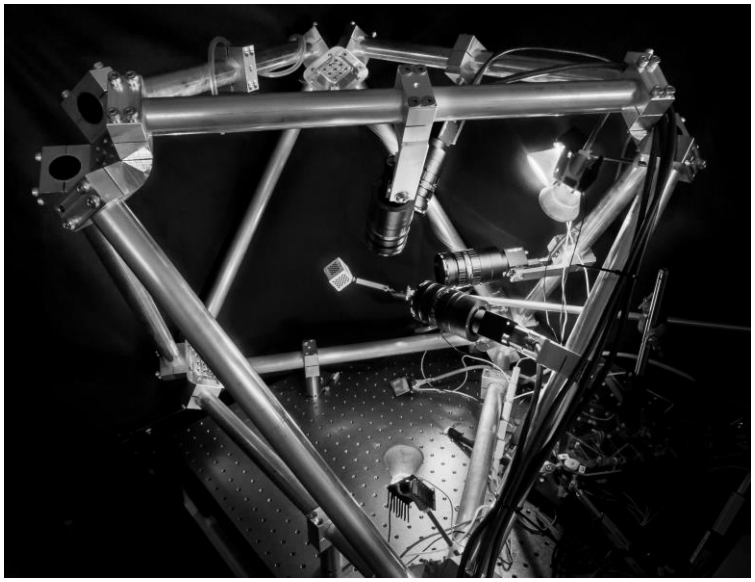

Fig. 3. Rig constructed for performing full-field imaging of the lung surface during pressure controlled inflation experiments.

2.2.3 Calibration

The cameras were calibrated prior to making measurements using a multi-plane direct calibration method developed using OpenCV tools. To robustly calibrate the cameras, multiple images of a checkerboard pattern, with a known square size, were acquired within the field of views of all cameras. This procedure was automated to

ensure the calibration procedure was accurate and rapid. A Stewart platform providing six degrees of freedom (3 translation, 3 rotation) and constructed in-house using Firgelli 120 mm linear actuators, was used to move the calibration pattern within the field of views of the cameras. This enabled us to collect a 125 calibration images in under 3 minutes.

These were used to identify the intrinsic parameters of each camera (describing the focal length, image sensor format, principal point, and radial and tangential distortions of each lens) for the current study. In future studies, the extrinsic parameters (describing the relative location and orientation of each camera) will also be identified for 3D reconstruction of the lung surface.

2.2.4 Surface tracking

A subpixel accurate phase-based cross-correlation (PCC) technique [23] was used for tracking the lung surface deformation between the image frames captured at two different inflation pressures. This technique involved cross-correlating subregions of the lung surface. The amplitude and phase spectrum of these cross-correlated subregions could be analysed in the frequency domain to efficiently identify the displacement of the subregions with subpixel accuracy (for example, with errors less than 0.05 pixel when recovering known rigid body displacements [23]). The PCC technique was applied in this study by first defining a grid of virtual points on the surface of the lung that could be seen in one camera. Square 64 pixel × 64 pixel subregions centred at these virtual points were then independently tracked across a pair of frames using the PCC technique.

2.3 Experimental protocol

Initial studies were performed on excised rat lungs that were intubated under real-time pressure. Lungs were dissected from the euthanized rats. During dissection, prior to opening the chest cavity, the trachea was exposed and the rats were intubated using a blunted 1.65 mm outside diameter (16 G) hypodermic needle. Pressure was monitored using a Honeywell pressure sensor to ensure the lungs were not subjected to excessive inflation pressures. The lungs were then manually inflated using a syringe up to a pressure of 1000 Pa so that they would not collapse upon opening the chest and release the negative pressure. Before imaging, to recruit the collapsed alveoli, lungs were fully inflated to 2800 Pa and held until inflation stopped. If inflation halted before full alveolar recruitment, pressure was cycled sinusoidally between 1000 Pa and 3000 Pa.

The pressure control system described in Section 2.1 was then used to inflate the lungs to different physiologically relevant pressures, ranging from 1000 Pa to 2800 Pa during stereo imaging with 6 s holds between steps, an example of the inflated lungs can be seen in Figure 4.

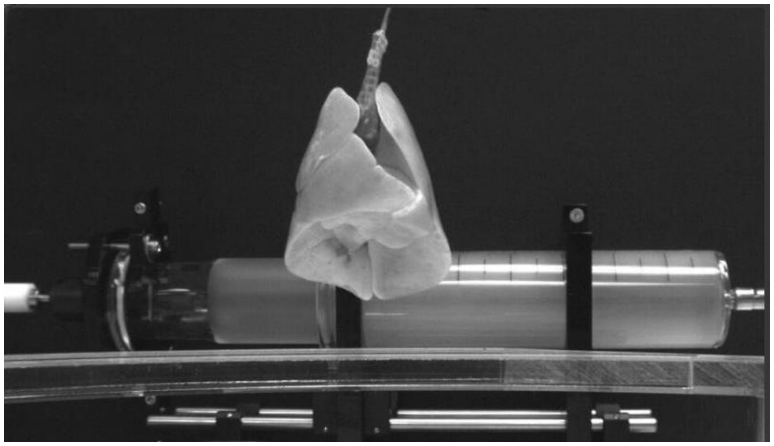

Fig. 4. Inflated whole lungs under pressure control at 2500 Pa. The syringe pump system can be seen in the background.

3 Results

3.1 Pressure-volume relationship in rat lungs

Preliminary pressure-volume results from the experiments performed in this study are shown in Figure 5. These results exhibited hysteresis due to inflation with air rather than saline, and were similar qualitatively to those previously measured in the literature [24]. The results show that the lung volume increased or decreased at different stages of ventilation when the pressure was held constant (indicated by the vertical lines in Figure 5). Figure 5 shows a clear, sudden, reduction in pressure when held at 900 Pa, this is likely caused by the opening of a number of alveoli that had previously been held closed by the surface tension in the surfactant.

3.2 Lung surface tracking

The preliminary tracking results in Figure 6 show 2D surface tracking results from the anterior surface of the left rat lung lobe from one camera. These results indicated that there was a continuous displacement field between the two inflation pressures in which the lung surface was imaged.

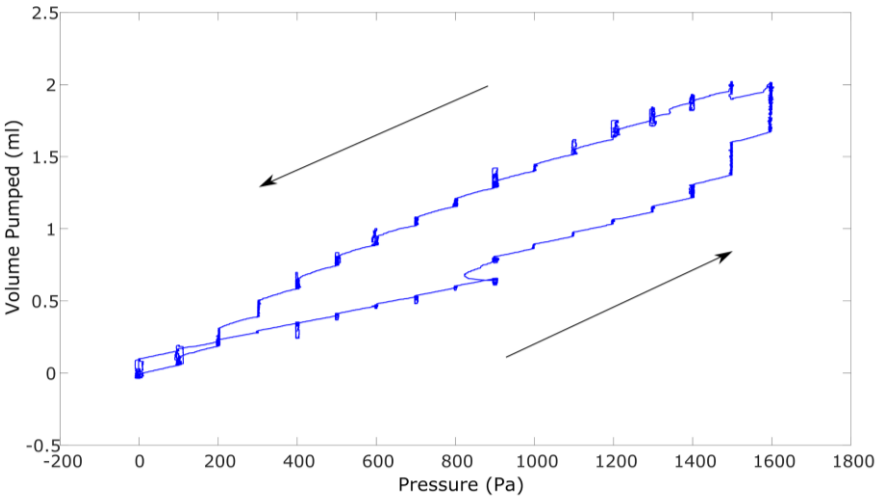

Fig. 5. Typical pressure volume loop for ex-vivo rat left lobe, inflated under pressure control. The pressure was incremented in 100 Pa steps to generate the loading and unloading curves, the arrows indicating the direction of loading and unloading.

4 Discussion

This paper described the development and implementation of the first real-time imaging system for tracking deformation of the intact lung surface under pressure-controlled ventilation. Lung tissue is extremely delicate and prone to damage during dissection. Traditional approaches for measuring pressure volume curves in lungs, either under volume or pressure controlled inflation, require the flow-rate to be monitored to estimate the volume of air in the lungs. However, these approaches are highly susceptible to leaks. A benefit of our system is the ability to control pressure allowing us to maintain the forces on the tissue while using 3D reconstruction of the entire lung surface for estimating lung volume.

Preliminary results were presented that demonstrated the novel physiological data that can be produced from the system. The surface tracking results showed that the displacement field between two relatively high inflation pressures were continuous. Future studies will investigate if this is also observed at lower inflation pressures to determine if the pleural surface stretches and expands to accommodate increase in lung volume during inflation. While polarising filters were placed in front the camera lenses, specular reflections from the LEDs were observed on the surface of the lung. Tracking cannot be accurately performed in these regions and were masked out of the results presented in Section 3.2. These reflections can be reduced by using more translucent materials to construct the diffusers for the LEDs, and adding polarisers in front of the diffusers.

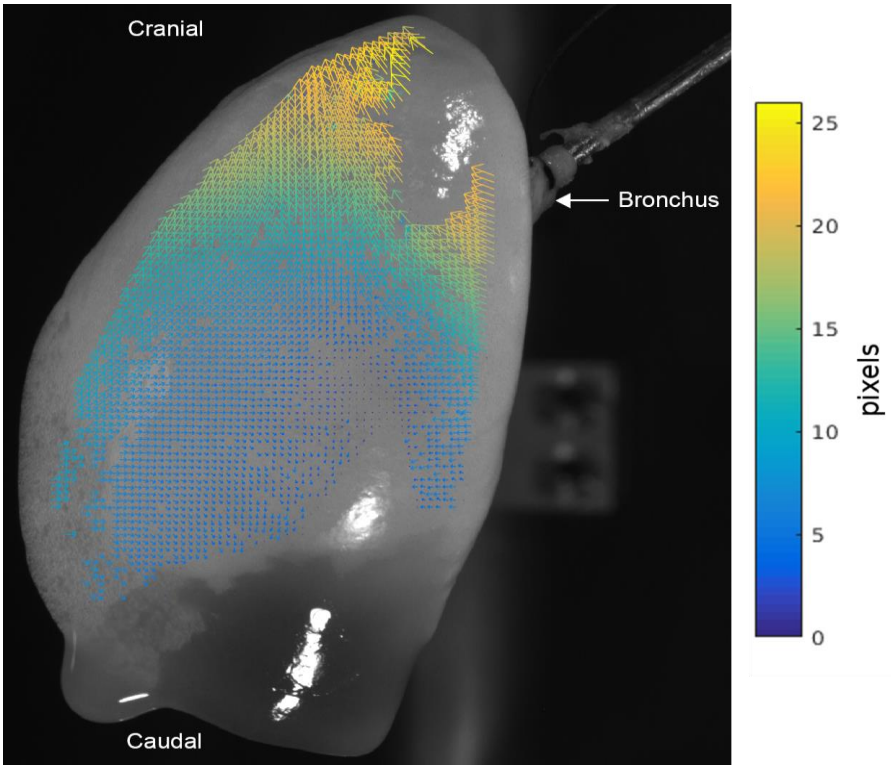

Fig. 6. 2D displacement vectors indicating the motion of the anterior left lobe surface of the rat lung between an inflation pressure of 2200 Pa and 2300 Pa. The arrow lengths have been increased by a factor of 2 for visualisation purposes.

The results presented in this paper only considered tracking of the lung surface from a single camera. This analysis will be extended to track and reconstruct surface deformation across all eight cameras in 3D allowing for full field measurement of lung surface deformation.

A limitation of the imaging system is that it only provides deformation measurements on the surface of the lung. Investigating the behaviour of the subpleural of the lung is of importance, particularity for determining the mechanism by which the lung expands as described in Section 1. However, to date, there has been insufficient experimental evidence for proving either of these theories. To address this limitation of our imaging system and test existing hypotheses in the literature, we have been developing an optical coherence tomography (OCT) imaging system that can provide dynamic imaging of the pleural and subpleural surfaces of the rat lung, with the aim of visualising and tracking 3D deformation of alveoli during ventilation.

5 Conclusions

A system was developed for inflating rat lungs to a specified pressure set point. Further to this, an imaging setup has been designed and tested that allows for the 3D measurement of surface strains during quasi-static inflation of the lungs. Preliminary results showed pressure-volume measurements that were consistent with those previously measured in the literature, and the surface tracking results produced displacement fields between inflation pressures were continuous. We envision that the computational models that can be developed and validated from the rich datasets that will be obtained from this system would help us better understand the mechanisms behind decline in lung function with aging with the aid of computational modelling, and guide the development of new diagnostic methods to distinguish age from lung disease.

Acknowledgments

The authors are grateful for financial support from the Royal Society of New Zealand Marsden Fund, and the Auckland Bioengineering Institute, The authors thank Stephen Olding for machining the stereo imaging rig.

References

1. Weibel ER, Nieman GF, Gatto LA, Frazer DG, Schittny JC, Woods JC, Conradi MS,Yablonskiy DA (2012) Commentaries on viewpoint: unresolved mysteries. J Appl Physiol.113(12):1948-9
2. Smaldone GC, Mitzner W (2012) Viewpoint: unresolved mysteries. J Appl Physiol.113(12):1945-7
3. Gil J, Bachofen H, Gehr P, Weibel ER (1979) Alveolar volume-surface area relation in airandsaline-filled lungs fixed by vascular perfusion. J Appl Physiol. 47(5):990-1001
4. Dunnill MS (1967) Effect of lung inflation on alveolar surface area in the dog. Nature. 214(5092):1013-4
5. Namati E, Warger WC, Unglert C, Eckert J, Hostens J, Bouma B, and Tearney G (2013) Fourdimensional visualization of subpleural alveolar dynamics in vivo during uninterrupted mechanical ventilation of living swine. Biomed Opt Express. 4(11):2492-506
6. Oldmixon EH, Hoppin Jr. FG (1991) Alveolar septal folding and lung inflation history. J Appl Physiol. 71(6):2369-79
7. Tschumperlin DJ, Margulies SS (1999) Alveolar epithelial surface area-volume relationship in
isolated rat lungs. J Appl Physiol. 86(6):2026-33
8. Forrest JB (1970) The effect of changes in lung volume on the size and shape of alveoli. J Physiol.210(3):533-47
9. Carney DE, Bredenberg CE, Schiller HJ, Picone AL, McCann UG, Gatto LA, Bailey G, Fillinger M, Nieman GF (1999) The Mechanism of Lung Volume Change during Mechanical Ventilation. Am J Respir Crit Care Med. 160(5):1697-17021999
10. Amin SD, Suki B (2012) Could dynamic ventilation waveforms bring about a paradigm shift in mechanical ventilation? J Appl Physiol. 112(3):333-4

11. Kononov S, Brewer K, Sakai H, Cavalcante FSA, Sabayanagam CR, Ingenito EP, Suki B (2001) Roles of mechanical forces and collagen failure in the development of elastase-induced emphysema. Am J Resp Crit Care Med. 164:1920-1926
12. Fredberg JJ, Stamenovic D (1989) On the imperfect elasticity of lung tissue. J Appl Physiol.67(6):2408-19,
13. Freed AD, Einstein DR (2012) Hypo-elastic model for lung parenchyma. Biomech Model Mechanobiol. 11(3-4):557-73
14. Tawhai MH, Nash MP, Lin CL, Hoffman EA (2009) Supine and prone differences in regional lung density and pleural pressure gradients in the human lung with constant shape. J Appl Physiol. 107(3):912-20
15. Denny E, Schroter RC (2006) A model of non-uniform lung parenchyma distortion. J Biomech.39(4):652-63
16. Bel-Brunon A, Kehl S, Martin C, Uhlig S, Wall WA. Numerical identification method for the non-linear viscoelastic compressible behavior of soft tissue using uniaxial tensile tests and image registration - application to rat lung parenchyma. J Mech Behav Biomed Mater. 29:360-74
17. Debes JC, Fung YC (1992) Effect of temperature on the biaxial mechanics of excised lung parenchyma of the dog. J Appl Physiol. 73(3):1171-80
18. Vawter DL, Fung YC, West JB (1978) Elasticity of excised dog lung parenchyma. J Appl Physiol. 45(2):261-9,
19. Rausch SMK, Martin C, Bornemann PB, Uhlig S, Wall WA (2011) Material model of lung parenchyma based on living precision-cut lung slice testing. Journal of the Mechanical Behavior of Biomedical Materials, 4(4), 583–592
20. Lehr JL, Butler JP, Westerman PA, Zatz SL, Drazen JM (1985)"Photographic Measurement of Pleural Surface Motion during Lung Oscillation." Journal of Applied Physiology 59, no. 2:623–33.
21. Lum H, Mitzner W (1987) A species comparison of alveolar size and surface forces. Journal of Applied Physiology, 62(5), 1865–1871.
22. Kerr JS, Yu SY, Riley DJ (1990) Strain specific respiratory air space enlargement in aged rats. Exp Gerontol. 25(6):563-74
23. Malcolm DTK, Nielsen PMF, Hunter PJ, Charette PG (2002) "Strain Measurement in Biaxially Loaded Inhomogeneous, Anisotropic Elastic Membranes." Biomechanics and Modeling in Mechanobiology 1, no. 3:197–210. doi:10.1007/s10237-002-0018-8.
24. Frazer, D. G., & Weber, K. C. (1976). Trapped air in ventilated excised rat lungs. Journal of Applied Physiology, 40(6), 915–922.
25. Broderick S.P., Doyle B.J., Kavanagh E.G., Walsh M.T. (2013) Photogrammetry for use in biological surface acquisition: investigation of use, geometric accuracy and consequence on analysis. Computer Methods in Biomechanics and Biomedical Engineering: Imaging & Visualization, 1:4, 234-246

Patient-specific simulation: non-destructive identification method for soft tissue under large strain – Application to pelvic system

Olivier Mayeur (1, 2), Jean-François Witz (1, 2), Pauline Lecomte-Grosbras (1, 2), Michel Cosson (2, 3, 4) and Mathias Brieu (1, 2).

1. Centrale Lille, France; 2. Laboratoire de Mécanique de Lille, CNRS FRE-3723, France, France; 3. CHU Lille, Service de Chirurgie Gynécologique, F-59000 Lille, France ; 4. Université Lille Nord de France, Faculté de Médecine, F-59000 Lille, France.

Abstract This work presents a non-destructive method to assess mechanical properties of the patient-specific soft tissues of a multi-organ system under large strain. The presented application is focusing on the female pelvic cavity. Based on an experimental data bank of mechanical properties, dynamic MRI's displacement field analysis, MRI's geometrical reconstruction and FE model of the pelvic cavity, a protocol has been developed to identify the material properties of a specific patient's organs. The purpose of this paper is to tackle that issue by using an inverse Finite Element analysis. Mechanical properties of the soft tissues are optimized to obtain the MRI's observed displacement of the cervix on the FE model.

Introduction

According to the Birth Trauma Association (BTA), in the UK alone (777,000 births in 2015), around 10,000 women a year develop Post Traumatic Stress Disorder (PTSD) and an additional 200,000 may feel traumatized by childbirth and develop one or more symptoms of PTSD. The well-being and healthy recovery of patients after labour, delivery and in the postpartum can be for instance impaired by emergency cesarean section (20% at first delivery), instrumental delivery (10-15% at first delivery), or severe perineal tears involving the anal sphincter (around 5% at first delivery) [1]. In the postpartum period, this would mean 1 million women in Europe every year. Along the same lines, this would mean 65000 women with severe and around 130,000 women with moderate post-traumatic stress disorders. More and more pregnant women ask for a personalized/individual information about their own risk incurred at the time of childbirth, performed ahead of the event [2]. Medical doctors need to be informed on patient's specific mechanical properties to analyze physiology, physiology-pathology or delivery and identify potential risk factor. The stiffness of biological tissues significantly affects the mobility of the pelvic system. Tissues stiffness have thus an impact on pathologies and surgical

treatments, when occurring. It would therefore be a major improve of patient's treatments to determine the in-vivo mechanical properties in order to define accurately pathologies and estimate surgical technics accuracy. This approach could be used to perform patient-specific simulation to help for treatments and/or prevention.

In obstetrical medicine, it is common to carry out diagnoses by considering geometrical aspects through medical imaging techniques [3]. However, there is scientific lock to characterize the mechanical properties of the pelvic system in an in-situ way. The proposed solution is the use of computational biomechanics, and more specifically personalized simulation for this kind of patient diagnosis, by solving an inverse problem.

Inverse method is commonly used in mechanical engineering to identify unknown parameters thanks to FE analysis and a range of identified and controlled parameters [4]. It is a well-known technique, but such an approach requires developments in a biomedical context. Due to the uncertainties resulting from employed techniques and biological dispersions, such a tool needs an adapted protocol.

First, the model must be patient specific following the different needs of the inverse method. This requires significant work on the geometrical definition of the system, representative of the patient while limiting measurement uncertainties [5]. This competence demands reliable image processing and reconstruction algorithms adapted to this pelvic system in clinical situation. Current developments show a strong contribution of the research community in the automation of such reconstruction protocols [6], [7]. According to the observable value expected to resolve inverse problem, the dynamic MRI makes it possible to quantify the displacement field of organs according to image registration techniques [8]. Then, as in any mechanical problem, we must also know the loading condition applied to the system corresponding to a pushing effort, which is well documented in the literature [9], [10]. Finally, the identification of mechanical properties, behavior law of soft tissues or interindividual dispersion frequently involved in pelvic cavity investigation [5], [11], [12], [13] but difficult to link correctly to the specific mechanical properties of a specific patient, can be addressed by inverse method.

This paper presents through the inverse approach the different input (geometry, loading, displacement and behavior law), required to identify the patient-specific mechanical properties. In a first part, we will evaluate the numerical process and in a second one, it will be applied to specific patients to validate our approach, discussions and conclusions will end the paper.

Material and method

FE Models generation

In order to succeed in identifying the mechanical properties of pelvic organs with our non-destructive approach, the first step is to define the specific geometry of patient in order to generate a personalized model compatible with FE analysis.

The first requirement concerns the acquisition of the geometry of the entire pelvic cavity. This step is carried out by MRI technique with a protocol conventionally used during clinical examination (3 Tesla MRI through 3 sequences of 2D images on the axial, coronal and sagittal incidences). This approach leads to constraints on the accuracy of the pixel size (0.7 mm), but it was chosen deliberately to ensure future clinical applications (figure 1a). MRI images are segmented by surgeons and radiologists, whose skills make it possible to determine precisely the main anatomical structures. The 3D model is then generated on Avizo software in order to have a three-dimensional representation of the organs and muscles (Avizo Standard edition 7® Visualization Sciences Group VSG, SAS). Next, we use CAD software to define representative surfaces of the system through B-splines. This step is necessary to make the geometric representations compatible with our FE simulations (delete reconstruction artefacts, interface between anatomical structures …). During this step, we also add some anatomical suspension structures, which are not visible to MRI due to insufficient resolution to be reconstructed (figure 1b). Previous work is already published on this model and the requirement to take into account those structures to represent the kinematics of the system during the FE simulations [5].

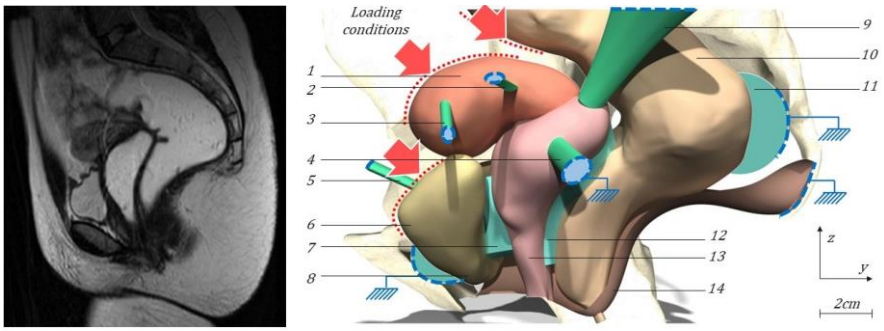

Fig. 1 (a) MRI of the 4th patient on the sagittal plane and (b) associated geometrical model with loading and boundary conditions. *1* uterus, *2* broad ligament, *3* round ligament, *4* paravaginal ligament, *5* umbilical ligament, *6* bladder, *7* Halban's fascia, *8* interface between bladder and pubis, *9* uterosacral ligament, *10* rectum, *11* interface between rectum and sacrum, *12* rectovaginal septum, *13* vagina, *14* pelvic floor.

In parallel to the static MRI analysis, dynamic MRI protocol was performed on patient in order to analyze the mobility of organs. The method used follows an approach already published based on image registration [8]. This essential step allows us to quantify specific mobility according to a pushing effort, corresponding to abdominal pressure. The internal pressure in the pelvic cavity has not been measured during MR imaging. Several pushing efforts can be considered in the literature with different levels of pressure, estimated using urodynamic techniques for several conditions (jump, valsalva, cough, abdominal effort...). In this context, we based our approach on a moderate effort with respect to the dynamic MRI examination. The patient performs an abdominal effort gradually with an end-of-thrust preservation to have more information on dynamic MRI. In this context and according to the literature, the effort is set to the order of 1 KPa. [10].

As the aim is to define the mechanical properties of organs with inverse method, the mechanical properties are not specified. However, we rely on the results known in the literature to define the behavior law used [11], [14], corresponding to a hyperelastic model (second order Yeoh model) [5], [15]. In this model the strain energy function depends only on the first invariant, I1, of the Cauchy-Green strain tensor and is given in equation 1.

$$W(I_1) = C_0(I_1 - 3) + C_1(I_1 - 3)^2 \quad (1)$$

Such strain energy density is defined by a C0 value, which at low strain represents the initial modulus of stiffness, and a C1 value, which allows the high increase in stiffness under large strains.

Inverse method

In order to perform successfully our inverse method approach (figure 2), it is necessary to define the geometry of the whole system, the behavior law type, the boundary conditions and the observed displacement. For this last point, dynamic MRI is used to quantify mobility of each patient at the end of abdominal thrust [8]. An algorithm is applied on the measured displacement field results to average the mobility on different anatomical areas. Equivalent algorithm is used to average the simulation results, based on the FE meshing in those areas. We mainly focus on the cervix location because it presents an essential criterion for the quantification of displacements, especially in pathological situation such as cystocele [5]. This measured displacement will become our target value in the inverse method by comparison with FE results. This problem can be formulated as a minimization of a functional with respect to the $C0_{vag}$ value, where Ω corresponds to the cervix area where displacements are measured, U_{fem} the magnitude of displacement on FE simulation and U_{mri} the magnitude of displacement on dynamic MRI analysis (equation 2).

$$\underset{C0_{vag}}{argmin} \int_{\Omega} (U_{fem} - U_{mri}) \tag{2}$$

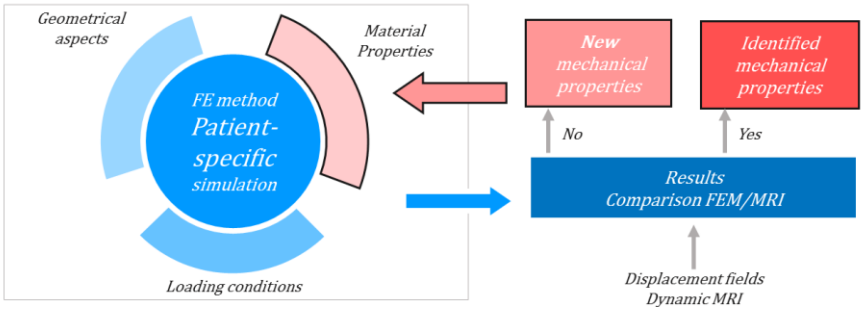

Fig. 2 General overview of the optimization algorithm (Blue: input measurements, red: Output identified parameters).

Since the goal is to identify the material properties of each organ, the inverse method process aims at defining material properties comparing FE model displacements evaluation to measured displacements. Experimental results on various tissues of the pelvic system, defining the Yeoh model, are sufficiently numerous to perform a statistical analysis [11-14]. In order to index the simulation in a coherent range, the intervals between the first and the third quartile are considered to search the real material properties [5]. To limit the input parameters, we focus our examination only on the C0 value, as the C1 value corresponds to the large strain (not observed on our dynamic MRI analysis). As this study is focused on physiological mobility, the displacement partially involves these large deformations on our system. The stiffness of the C1 value of vagina is assumed to change in accordance with the C0 value. The same approach was applied to the other organs, considering a relationship between each parameter based on the statistical data (equation 3). We have also considered simulation methods to analyze the C1 sensitivity. On converge solution, a modification of C1 shows a little influence on the mobility response in such physiological case. The observed deviation is near the results already published [5].

$$\begin{bmatrix} C1_{vag} \\ C0_{rec} \\ C1_{rec} \\ C0_{bla} \\ C1_{bla} \end{bmatrix} = \begin{bmatrix} -4.12 & 5.14 & -0.25 \\ 2.81 & -0.47 & 0.10 \\ -4.51 & 1.88 & -0.10 \\ -1.52 & 0.82 & -0.04 \\ 3.12 & -0.53 & 0.03 \end{bmatrix} \begin{bmatrix} {C0_{vag}}^2 \\ C0_{vag} \\ 1 \end{bmatrix} \tag{3}$$

Application

Four patients, presenting a normal gynecologic examination without noticeable medical history, have been integrated in the protocol (institutional ethical approval CEROG OBS 2012-05-01 R1). On a first stage, three of them, with similar mobility analysis, were selected to create a generic model built thanks to the average geometry of anatomical structures. This generic model is used to validate our tools reducing the influence of geometry on our simulation. The objective is to identify on this model the material properties of the organs to reach an imposed displacement corresponding to the one observed on MRI. This displacement is focused on the cervix area and computed thanks to the dynamic MRI analysis of the 3 patients (mean value). By coupling this target with the generic model representative of 3 patients, material identification results could be considered as average properties. Comparison with experimental databank will allow us to validate the methodology [11-14]. The second stage is to integrate the patient specific geometry on the FE model with the same displacement approach to quantify the inter-individual differences on our protocol. The last stage is to apply this protocol to the fourth patient, out of the cohort for generic model, and presenting a higher displacement field.

To summarize, we have 3 application sets where the material properties will be automatically identified:

- Phase 1: "Generic" model; average of 3 patients
- Phase 2: "Patient-Specific like" models; on the 3 previous patients
- Phase 3: "Patient-Specific real" model; 4th patient presented higher displacement on dynamic MRI.

Results

Generic model

To validate our numerical approach, a first simulation set was tested with the generic model, representative of the 3 patients. The optimization algorithm converges after four iterations with a target at 8 mm displacement (criteria at 10^{-3}mm deviation compared to target value) and allow us to identify the material property of vagina and more precisely the C0 value on our Yeoh model near to 0.16 MPa (figure 3a). The C0 and C1 values (being in MPa) for the vagina, rectum and bladder, returned by this optimization are C0vag= 0.16 MPa, C1vag= 0.48 MPa, C0rec= 0.10 MPa, C1rec= 0.09 MPa, C0bla= 0.06 MPa, C1bla= 0.03 MPa. Those parameters are then used to plot the behavior law (figure 3b). To anticipate the potential variation of pressure level, we have performed simulation with a ±10% pressure's

change to analyze the influence of such pressure on the identified mechanical properties. As example on this generic model, the C0 values of vagina for a loading condition defined at 0.9 kPa, 1 kPa and 1.1 kPa are respectively 0.12 MPa, 0.16 MPa and 0.20 MPa. This difference is relatively minor when compared to the dispersion observed on the experimental test on vaginal tissue (minimum value at 0.003 MPa and maximal value at 0.7 MPa).

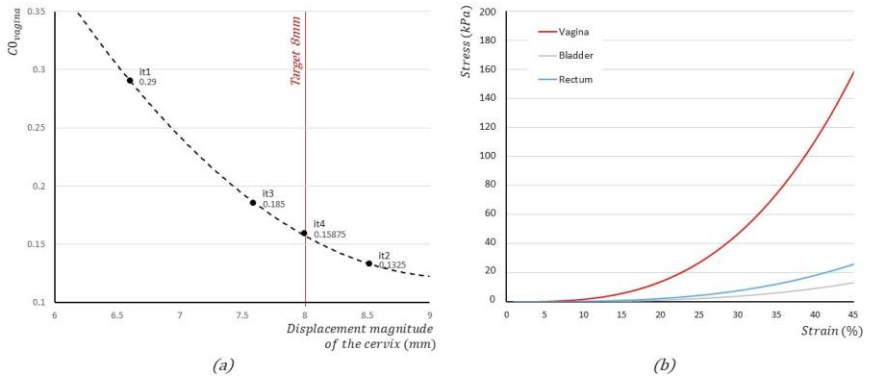

Fig. 3 (a) Displacement magnitude at the cervix for different values of C0vag, computed during the optimization process, (b) behavior law for the vagina, rectum and bladder with the C0 and C1 values determined by the optimization algorithm.

This first result allows us to validate our methodology with an identification of material properties for each organ. Since during this step one considers an average model with average displacements targeted, the identified mechanical properties are corresponding to representative values of our cohort. Results are in the range of our experimental data bank allowing us to observe a good response from our methodology.

Patient-specific simulation

The protocol is now applied to a patient-specific geometry. In that case, we assume that in physiological case, actual pressures and observed displacements are the same for all three patients. The problem is only solved with consideration of the geometrical variation, comparable to an inter-individuality (figure 4a). It leads us to study the material influence and validate our approach by comparing the results to the databank deviation (figure 4b). The algorithm was run for three models (G-PS1, G-PS2, G-PS3) with patient specific geometries. The algorithm converged after 6 iterations for G-PS2 and G-PS3. Identified values are in the range between Q1 and Q3 for each organ [2]. Optimization of the G-PS1 model converged after the fifth iteration while the estimated C0vag (0.23 MPa) value was somewhat higher than

the Q3 value (0.22 MPa) but still largely lower than the maximal experimental value (0.72 MPa). Figure 4a shows the steps of the iterative optimization process for the models as well as the fitted curves (R>0.999).

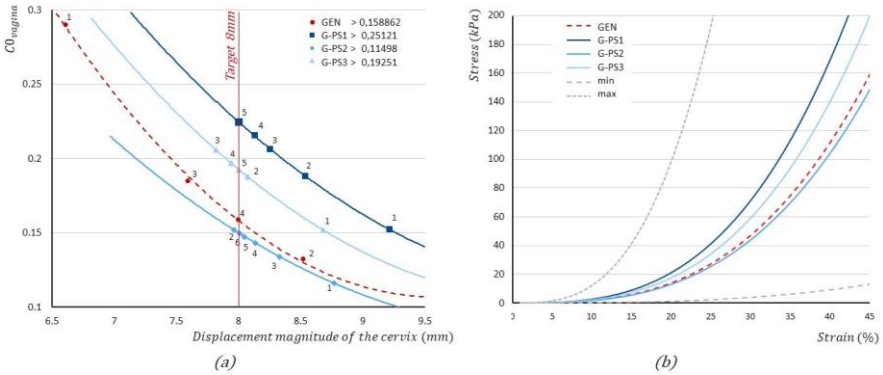

Fig. 4 (a) Displacement magnitude at the cervix for different values of C0vag of the three Patient-Specific models, (b) behavior law for the vagina plotted for the generic and 3 P**S** models where the c0vag and c1vag values are determined by the optimization algorithm (GEN: results on GE-Neric model, G-PSn: Results on Patient-Specific model).

Patient-specific results with the consideration of physiological displacement show that the study of mobility is a competition between material properties and geometrical definition. Variations can be observed on the 3 material properties of each organ and appear quite superior to the mean value of experimental data. For example on vagina of G-PS1, G-PS2 and G-PS3, the C0 value is 0.23 MPa, 0.12 MPa and 0.19 MPa respectively where the mean value on experimental data-bank is 0.11 MPa.

Patient specific details

The last part of the study is focused on a fourth patient, out of the cohort used to generate the generic model. Futhermore, the analysis of the dynamic MRI reveals a higher displacement of the cervix area of 14.5mm. This value is used as a target on our algorithm (figure 5). The strain is greater on this patient but the observed displacement remains in a physiological domain with relatively low mobility when compared to pathological mobility. The identified mechanical properties of this patient give a C0 value for vagina at 0.13 MPa.

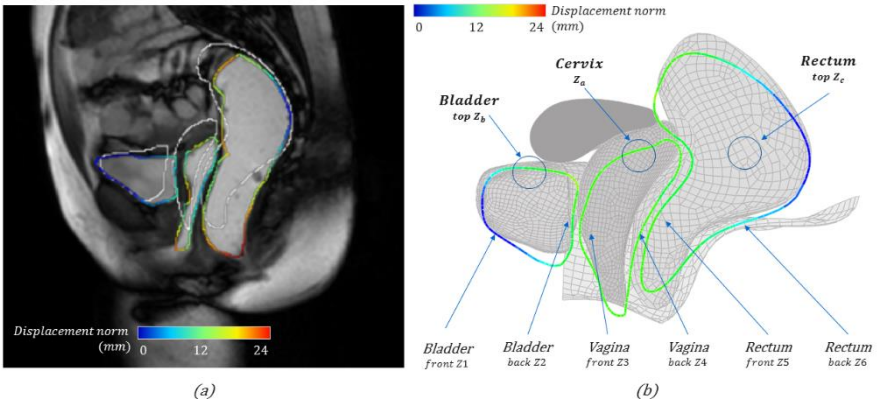

Fig. 5 Comparison between (a) displacement fields of dynamic MRI (outlines in white: initial position of organs, outlines in color: displacement magnitude at the end-of-thrust) and (b) FE results of the identified solution with definition of different analysis area.

The displacements computed from medical-imaging data analysis are compared with our FE simulation results. On FE model, the nodal displacements in a given region of interest (ROI) are considered for the cervix (optimization criterion) and are related to the same ROI of the MRI, equivalent to a dozen voxels (figure 5b). It is interesting to verify the accuracy of the displacement field in other areas of the pelvic system. The displacements of bladder and rectum are also measured on the top. The front and the back of each organ are considered on MRI and FE results to study the mobility near the fasciae (figure 6b).

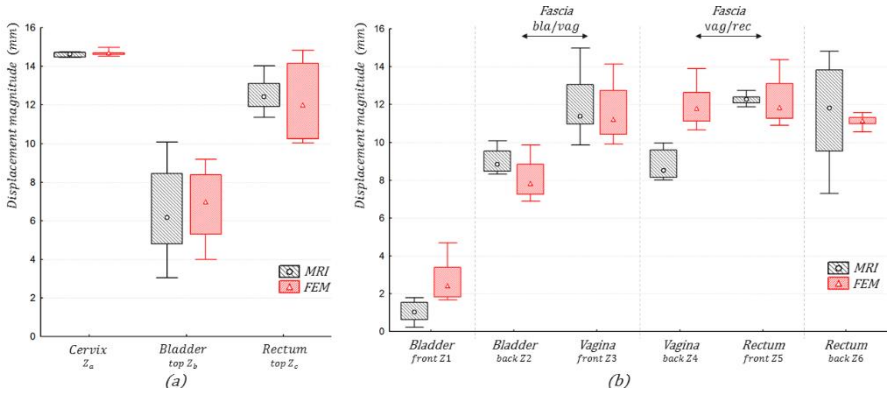

Fig.6 Patient-specific comparison between FE and MRI results for (a) the upper zones of organs and (b) anterior and posterior location of the bladder, vagina and rectum. The localization of the analysis areas is defined on the figure 5b. The definition of those areas is linked to the pixel size of the dynamic MRI and the corresponding nodes of the FE model.

Discussions

The use of medical imaging techniques allows us to reconstruct the geometry and to analyze a displacement field of the pelvic cavity under an imposed pushing effort. Through the FE simulation, the coupling of these two data with the knowledge of the behavior laws of the constitutive biological soft tissues enabled us to characterize the hyperelastic properties of the pelvic organs. This method makes it possible to define the specific mechanical properties of the patient. This first study shows that our algorithms converge for both representative generic models and patient specific simulations, allowing using a new method of nondestructive characterization for multiple organs under large strain.

The values identified are in the range of our experimental data bank, which reveals the good correlation between the numerical model and the experiments in this application. However, it would be interesting to carry out a study of the uncertainties caused by the measurement errors of such devices. Some variations on FE displacement results can be observed when the geometry changes due to the MRI resolution [2]. In this patient-specific application, we considered the geometry of organs as correct values without deviation. Uncertainties related to FE model generation and inverse method could be considered to see the consequences on mechanical property results. We could also consider a study of sensitivity on every parameter used for the behavior law of every organ in order to reach a better evaluation of the mechanical properties with a relevant estimation of uncertainties.

Concerning the anatomical area, we were able to show a good correlation at the loading zones located on the top of the organs (figure 6a). Observations on the anterior and posterior area of organs are more dispersive (figure 6b). This point underlines the transition to an approach with an identification of the mechanical properties of the fasciae and ligaments. This strategy will make it possible to have a complete model of the pelvic cavity without constraining the mechanical behavior of structures. In the same way, we could consider intra-organ gradients of mechanical properties to increase the precision of our approach.

During the displacement field analysis, intravaginal gel escapement was detected. The discharge of this cavity could explain also the differences observed locally in the anterior and posterior areas. Since the cervix is constrained by the anatomical structures of suspensions (Uterosacral and cardinal ligaments), its displacements are constrained as well. The mobility of the parts situated in the middle of the organs is less affected by this phenomenon involved by limiting condition because the structures of suspensions are less numerous. The behavior law of the fasciae is not statistically described in the literature, which leads to greater variation in these areas. Experimental work on these anatomical structures need to be considered in future works to increase the representativeness of the model in these zones. Therefore, it is relevant to study the cervix displacement since they are well defined.

The internal pressure intensity, within the MRI chamber, is strongly conditioning our inverse method inputs and has some potential consequences. The study of sensibility reveals that patient-specific value of pressure levels is needed to predict accurately the material properties. The imposed pressure is specific to the patient, such as mobility and geometry, thus one need to have a measurement means to estimate more accurately dispersion. This justifies our conclusion to develop a device allowing us to obtain this value during the dynamic MRI.

Conclusion

This non-destructive identification approach allows us to identify, for several organs in a single analysis, the material properties of soft tissue under large strain. This application to pelvic system is based on different tools commonly used on biomedical engineering (FE simulation, behavior law, geometrical definition from MRI, displacement field analysis from dynamic MRI). In the presented application, we based our study on these different patient-specific aspects to categorize mechanical stiffness. Results are in the range of experimental data bank. In this methodology, the applied pressure is not yet specific to the patient. It is currently impossible to perform MRI exam of a patient and to know the coupled pressure levels, transferred to the system. Since this should also be patient specific data, rather than literature review evaluation, we should measure them to have a fully patient-specific approach. Works are in progress to develop an intravaginal sensor, which is compatible with dynamic MRI exam and measure the exact pressure imposed on our FE approach.

References

1 Macfarlane AJ, Blondel B, Mohangoo AD, Cuttini M, Nijhuis J, Novak Z, Olafsdottir HS, Zeitlin J, the Euro-Peristat Scientific Committee. Wide differences in mode of delivery within Europe: risk-stratified analyses of aggregated routine data from the Euro-Peristat study. BJOG 2016;123:559–68.

2 Mayeur O, Jeanditgautier E, Witz JF, Lecomte-Grosbras P, Cosson M, Rubod C, Brieu M (2017). Evaluation of strains on levator ani muscle: damage induced during delivery for a prediction of patient risks. Computational Biomechanics for Medicine, pp.135-146.

3 Rortveit G, Brown JS, Thom DH, Van Den Eeden SK, Creasman JM, Subak LL (2007) Symptomatic pelvic organ prolapse: prevalence and risk factors in a population-based, racially diverse cohort. Obstetrics & Gynecology 109(6):1396-1403.

4 Dubuis L, Avril S, Debayle J, Badel P (2011) Identification of the material parameters of soft tissues in the compressed leg, Comput Methods Biomech Biomed Engin., 15(1):3-11

5 Mayeur O, Witz JF, Lecomte-Grosbras P, Brieu M, Cosson M, Miller K (2016) Influence of Geometry and Mechanical Properties on the Accuracy of Patient-Specific Simulation of Women Pelvic Floor. Annals of Biomedical Engineering 44(1):202-212.

6 Namías R, D'Amato JP, Del Fresno M, Vénere M, Pirró N, Bellemare ME. (2016) Multi-object segmentation framework using deformable models for medical imaging analysis, Med Biol Eng Comput., 54(8):1181-92
7 Jiang Z, Witz JF, Lecomte-Grosbras P, Dequidt J, Duriez C, Cosson M, Cotin S, Brieu M (2015) B-spline Based Multi-organ Detection in Magnetic Resonance Imaging: B-spline Based Multi-organ Detection in MRI, Strain, 51, pp.235 - 247
8 Lecomte-Grosbras P, Witz JF, Brieu M, Faye N, Cosson M, Rubid C (2015) Quantification of Pelvic Mobility on Dynamic Magnetic Resonance Images: Using Mechanical Insight to Help Diagnose Pelvic Pathologies, Strain, 51(4):301-310.
9 Kamina, P. Anatomie Clinique, Tome 4. Paris: Maloine;
10 Cobb WS, Burns JM, Kercher KW, Matthews BD, Norton H, Heniford BT (2005). Normal intra-abdominal pressure in healthy adults. J. Surg. Res. 129:231–235, 20
11 Chantereau P, Brieu M, Kammal M, Farthmann J, Gabriel B, Cosson M (2014) Mechanical properties of pelvic soft tissue of young women and impact of aging. Int Urogynecol J. 25(11):1547-1553.
12 Rubod C, Boukerrou M, Brieu M, Jean-Charles C, Dubois P, Cosson M (2008) Biomechanical properties of vaginal tissue: preliminary results. Int Urogynecol J Pelvic Floor Dysfunct 121(9):811–816.
13 Rubod C, Brieu M, Cosson M, Rivaux G, Clay JC, B. Gabriel B (2012) Biomechanical properties of human pelvic organs. Journal of Urology. 79(4):1346–1354.
14 Clay JC, Rubod C, Brieu M, Boukerrou M, Fasel J, Cosson M (2010) Biomechanical properties of prolapsed or non-prolapsed vaginal tissue: impact on genital prolapse surgery. Int. Urogynecol. J. 12:1535–1538.
15 Yeoh, O. H. Some forms of the strain energy function for rubber. Rubber Chem. Tech. 66(5):754–771, 1993.

Simulating Platelet Transport in Type-B Aortic Dissection

Louis P. Parker, [1,2] Lachlan J. Kelsey,[1,2] James Mallal, [1,2] Roland Hustinx, [5] Natzi Sakalihasan, [5] Paul E. Norman, [1,4] Barry J. Doyle.[1,2,3]

[1] Vascular Engineering Laboratory, Harry Perkins Institute of Medical Research, QEII Medical Centre, and Centre for Medical Research, The University of Western Australia, Western Australia, Australia.

[2] School of Mechanical and Chemical Engineering, The University of Western Australia, Australia.

[3] BHF Centre for Cardiovascular Science, The University of Edinburgh, UK.

[4] School of Medicine, The University of Western Australia, Australia.

[5] Cardiovascular and Thoracic Surgery Department, University Hospital Liège, Belgium.

Keywords: computational fluid dynamics, particle residence time, wall shear stress.

Abstract

Aortic dissection is where the medial layer of the arterial wall is separated by a tear leading to intramural bleeding. The blood forms an alternate channel of flow known as the false lumen. Thrombosis of the false lumen is common in cases of dissection as flow conditions are typically more stagnant than in the true lumen. Central to the process of thrombosis is the activation and aggregation of platelets in the blood. Therefore, the aim of this work is to simulate the transport of platelets in a case of Type-B aortic dissection in a clinically-relevant timeframe.

We investigated a 38 year old female with Type-B aortic dissection. After reconstructing the contrast-enhanced computed tomography (CT) scans into three dimensions, we created a computational mesh of polyhedral and prism elements. We used realistic boundary conditions at the inlet and at the outlets via 3-element Windkessel models. A one-way Lagrangian method was used to model the trajectories of platelets and particles were injected for 11 seconds over 16 cardiac cycles. The total number of injected particles was 1.5M. We ran our simulations on 512 cores of the MAGNUS supercomputer at the Pawsey Supercomputing Centre.

We observed elevated residence times of these particles in regions of both stagnant (low TAWSS) and recirculating flow (high OSI), emphasising the need to consider both TAWSS and OSI in thrombus susceptibility predictions for dissection. Tear geometry was seen to have a dominating effect on TL haemodynamics, with platelets colliding and adhering to the wall primarily around the proximal entry tears and supra-aortic branching vessels.

The complex flow patterns support the need for computational modeling to reveal flow conditions and prognosis for Type-B aortic dissection patients. Furthermore, high-performance computing enables computationally expensive patient-specific simulations to be carried out within a clinical timescale.

1 Introduction

Aortic dissection is where the medial layer of the arterial wall is separated by a tear leading to intramural bleeding [1]. The blood forms an alternate channel of flow known as the false lumen (FL). The aorta may then have a series of tears between the true lumen (TL) and FL. The disease is the most common acute aortic condition to require urgent surgical intervention [2-6]. Treatment of the disease can be divisive amongst clinicians as little is understood about the mechanics of the disease and early warning signs of complication. Complications of the disease may be either (a) malperfusion syndrome where the dissecting FL occludes a branching artery leading to end-organ ischemia (lack of blood supply) [7] or (b) hemorrhage resulting from rupture of the false lumen [8]. Type-B refers to the Stanford classification of aortic dissection, where the FL begins distal to the left subclavian artery, the last of the three main arteries to branch off the aortic arch.

It is common in cases of dissection to observe the development of intraluminal thrombus in the FL where flow conditions are typically more stagnant than in the TL. In predicting complication it appears that the patency of the false lumen shows some promise as a prognostic tool. Imaging studies have followed the outcomes of patients with a fully patent lumen and have concluded that this is associated with poor outcomes [3, 9-11]. Research shows that partial thrombosis of the FL is even more detrimental with a 2.7-fold increase in death when compared with cases where the FL is fully patent [9, 12]. A fully thrombosed FL represents a stable form of the disease where intervention is no longer required. The alternate channel created for the blood to flow through has been naturally occluded eliminating the risk of further progression. This link between patient outcomes and the development of thrombosis in the FL has lead computational research into aortic dissection to focus on thrombus development modelling [13]. An accurate computational tool that could predict thrombosis of the FL would allow the treating clinician to determine the prognosis.

Central to the process of thrombosis is the activation and aggregation of platelets in the blood. Recirculation zones in the FL that exhibit long residence times for platelets and low wall shear stress (WSS) conditions create the necessary environment for platelet aggregation and eventual deposition [13-15]. The transport of platelets through the system can be effectively simulated using Lagrangian multiphase models available in STAR-CCM+ (Siemens, Berlin). By injecting and simulating the platelet trajectories in aortic dissection we are able to examine the susceptibility of sections of the geometry to thrombogenesis and help form early hypotheses as to the dominant flow patterns that encourage thrombosis.

Therefore, the aim of this work is to simulate the transport of platelets in a case of Type-B aortic dissection. To the authors knowledge a simulation of platelet transport has not been performed in aortic dissection until now. It is common to examine relative residence time (RRT) in arterial haemodynamic studies which is calculated using WSS and oscillatory shear index (OSI) at the surface. The simulation of physical particles in this study considers particle age after collisions with the wall and allows for analysis of the platelets which adhere to the wall.

2 Method

2.1 Patient details and imaging

The patient was a 38 year old female who attended the Cardiovascular and Thoracic Surgery Department at the University Hospital Liege, Belgium. This represents a unique case as the patient is particularly young with no indication of any connective tissue disorder. Contrast-enhanced computed tomography (CT) was performed (slice thickness 1 mm), as well as imaging with 18F-FDG Positron Emission Tomography (PET), an effective method to identify inflammation in the aortic wall [16], which revealed significant myocarditis. The patient also had severely impaired ejection at only 25% with a 130/70 mmHg resting blood pressure.

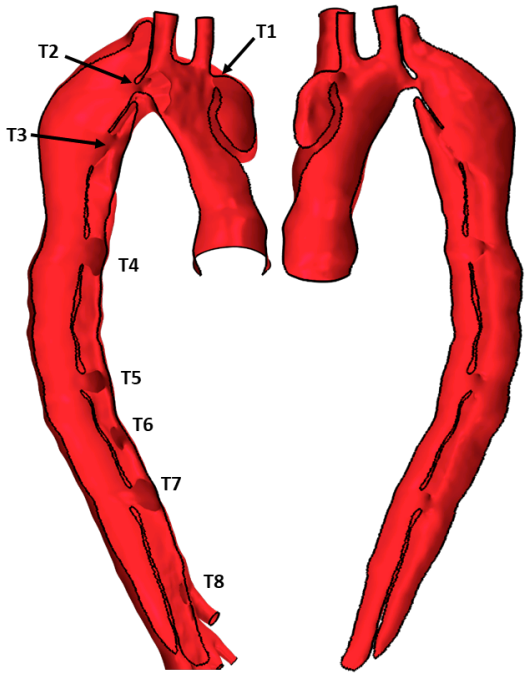

Fig. 1 A cross-section of the geometry showing the first 8 entry tears (T1-T8). Distal to this (not shown) are two small re-entry tears.

2.2 Patient-specific Reconstruction

The dissecting aorta was segmented from the CT scan based on pixel intensity and then reconstructed in 3D using Mimics (v19.0, Materialise, Belgium). Further manual manipulation was required to remove the minor arteries and scan artifacts using surface repair tools allowing for the deletion and creation of surface cells that more accurately represent the lumen wall [17]. The locations of the entry and exit tears between the TL and FL were identified on the original CT image and this was used as a reference point to ensure that all were incorporated into the final geometry. The geometry was smoothed using a Laplacian method to remove any sharp edges in the surface and represent the lumen wall as accurately as possible.

2.3 CFD Mesh

A greater number of cells are required in regions of steep velocity gradient to accurately compute the flow. Aortic dissection cases are likely to be the most complex geometries analysed in arterial CFD as the internal structures create very steep velocity gradients throughout the model. The meshing protocol used for this simulation was designed for an efficient allocation of cells within the fluid domain and performed using the angle-based selection of surface cells and reduced cell size remeshing, using the surface-preparation and meshing tools available in STAR-CCM+. The nature of this process allows it to be automated and executed remotely.

Polyhedral cells were used for the majority of the fluid domain for their superior accuracy and efficiency [18]. The prism-layer mesher was used to create a high number of anisotropic cells in close proximity to the non-slip luminal wall to accurately capture boundary-layer. The prism layer thickness, *t,* was sufficiently large as it followed the boundary-layer width expected for Hagen-Poiseiulle flow. The relationship is dependent on the local vessel radius, R as has been adopted in similar CFD investigations [19, 20].

$$t = \left(1 - \frac{1}{\sqrt{2}}\right) R \qquad \text{(Equation 1)}$$

A stretching parameter, *S* is also specified to allocate a decreasing number of cells as we move away from the arterial wall, towards the centre of the artery where the velocity gradient eases. The same process has been adopted in similar CFD investigations where *S* is dependent on the total number of prism layers, *n* [19, 20].

$$\mathrm{S} = 2^{\left(\frac{1}{n-1}\right)} \qquad \text{(Equation 2)}$$

To further ensure that the flow dividers and tight bends in the geometry received preferential allocation of cells in the meshing process, careful attention was given to the surface mesh prior to generating a volume mesh. The surface mesh forms the basis of the volume mesh and so by reducing cell sizes around particular features, refinement of the volume mesh would follow. The process started with

re-meshing the entire surface to faces with an edge length of 8×10^{-4} mm. A selection was then made of the cells at the surface attached by an angle no greater than 12 degrees to an arbitrary flat section. This selection was then inverted to leave only cells in the surface that were beyond a 12 degree incline from the rest of the geometry, these being the areas at the leading edge of bifurcations and at tight bends such as branching points. This subset of cells was then expanded to include all bordering cells and the edge length of these cells was reduced to 2×10^{-4} mm. The interface between the two regions of different surface size was then blended, and the refined region conservatively smoothed while maintaining all geometric features.

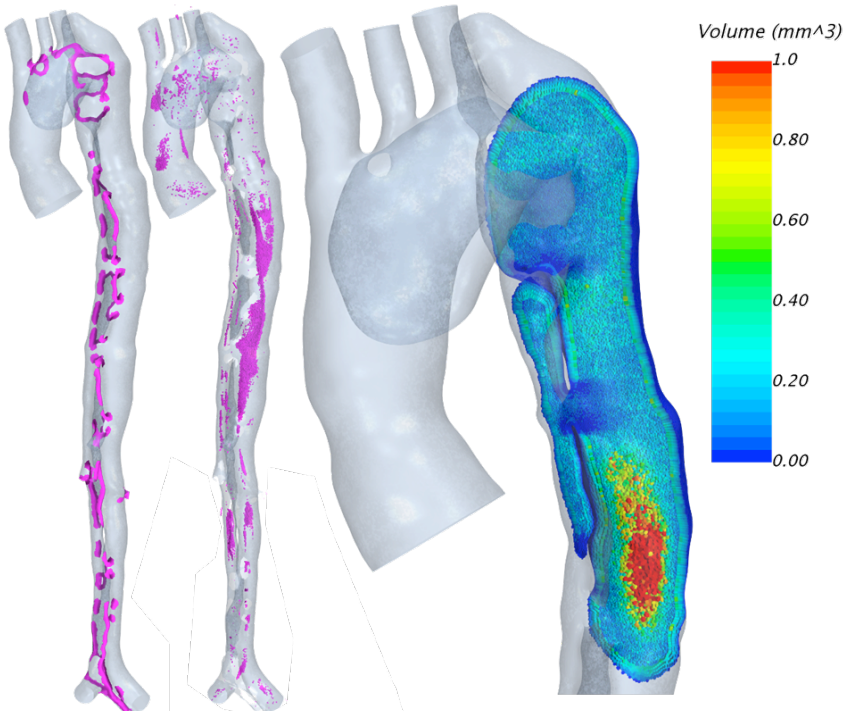

Fig. 2 The mesh refinement region with the remeshed surface cells shown in pink (left), volume mesh refinement region with the refined volume cells shown in pink (middle) and a cross-section of the volume mesh after refinement (right).

A steady state simulation was run on this mesh at typical systole conditions, with an inlet mass flow rate of 0.3 kg/s and an equal flow-split boundary applied to the nine outlets. This was performed to identify regions of steep (spatial) velocity gradient in the core polyhedral mesh that would benefit from increased refinement. The mesh was iteratively refined by reducing cell sizes until the change in velocity across each polyhedral-cell in the mesh was similar. The final mesh contained 6M cells.

2.4 Physical Assumptions and Boundary Conditions

A laminar flow model was used as has been the case for similar investigations [19]. Blood was modelled as an incompressible fluid with a density of 1050 kg/m^3 and a Carreau-Yasuda non-Newtonian approximation for viscosity. A non-slip, rigid wall boundary was applied [21-25]. We explicitly coupled the 3D CFD simulation with a 3-element Windkessel model at each outlet boundary to estimate the resistance and compliance of the downstream vascular beds. This improves the estimation of pressure throughout the domain and allows the pressure waveform at the aortic inlet to comply with the patient's systolic and diastolic pressures. The Windkessel parameters were calibrated according to previous methodology [18, 23, 26], whereby the resistance (target flow) and compliance are proportional to outlet vessel cross-sectional area. The physical time-step was fixed to 1ms, where a maximum of 15 inner iterations per-time-step was sufficient to maintain root-mean-square absolute momentum and continuity residuals below 10^{-10}.

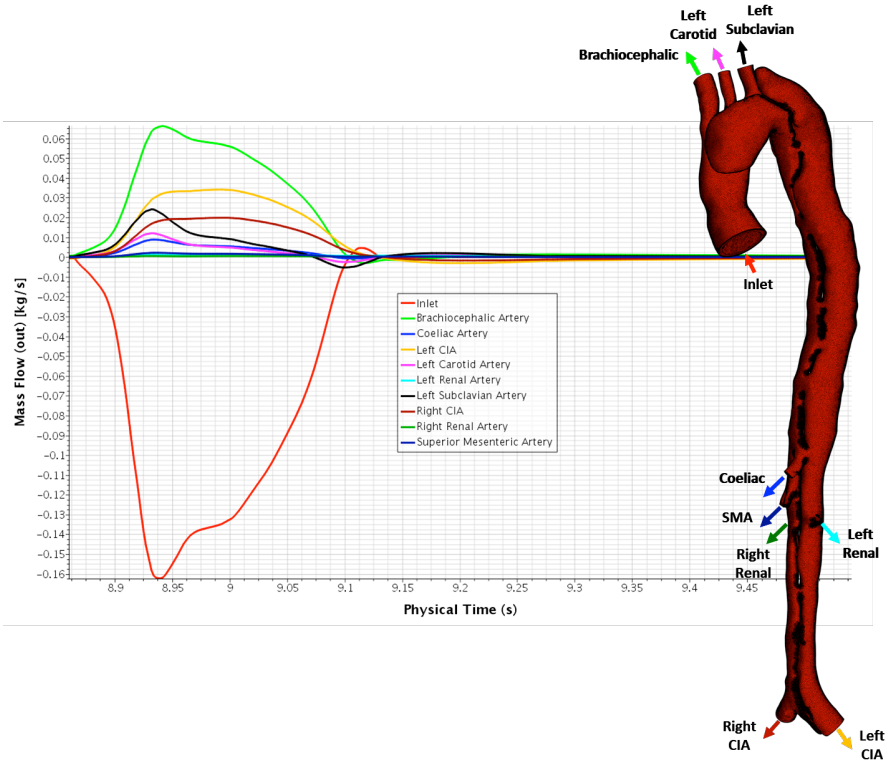

Fig. 3 The particle age shown at each particle (top), the DRT mapped to the surface (bottom).

2.4 One-way Lagrangian Particle Modelling

A one-way Lagrangian method was used to model the trajectories of platelets and was based on the same process we have used in a previous study [19]. This method has been validated against the experimental data from Pui et al. [27]. We created an injection plane of 1,323 points normally aligned with the direction of flow, ~3cm into the geometry past the inlet. The location of this plane allows injection of the platelets well before the regions of interest in the FL and TL. The particles injected were modelled as spherical, a common assumption in the large arteries [28-30], with a diameter of 2µm and a density of 1040 kg/m^3. These material properties for platelets have been used for similar investigations in abdominal aortic aneurysms [31]. The particles were injected through the plane at randomly distributed points with the inclusion probability set proportional to the mass flow rate. This methodology has previously been applied to studies of platelet movement in common iliac aneurysms, where the local sub-stepping of particles within each physical time-step is bounded by minimum and maximum Courant numbers, set to 0.05 and 0.35, respectively [19]. The forces on each particle consisted of the pressure gradient force (Equation 3) and the drag forces (Equations 4 and 5). C_d (Equation 4) being the empirically derived Schiller-Naumann drag force coefficient, as used in previous studies [19, 31].

$$F_d = \frac{1}{2} C_d \rho A_p |\boldsymbol{v_s}| \boldsymbol{v_s} \tag{3}$$

$$C_d = \frac{Re_p}{24}(1 + 0.15 Re_p^{0.687}) \tag{4}$$

$$F_p = -V_p(\nabla P_s) \tag{5}$$

where,

Re_p is the particle Reynolds Number,
ρ is fluid density,
$\boldsymbol{v_s}$ is the particle slip velocity,
A_p is the projected particle area,
V_p is particle volume, and
∇P_s is the gradient of static pressure.

The particles were injected for 11 seconds, just over 16 cardiac cycles at 88 BPM. It was important to simulate as many cycles as feasible to allow the particles to travel distally throughout the domain and have an even distribution. The total number of injected particles was 1.5M. Even with such a low ejection fraction the number of particles simulated is orders of magnitude less than would be expected

in vivo, they do however provide a representative sample of particles in the system and allow us to observe regions where particles become trapped for a long period of time and are at increased risk of deposition [31]. The particle age was recorded for each particle in this study to determine where platelets preferentially reside in the FL and TL. The particle age of the platelets in the entire domain was converted to a domain residence time (DRT) for each computation cell in the mesh. This is calculated as the average particle age at each cell, where cells without particles have this value determined using an inverse distance weight of values at neighbouring cells. The simulation was run until there was an adequate distribution of cells in all parts of the domain to ensure accurate DRT values. Additionally the domain has been divided into eight regions and the average DRT provided (from near-wall cells). Note that, the most distal particles have a greater age by nature of being further from the injection plane, therefore the comparison of the average DRT in TL and FL segments are equidistant from the aortic root will allow comparisons to be made regarding local particle residence and entrapment.

2.5 Simulation details

We ran our simulations on the MAGNUS supercomputer at the Pawsey Supercomputing Centre (Perth, Australia). This system consists of 2,976, 12-core Intel Xeon E5-2690V3 Haswell processors giving a total of 35,712 cores and over a PetaFLOP of computing power. Our simulation was run on 512 cores for 15 hours, providing 21 seconds of physical time or just over 30 cardiac cycles for this particular case. User-defined field functions were created for Time-averaged Wall Shear Stress (TAWSS) and Oscillatory Shear Index (OSI) which were calculated based on the final three cardiac cycles as well as Endothelial Cell Activation Potential (ECAP), the ratio: OSI/TAWSS, which has been used as an indicator of thrombogenic susceptibility in the aorta [32].

3 Results and Discussion

3.1 Particle Residence and Transport

The geometry features two distinct saccular regions in the aortic arch (indicated by A and B on Figure 3). These regions were observed to trap particles around their exterior. Particles that made it into these regions in the first cycle were still present after 11 seconds or 16 cardiac cycles. Interestingly there was a large number of these particle from the first cardiac cycle within the TL of the descending thoracic aorta (C on Figure 3). In what is a relatively straight section of the aorta we would expect to see laminar flow conditions that flush these particles out within the proceeding cardiac cycles. This points to recirculation zones caused by the complex tear geometries. This stagnation of the TL in this region is unique in that in cases of dissection it is usually assumed that stagnation will occur in the FL as

by its nature the blood must enter through a tear and it is often constrained by a small re-entry tear. In this case it appears that the geometry of the first major entry tear and its location just beyond the left subclavian artery means that the FL receives the majority of the massflow. In this geometry it would be likely that if a thrombus development model was applied we would see the development of thrombus in the TL, at least in the descending thoracic segment, this information would present a unique issue for clinicians. A fully thrombosed FL is believed to represent a stable case of the disease as we no longer have blood entering the FL and progressing the disease. If, as in this case we have branching arteries attached to the FL, full thrombosis of the FL is no longer desirable due to the likelihood of renal ischemia.

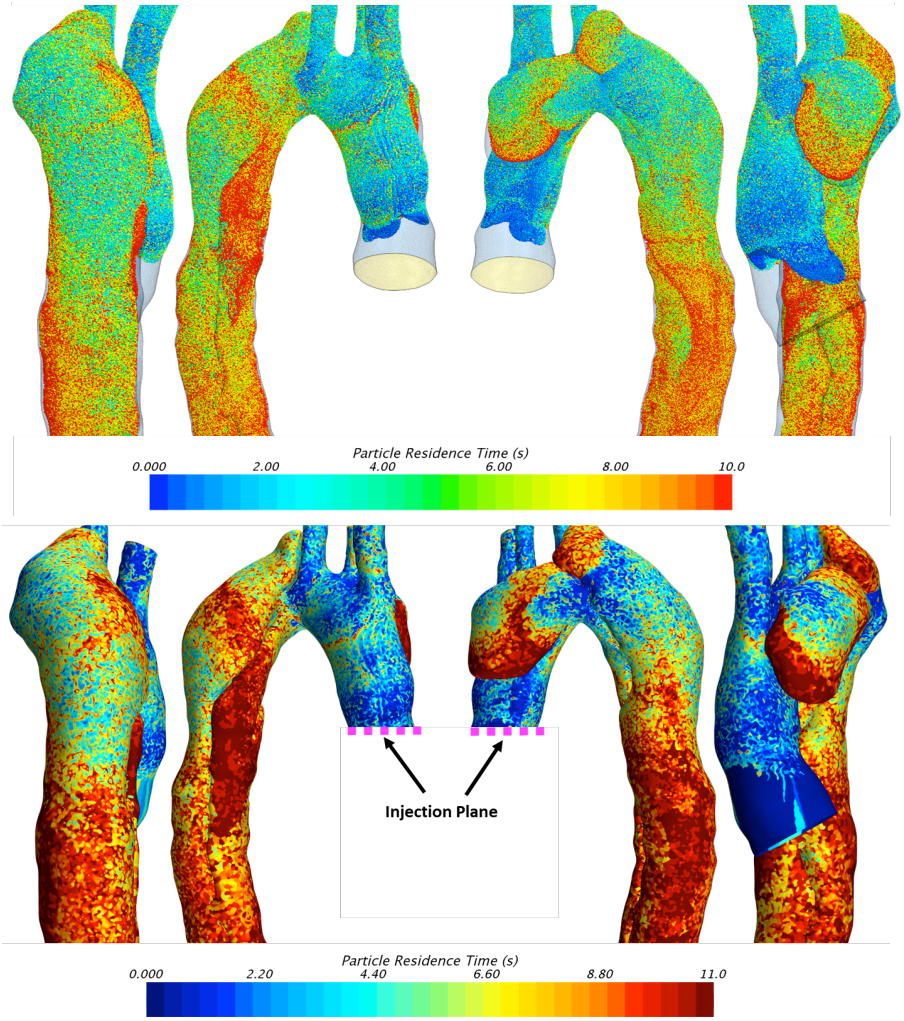

Fig. 4 The particle age shown at each particle (top), the DRT mapped to the surface (bottom).

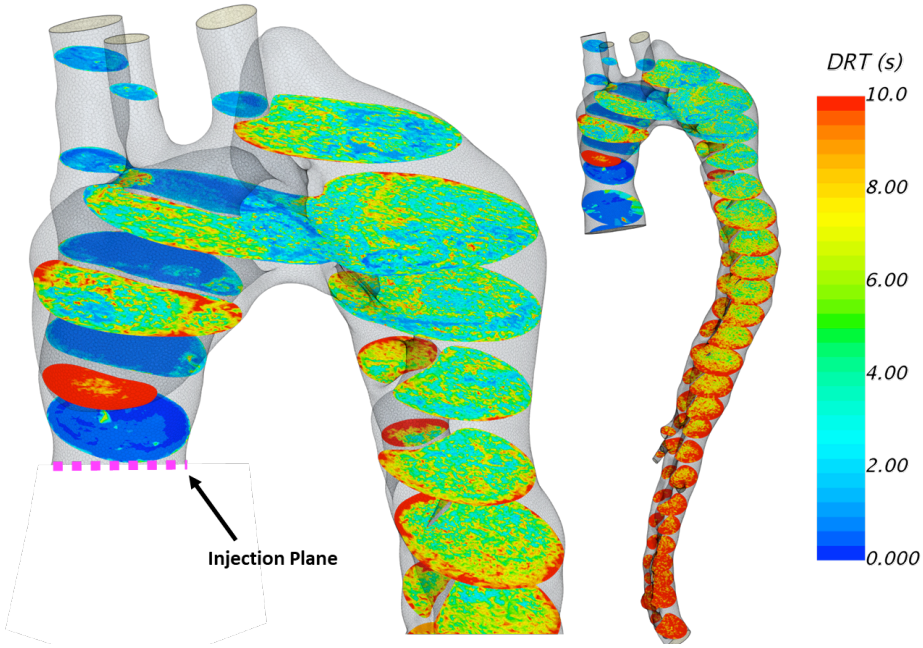

Fig. 5 The DRT shown for each cell on a series of internal plane sections.

3.2 Haemodynamic Surface Conditions

TAWSS in the aortic arch showed a strong correlation with the DRT conditions. We observed stagnant, low TAWSS conditions here leading to higher overall DRT. In the descending thoracic aorta we do not see the same relationship between shear stress and residence time. The TAWSS in this region is 20% higher in the TL when compared with the equivalent FL segment however, the FL shows far lower DRT values. The major difference between the TL and FL in the descending thoracic aorta was in OSI where we observed a 30% increase suggesting that the high DRT values are resulting from recirculation zones in the flow. High TAWSS conditions may be retained in recirculating zones as the blood is still exerting shear at the wall, however the direction of this shear if fluctuating contributing to elevated OSI.

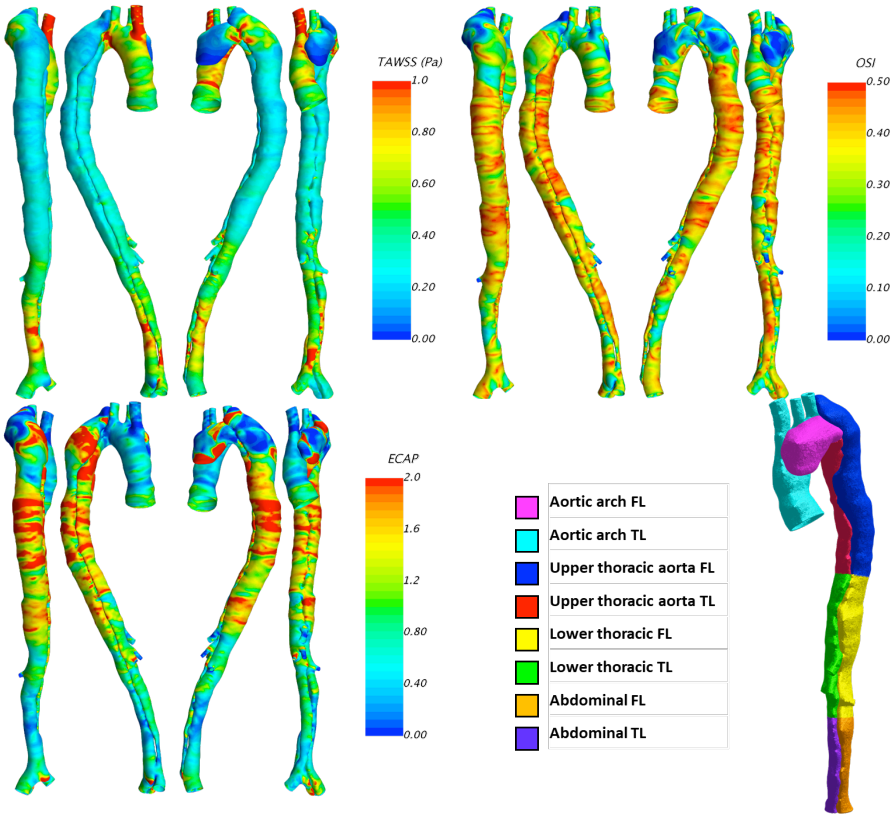

Fig. 6 Contour plots showing surface values for TAWSS (top left), OSI (top right) and ECAP (bottom left). The bottom right shows the surface segments used for the analysis of surface average DRT, TAWSS, OSI and ECAP.

The source of this high OSI is likely to be the series of tears between the TL and FL in this region (see Figure 5) and this confirms the theory that tear geometry is critical to the consideration of thrombus development in dissection and its subsequent management. This observation contributes to the argument that patient-specific CFD has great potential in dissection cases where inspection of CT imaging alone is insufficient to determine whether a case is likely to be stable over a period of time. As the entry tear separates the existing aortic wall, the FL wall is thinner than in the TL and so likely compromised in strength. The observation that majority of the flow is entering the FL as it exits the aortic arch could be critical to management in this particular case as the thinner wall will be at increased risk of rupture under a greater load. The sharp change in direction in flow exiting the arch is likely to cause impingement of the flow on the FL wall and increased FL pressure further increasing the prospect of rupture.

Table 1 Surface average values for the aorta segments shown in Figure 4.

Region	DRT (s)	TAWSS (Pa)	OSI	ECAP
Aortic arch FL	7.53	0.265	0.125	2.372
Aortic arch TL	2.87	0.756	0.265	0.447
Upper thoracic aorta FL	7.86	0.286	0.295	1.297
Upper thoracic aorta TL	8.63	0.343	0.383	1.428
Lower thoracic FL	10.04	0.355	0.372	1.149
Lower thoracic TL	9.91	0.375	0.352	1.029
Abdominal FL	9.95	0.666	0.285	0.486
Abdominal TL	10.13	0.599	0.386	0.728

3.3 Platelet Wall Collisions

When platelets made contact with the vessel wall, they were fixed in space, and while this is not a realistic model for wall adhesion we believe that these areas of collision are valuable to visualize and understand. These conditions of flow impingement make platelet, and other larger blood cell, contact with the lumen most likely. We observed adhesion in the upstream facing flow dividers. The complex flow patterns occurring around the brachiocephalic, left common carotid and left subclavian artery branches show a large number of collisions also.

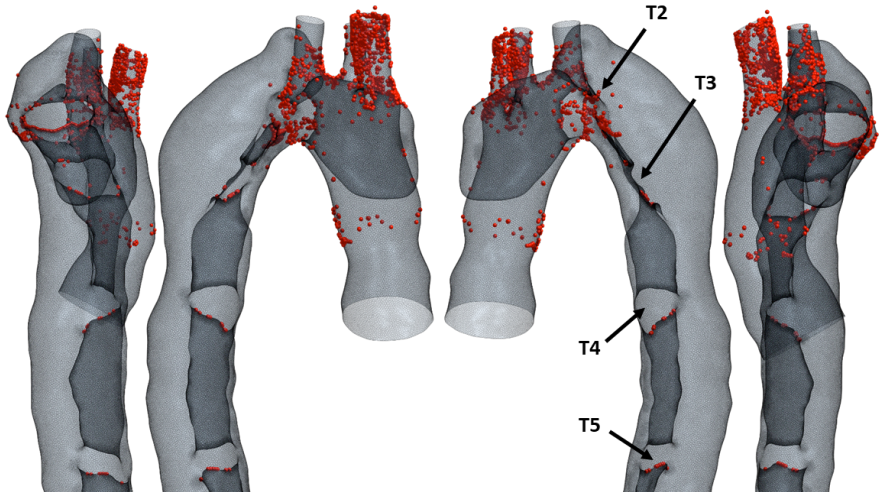

Figure 5. Particles that have adhered to the wall indicated in red as well as the first four entry/re-entry tears (T1-T4).

3.4 Applicability of Supercomputing to PSM

A major barrier to the inclusion of computationally intensive modelling in the clinical setting is the associated turnaround time from scan to results. The advent of high-performance computing clusters (HPC), such as MAGNUS, represent a potential solution. A simulation such as that considered in this study would not be viable on a standard workstation within a reasonable clinical timeframe. Automated mesh refinement based on the results of a steady-state pre-simulation is also clinically applicable, removing the need for user input to increase the accuracy of the mesh. The application of a highly scalable model for aortic dissection could make the simulation of large, statistically significant cohorts of patients viable with the potential to effectively define the relationship between haemodynamic conditions, thrombosis and prognosis.

To further quantify the applicability of HPC in simulation processing we have examined the scalability of the simulation to better understand the relationship between the cores allocated to the simulation and the resulting turnaround time. The time spent computing successive iterations decreased linearly as the number of CPUs used increased (analyzed at: 256, 512, 1024, 2096 and 4096 CPU cores). Without the progressive injection of platelets, the simulation of a cardiac cycle on a 6M cell mesh takes one minute using 4096 CPU cores.

4 Conclusion

This study presents a single case of Type-B aortic dissection analysed with the injection of 1.5M platelets. Though only a single case was simulated, it represents a relatively complex geometry and these methods are very transferrable to any other dissection case. We observed elevated residence times of these particles in regions of both stagnant (low TAWSS) and recirculating flow (high OSI) in separate regions, emphasising the need to consider both TAWSS and OSI in thrombus susceptibility predictions for dissection as the relationship may not be as solely dependent on low TAWSS conditions as previously thought. Tear geometry was seen to have a dominating effect on TL haemodynamics. The complex flow pattern emerging from these features support the need for CFD as a supplement to CT imaging when assessing prevailing flow conditions and prognosis for Type-B aortic dissection patients. The application of HPC in this study has demonstrated how computationally expensive patient-specific CFD simulations can now be carried out on a clinical timescale.

Acknowledgements

We would like to acknowledge funding from the National Health and Medical Research Council (grants APP106986 and APP1083572) and the William and Marlene Schrader Trust. This work was supported by resources provided by the Pawsey Supercomputing Centre with funding from the Australian Government and the Government of Western Australia. The patient was imaged for the Liège Study on Dissected Aorta (LIDIA) partially funded by 'Fonds pour la chirurgie cardiaque, Belgium' and unrestricted research grant from Medtronic.

References

1. R. Erbel, et al., 2014 ESC Guidelines on the diagnosis and treatment of aortic diseases: Document covering acute and chronic aortic diseases of the thoracic and abdominal aorta of the adult. The Task Force for the Diagnosis and Treatment of Aortic Diseases of the European Society of Cardiology (ESC). Eur Heart J **35**(41), p. 2873-926, (2014). doi:10.1093/eurheartj/ehu281
2. B.K. Khandheria, Aortic dissection. The last frontier. Circulation **87**(5), p. 1765-8, (1993).
3. R. Pretre and L.K. Von Segesser, Aortic dissection. Lancet **349**(9063), p. 1461-4, (1997). doi:10.1016/S0140-6736(96)09372-5
4. C.S. Roberts and W.C. Roberts, Aortic dissection with the entrance tear in the descending thoracic aorta. Analysis of 40 necropsy patients. Ann Surg **213**(4), p. 356-68, (1991).
5. P.G. Hagan, et al., The International Registry of Acute Aortic Dissection (IRAD): new insights into an old disease. JAMA **283**(7), p. 897-903, (2000). doi:10.1001/jama.283.7.897
6. L.K. Bickerstaff, et al., Thoracic aortic aneurysms: a population-based study. Surgery **92**(6), p. 1103-8, (1982). doi:0039-6060(82)90174-X
7. M. Midulla, et al., Aortic dissection and malperfusion syndrome: a when, what and how-to guide. Radiol Med **118**(1), p. 74-88, (2013). doi:10.1007/s11547-012-0815-9
8. T.T. Tsai, et al., Long-term survival in patients presenting with type A acute aortic dissection: insights from the International Registry of Acute Aortic Dissection (IRAD). Circulation **114**(1 Suppl), p. I350-6, (2006). doi: 10.1161/circulationaha.105.000497
9. T.T. Tsai, et al., Tear size and location impacts false lumen pressure in an ex vivo model of chronic type B aortic dissection. J Vasc Surg **47**(4), p. 844-51, (2008). doi:10.1016/j.jvs.2007.11.059 [doi]
10. R. Erbel, et al., Effect of medical and surgical therapy on aortic dissection evaluated by transesophageal echocardiography. Implications for prognosis and therapy. The European Cooperative Study Group on Echocardiography. Circulation **87**(5), p. 1604-15, (1993).

11. Y. Bernard, et al., False lumen patency as a predictor of late outcome in aortic dissection. Am J Cardiol **87**(12), p. 1378-82, (2001). doi: S0002914901015569
12. T.T. Tsai, et al., Partial thrombosis of the false lumen in patients with acute type B aortic dissection. N Engl J Med **357**(4), p. 349-59, (2007). doi:10.1056/NEJMoa063232 [doi]
13. C. Menichini and X.Y. Xu, Mathematical modeling of thrombus formation in idealized models of aortic dissection: initial findings and potential applications. J Math Biol **73**(5), p. 1205-1226, (2016). doi:10.1007/s00285-016-0986-4
14. A.M. Malek, S.L. Alper, and S. Izumo, Hemodynamic shear stress and its role in atherosclerosis. JAMA **282**(21), p. 2035-42, (1999).
15. M.S. Goel and S.L. Diamond, Adhesion of normal erythrocytes at depressed venous shear rates to activated neutrophils, activated platelets, and fibrin polymerized from plasma. Blood **100**(10), p. 3797-803, (2002). doi: 10.1182/blood-2002-03-0712
16. A. Courtois, et al., 18F-FDG uptake assessed by PET/CT in abdominal aortic aneurysms is associated with cellular and molecular alterations prefacing wall deterioration and rupture. J Nucl Med **54**(10), p. 1740-7, (2013). doi: 10.2967/jnumed.112.115873
17. B.J. Doyle, et al., 3D reconstruction and manufacture of real abdominal aortic aneurysms: from CT scan to silicone model. J Biomech Eng **130**(3), p. 034501, (2008). doi:10.1115/1.2907765
18. M. Spiegel, et al., Tetrahedral vs. polyhedral mesh size evaluation on flow velocity and wall shear stress for cerebral hemodynamic simulation. Comput Method Biomech Biomed Eng **14**(1), p. 9-22, (2011). doi: 10.1080/10255842.2010.518565
19. L.J. Kelsey, et al., A comparison of hemodynamic metrics and intraluminal thrombus burden in a common iliac artery aneurysm. Int J Numer Method Biomed Eng **33**(5), (2017). doi:10.1002/cnm.2821
20. L.J. Kelsey, et al., The influence of downstream branching arteries on upstream haemodynamics. J Biomech **49**(13), p. 3090-3096, (2016). doi:10.1016/j.jbiomech.2016.07.023
21. Doyle BJ, et al., From Detection to Rupture: A Serial Computational Fluid Dynamics Case Study of a Rapidly Expanding, Patient-Specific, Ruptured Abdominal Aortic Aneurysm. In: Computational Biomechanics for Medicine, p. 53-68, (2014). doi:10.1007/978-1-4939-0745-8_5
22. A.J. Boyd, et al., Low wall shear stress predominates at sites of abdominal aortic aneurysm rupture. J Vasc Surg **63**(6), p. 1613-9, (2016). doi:10.1016/j.jvs.2015.01.040
23. A.S. Les, et al., Quantification of hemodynamics in abdominal aortic aneurysms during rest and exercise using magnetic resonance imaging and computational fluid dynamics. Ann Biomed Eng **38**(4), p. 1288-313, (2010). doi:10.1007/s10439-010-9949-x

24. C. Poelma, P.N. Watton, and Y. Ventikos, Transitional flow in aneurysms and the computation of haemodynamic parameters. J R Soc Interface **12**(105), (2015). doi:10.1098/rsif.2014.1394
25. B.J. Wolters, et al., A patient-specific computational model of fluid-structure interaction in abdominal aortic aneurysms. Med Eng Phys **27**(10), p. 871-83, (2005). doi:10.1016/j.medengphy.2005.06.008
26. W.K. Laskey, et al., Estimation of total systemic arterial compliance in humans. J Appl Physiol (Bethesda, Md. : 1985) **69**(1), p. 112-9, (1990).
27. D.Y.H.R.-N. Pui, Francisco ; Liu, Benjamin Y. H., Experimental Study of Particle Deposition in Bends of Circular Cross Section. Aero Sci Tech **7**(3), p. 301-315, (1987).
28. D. Hardman, et al., On the prediction of monocyte deposition in abdominal aortic aneurysms using computational fluid dynamics. Proc IMechE Part H J Eng Med 227(10), p. 1114-1124, (2013). doi:10.1177/0954411913494319
29. T. AlMomani, et al., Micro-scale Dynamic Simulation of Erythrocyte–Platelet Interaction in Blood Flow. Ann Biomed Eng **36**(6), p. 905-920, (2008). doi:10.1007/s10439-008-9478-z
30. P.W. Longest, C. Kleinstreuer, and J.R. Buchanan, Efficient computation of micro-particle dynamics including wall effects. Computers & Fluids **33**(4), p. 577-601, (2004). doi:10.1016/j.compfluid.2003.06.002
31. C. Basciano, et al., A relation between near-wall particle-hemodynamics and onset of thrombus formation in abdominal aortic aneurysms. Ann Biomed Eng **39**(7), p. 2010-26, (2011). doi:10.1007/s10439-011-0285-6
32. P. Di Achille, et al., A haemodynamic predictor of intraluminal thrombus formation in abdominal aortic aneurysms. Proc R Soc A Math Phys Eng Sci **470**(2172), (2014). doi:10.1098/rspa.2014.0163